Master of Science Thesis

Characterization of the flow-field in circular subsonic impinging jets

Investigation of surface pressure fluctuations and far-field noise emissions through pressure sensor measurements

Swathi Krishna

05-07-2012

Faculty of Aerospace Engineering · Delft University of Technology

Characterization of the flow-field in circular subsonic impinging jets

Investigation of surface pressure fluctuations and far-field noise emissions through pressure sensor measurements

Master of Science Thesis

For obtaining the degree of Master of Science in Aerospace Engineering at Delft University of Technology

Swathi Krishna

05-07-2012

Faculty of Aerospace Engineering · Delft University of Technology

Delft University Of Technology
Department Of
Aerodynamics

The undersigned hereby certify that they have read and recommend to the Faculty of Aerospace Engineering for acceptance a thesis entitled **"Characterization of the flow-field in circular subsonic impinging jets"** by **Swathi Krishna** in partial fulfillment of the requirements for the degree of **Master of Science**.

Dated: 05-07-2012

Examination committee:

Prof. Dr. Fulvio Scarano

Mr. Daniele Violato, M.Sc

Dr. ir. Ferdinand Schrijer

Dr. Mark Tummers

Abstract

Impinging jets are relevant flow configurations in many technological developments. For example, on some short take-off and landing aircraft the high speed exhaust from the jet engine is deflected by direct impingement on the flaps to create extra lift during take-off. Fatigue due to excessive dynamic loading on the flaps and high levels of noise radiation are among the problems encountered in such designs. Additionally, such flow-structure interaction is a good model for cooling of turbine blades, annealing of plastic and metal sheets, deicing of aircraft systems etc.. Jets are easy to simulate and contain all the constituents necessary for the study of shear flows. The shear-layer instability at the nozzle edge develops into axisymmetric toroidal vortices which magnifies in size and strength downstream of the nozzle. The interaction of these vortices with the solid structures induces pressure fluctuations that manifests in the form of noise in the far-field region. Hence, it is also a benchmark case for studying vortex-structure interaction noise.

Various researchers have employed flow visualization, pressure sensor measurements and optical techniques to study the behaviour of an impinging jet until now. This thesis focusses on characterizing wall pressure fluctuations and far-field noise emissions in impinging jets for different flow regimes by means of sensor measurements. The set-up consists of a round jet impinging orthogonally on a solid aluminium plate embedded with a pressure sensor in the center. Initially, jet impingement in laminar, transitional, turbulent and highly turbulent regimes have been studied for a specific nozzle-to-plate distance of 4 diameters. The pressure fluctuations across the horizontal and vertical axes of the jet is scanned to produce a profile that helps describe the nature of flows at $Re = 5000$, 10000, 20000, 50000. The progress of pressure fluctuations as the nozzle-to-plate distance is differed has also been studied for three high Reynolds number flows. Fourier decomposition of the pressure fluctuations along the radial sweep is compared to gain an understanding of the inherent frequencies that mark specific events in an impinging jet. Following which, a study of secondary vortices, observed in the radial wall jet region of highly turbulent flows has been carried out for varying distances of 1 to 8 diameters from the nozzle exit. These near-field measurements are followed by acoustic microphone measurements for highly turbulent flows.

The pressure fluctuation profiles confirms the axisymmetry of the jet and provide quan-

titative data on vortex impingement by exhibiting a peak in the region of impact. The results show that the maximum standard deviation of the pressure fluctuations decrease as the Reynolds numbers increases. This suggests that as the velocity of the flow increases, the coherence of the toroidal structures impinging on the surface decreases and the vortices become weaker. Priorly obtained data from time-resolved measurements through Tomographic PIV is used as an aid to explain the interpretations drawn from sensor measurements. The onset of the secondary peak suggesting possible unsteady separation and formation of secondary vortices occurs from $Re = 25000$ at nozzle-to-plate distances of 3 and 4 diameters. The power spectrum exhibits the energy of impinging vortices and their convection in the flow. The non-dimensional frequencies given by Strouhal numbers are nearly the same for smaller Reynolds numbers with $St \approx 0.38$ for vortex pairing and around $St \approx 0.7$ for vortex shedding at a fixed nozzle-to-plate distance of 4 diameters. The distinct peaks of the vortex shedding and pairing as seen at lower velocities transform into a broader peak indicating aperiodic passage of vortices as the Reynolds number increases. The acoustic measurements provide an insight into the sound pressure levels perceived due to jet impingement at two mic-angles and far-field distances for a highly turbulent flow regime while also giving an estimate of the range of underlying frequencies in the system.

Acknowledgements

The last two and half years has been a giant roller-coaster ride for me. There are many people who have helped me come this far and I cannot go further before expressing my deepest gratitude to them.

Firstly, to Prof. Dr. Fulvio Scarano for giving me a great opportunity to be his student and work on a challenging and interesting topic. His encouragement and guidance proves to be a real confidence booster.

My profound gratitude to Daniele Violato for the time and patience he invested to teach and steer me in the right direction. His eye for perfection and organized approach towards experimentation is something I have tried to inculcate in myself over the last year and will carry forward.

Many thanks to Stefan Bernardy, Eric de Keizer, Peter Duyndam, Nico van Beek, Frits Donker Duyvis for all the help in building the experimental set-up and fixing smaller issues that cropped up every now and then.

My earnest appreciation for Dr. Daniele Ragni, Dr. Andrea Ianiro, Sina Ghaemi, Stefan Probsting for the guidance and help during tricky phases of experimentation.

A bow to Dr. S.Sundaram and Dr. Jelmer Wind for being such wonderful tutors and inspiring me when I needed it most.

I am eternally grateful to B.S.Srinivas Murthy, Latha Shastry, H.V.Krishna Shastry, Sanath Kumar and Shreenivas who made it possible for me to come here in the first place.

A big hug to Anouk van Rooij and Momchil Dimchev, for being a bright silver lining underneath the clouds of Holland.

To Anil, who has been my life support system in a foreign country and to Ajay, Sundeep and Praveen who have been my guardian angels ever since the first day. I cannot thank them enough for being such wonderful friends.

Thanks to Snigdha, Ramya(BJ), Vignesh, Supriya and Sanjay for always being there despite my incessant complaining and brooding and for inciting a laugh every time I needed it.

And my *Sashtanga Namaskaram* to Maa, Dad and Ammamma. For embracing all my idiosyncrasies and giving me the choice and the chance at every stage of life. It is to them that I dedicate this work.

Delft University of Technology Swathi Krishna
05-07-2012

Contents

List of Figures

List of Tables

Chapter 1

Introduction

Universally, noise is recognised as unwanted sound. Acoustic noise is considered to be a substantial cause of discomfort to humans and affects stealth operations by military vehicles amongst other repercussions. Industrial sectors like aerospace and automotive that are proximal to the cities are often bound by stringent noise regulations that cause a dip in their business profits which drive these enterprises to seek measures to abate noise related to their products. Few apt examples of large-scale consequences due to acoustic noise can be said to originate from the aircraft flying close to residential complexes and the rotating blades of wind turbines that are installed near urban areas to encourage the use of renewable energy sources. The demand for these products is ever on the rise and noise being an undesirable spin off factor, it is necessary to tackle and reduce this element thoroughly.

Figure 1.1: Noise sources

Noise generated from an aircraft is said to originate due to components such as engines,

rotors and airframe. With the advancement of jet-engines each day, the noise from the fans of the engine rises significantly too. Airframe comprises of all the wing and tail components along with landing gears which produces sound when it encounters flow. Airframe noise reaches high levels during landing with the full high-lift devices operational and the undercarriage down with engines at approach settings. This type of flow-generated noise is a serious problem in many engineering applications likewise. While research is carried out vastly to decrease engine and rotor noise, it is of prime importance to understand the sources of airframe noise if an attempt is to be made to curb it. A clear impression of the mechanisms involved when flow interacts with surfaces can be obtained through the study of aeroacoustics.

Based on the aerodynamic forces acting on the surfaces, Curle (1955) followed the work of Lighthill (1952) and proposed an acoustic analogy to predict the far field noise generated by unsteady flows interacting with a surface. Once the sources causing noise are discernible, they can be effectively tackled by varying the structural properties of the system or the flow itself.

1.1 Mechanisms of noise generation

The following cases give simplified examples for typical noise sources encountered on an aircraft:

Fluid structure interaction: When fluid flowing over a body impinges on the aircraft's structural components, it generates pressure fluctuations on the surface which translates as acoustic fluctuations in the far-field.

Turbulent shear flows : Free shear flows are inhomogeneous flows with mean velocity gradients that develop in the absence of boundaries. They transit to the turbulent regime much easily and promote the formation of large scale structures. When these coherent structures disjoin from the continuous fluid stream, they produce an oscillating force on the fluid that is propagated as acoustic pressure fluctuations in the far-field.

Trailing edge flow: In case of rotors or airfoil tips being exposed to heavy flow, sound is produced due to interaction of unsteady flows with a sharp-edged body.

1.2 Jets

Free shear flows are commonly found in natural and engineering environments. The turbulent plume of a cigarette or chimney, waterfall or a buoyant jet issuing from a volcanic eruption all illustrate the presence of free shear flows. An excellent case of turbulent shear flow in engineering can be seen in the wakes behind moving bodies, combustion processes and exhausts from engines; some of the many cases that can be found on an aircraft. These are free shear layers emanating from a solid boundary and spread outward, away from the structure. Mostly turbulent, this type of flow arises because of mean-velocity

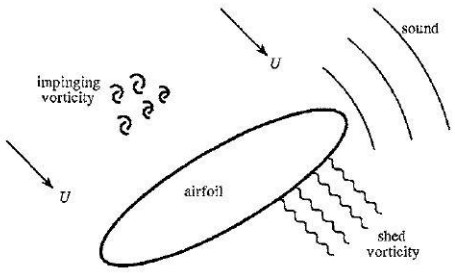

(a) Vortices impinging on a surface

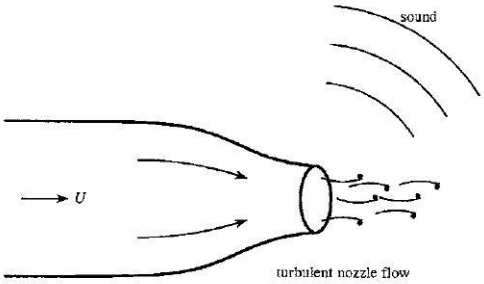

(b) Turbulent flow from a nozzle

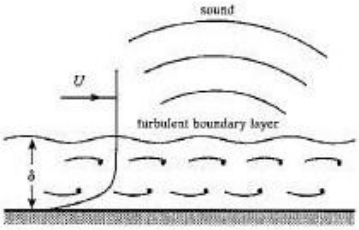

(c) Turbulent boundary layer

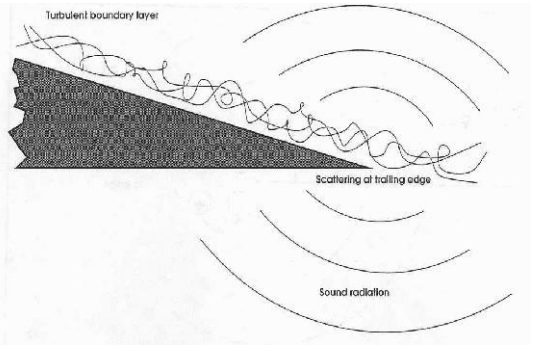

(d) Trailing edge

Figure 1.2: Noise mechanisms(Howe (2003))

differences. Turbulent flows are often characterized by large scale structures containing vorticity, those which when separated from the fluid, cause fluctuations at the boundary region which is transmitted to the flow. This pressure fluctuation is rendered as sound in the far-field. Depending on the edge geometry and flow conditions, the fluctuations produced by these vortices can vary from a ripple in the water to jet engine exhaust in an aircraft. So it is necessary to study this turbulent shear flow in detail.

Jets pose as a vivid test case to study many unresolved scientific issues of non-linear fluid dynamics and turbulence. Jets provide all the elements of a shear flow and are easy to simulate in laboratory environments. A wide range of turbulent scales can be observed in this self-similar flow. When the fluid flow from a jet interacts with a stable solid boundary downstream, it experiences fluctuating loads which are responsible for sound production. It is only logical to use a jet impinging on a flat plate as a benchmark to understand the different scales of structures, their behaviour and interaction between vortices and solids that generate sound.

Moreover, the case of impinging jets is not uncommon in engineering applications. It can be constantly encountered in cooling or drying of wind turbine blades, helicopter rotor-wash, industrial ventilation, combustion phenomenon amongst others. Advanced fixed-wing supersonic fighter aircraft which employ Short Take-Off and Vertical-Landing(STOVL) is another example for an application of impinging jets as the aircraft is provided with lift at zero forward airspeed from the exhaust jet impinging on the ground.

With this, it can be established that jets and specifically impinging jets are of high

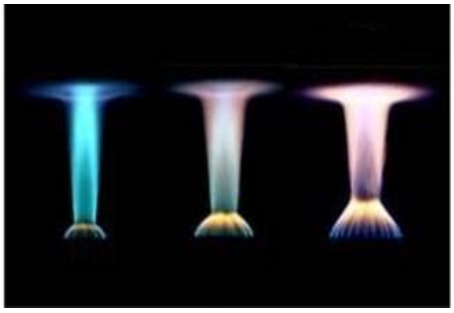

(a) Impinging flame jet (Choy et al. (2012))

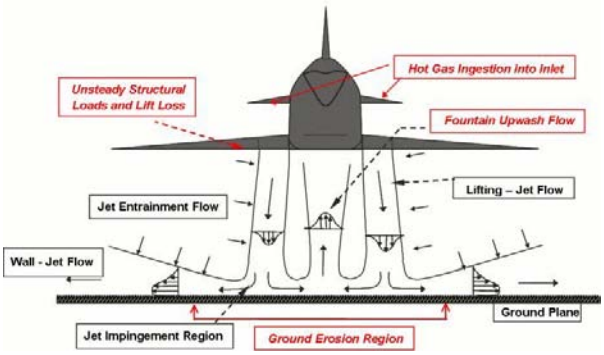

(b) Flow behaviour in a STOVL

(c) Water jet impinging on the rotor of a Turgo Turbine(ref:renewablesfirst.co.uk)

Figure 1.3: Some examples of impinging jets

importance from both points of view: academic understanding of sound production due to interaction of vortices produced in the shear layer with solid objects as well as practical applications which demands an in-depth study of the same.

Free and impinging jet aeroacoustics has been investigated plenty before in both experimental and computational domains. Several researchers like Popiel and Trass (1991), Cooper et al. (1993), Yule (1978), Becker and Massaro (1968) have performed extensive measurements on jets using flow visualization and hot wire techniques to discern the formation and development of a jet. They have defined the characteristics of vortical structures emanating from the shear layer and the velocity profiles along the jet. Later on researchers like Hall and Ewing (2005), Hall and Ewing (2006), Ho and Nosseir (1981), Nosseir and Ho (1982) used pressure sensors to interpret the pressure fluctuations produced by these large-scale structures. Some others like Landreth and Adrian (1990), Liepmann and Gharib (1992), Ganapathisubramani et al.,(2002) have used a much recent technique of Particle Image Velocimetry (PIV) to investigate $3D$ behaviour of the shear layer and transition patterns in streamwise and cross-sectional directions.

The intrinsic 3D nature of jets and the unsteady dynamical behaviour requires time-resolved, volume based techniques. Usually it can be achieved by implementing high resolution CFD techniques. It is the challenge in experimental domain that evokes interest here. Few researchers like Hori and Sakakibara (2004) have used stereo PIV to study the

3D vorticity field. These techniques though successful, left much to be desired with respect to obtaining accurate velocity fields, vorticity vector etc. in the 3D domain. However, the development of Tomographic PIV(Elsinga et al. (2006)) has presented a new technique to obtain better visualization and also more accurate velocity vector fields independent of the flow speed.

To this end, FLOVIST (*Flow Visualization Inspired Aero-acoustics with Time-resolved Tomographic Particle Image Velocimetry*) is a long term European project at the Delft University of Technology with the purpose of investigating aeroacoustic phenomena from an experimental point of view. The team recently carried out Tomo-PIV experiments with the aim of evaluating 3D pressure fields by following the Lagrangian approach to investigate the pressure fluctuations caused by a round jet impinging on a plate (Violato et al. (2011)). In addition to providing high quality flow visualization, the tomographic variant provides a more complete approach to obtain information about the pressure fluctuations generating sound, thus motivating its application in the field of aeroacoustics.

1.3 Research objective and overview

As a consequence of its applicability, there has been a considerable interest in characterizing the flow field of impinging jets and measurement of the noise produced. Researchers have investigated different influential parameters of an impinging jet individually and comparisons have been made for various Reynolds numbers, nozzle-to-plate distances and nozzle geometries. However, details of the pressure distribution and thereby the physical processes in different flow regimes for similar and varying nozzle-to-plate distances can only be partly inferred through collective works of several researchers. An exhaustive account of the flow field and comparison of pressure fluctuations caused by flow structures in laminar, transitional, turbulent and highly turbulent impingement has not been demonstrated by any single experimental campaign.

The first part of this thesis aims at capturing the pressure fluctuations on a solid surface caused by jet impingement between the stagnation and radial wall jet region. Experiments are carried out in different flow regimes-laminar to highly turbulent-in an attempt to improve the understanding of sources producing noise due to vortex-structure interaction. Phenomenological description is presented for each of the pressure distribution curves along with the aid of velocity contours obtained from PIV measurement database for impinging jets. Fourier decomposition of surface pressure fluctuations is carried out to relate the energy distribution in the spectra to specific events of an impinging jet that act as source mechanisms for sound production. The second set of measurements focus on measuring the far-field noise in a highly turbulent impingement at varying nozzle-to-plate distances to obtain an estimate of sound pressure levels produced in such regimes. A directivity test is attempted to understand the type of acoustic sources acting in an impinging jet.

For comparison purposes and also in light of the future work of the FLOVIST team, that aims to corroborate the reconstructed 3D pressure field from Tomo-PIV measurements with data from pressure sensors, the first set of pressure measurements are done

at similar experimental conditions. To ensure this comparability, Hot-Film Anemometry is employed to ascertain similar flow exit conditions for the two techniques.

Following the introduction in this chapter, the next chapter presents theoretical background of basic acoustics and acoustic analogies. The third chapter gives an in-depth account of jet physics, the mechanism of sound production in impinging jets and pertinent research available on them from a gamut of sources. The fourth chapter then gives a detailed report of the flow conditions, experimental techniques employed and the procedure followed for measuring surface pressure fluctuations. Succeeding which, the analysis of data obtained from those measurements are presented. The sixth chapter is devoted to interpretation of the results and discussing its implications. The final chapter is dedicated to conclude the findings and recommend possible future research relevant to the FLOVIST team.

Chapter 2

Theory on aeroacoustics

While acoustics is the study of propagation of sound in a medium, aeroacoustics is the study of sound generated by turbulent fluid motion or aerodynamic forces interacting with a surface. It deals with noise generated by flow structures including the effects of any solid boundaries in the flow. The first advance in the field of aeroacoustics was made by Sir James Lighthill who, prompted by the need for quieter engines, presented an acoustic analogy whereby the governing equations of motion of the fluid are coerced into a form resonant of the wave equation of linear acoustics. He manipulated flow governing equations and derived a wave equation based on pressure as the fluctuating variable and the flow variables contributing to the source of fluctuation. The sound field is obtained as a convolution of the Green's function and the sound source. The Green's function is the linear response of the reference flow, used to define the acoustical field to an impulsive point source. A brief theory is presented in the following subsections.

2.1 Basic acoustics

Sound can be understood as isentropic pressure perturbations in a fluid medium, propagated as sound waves. A sound source sets the nearest particles of air into vibration through which acoustic energy is transmitted from the source to the surroundings. These perturbations are deemed as noise when the waveforms are distorted with disorganized frequencies at high intensities. The sound pressure variations may have the form of a sinusoid which varies in both time and distance from the source,

$$p' = p(r, t) \tag{2.1}$$

where r is the distance from the acoustic center of the source. The peak value or the amplitude of the sound pressure decreases as the distance from the source increases. For a simple harmonic motion of a point source,

$$p'(r,t) = \frac{A}{r} cos\omega(t - r/c) \tag{2.2}$$

where A is the strength of the source and ω is the angular frequency in radians per second, $\omega = 2\pi f$. The ratio A/r is the amplitude of the local sound pressure disturbance which propagates with speed c, the time r/c is taken for the sound wave to travel to a point at distance r from the source. The magnitude of a sound signal can be expressed by the amplitude, p'_{max}, of the instantaneous sound pressure. However, the most frequently used measure of magnitude is the effective (sound) pressure, which is the root-mean-square value of instantaneous pressures over one period or an integral number of periods at the point.

$$p_e = \left[\frac{1}{T}\int_0^T [p'(t)]^2 dt\right]^{1/2} \tag{2.3}$$

where $p'(t)$ is as described in 2.2. The perturbations are often very small and propagate in a fluid at a speed given by-

$$c_0 = \sqrt{\left(\frac{\partial p}{\partial \rho}\right)_{s=s_0}} = \sqrt{\gamma RT} \ (for\ an\ ideal\ gas) \tag{2.4}$$

where R is the gas constant, $\gamma = \frac{Cp}{Cv}$ the specific heat ratio and T the absolute temperature in kelvin. The subscript $s = s_0$ indicates an isentropic process.

Acoustic measurements often require the presence of free-field conditions, which implies an environment free of reflections from obstacles such as wall or ground surfaces. For this purpose, special rooms have been designed in which the sound absorptive construction of the interior surfaces is such that practically no sound is reflected from them. These rooms are called *free-field chambers* or *anechoic chambers.*

Consider acoustic propagation as an isentropic perturbation of an equilibrium uniform reference state, described by the variables ρ_0, p_0 and v_0; the perturbed field variables can be rewritten as-

$$\rho' = \rho - \rho_0;\ p' = p - p_0;\ v' = v - v_0 \tag{2.5}$$

Assuming, $\rho << \rho_0$ and $p << p_0$, the governing equations of mass and momentum of ideal fluid can be linearised (Euler equations) and combined to obtain this well known wave equation-

$$\left(\frac{1}{c_0^2}\frac{\partial^2}{\partial t^2} - \nabla^2\right)[(p - p_0)\delta_{ij}] = q(x,t) \tag{2.6}$$

where, $q(x,t)$ is shorthand notation for the linear source term in the wave equation. In the absence of a source term, $q = 0$; the sound field is due to initial linear perturbations or boundary conditions.

The propagation of sound can described by D'Alembert's solution to wave equation, given by-

$$p' = F(n.x - c_0 t) \tag{2.7}$$

where F is determined only when the initial boundary condition and the source term $q(x,t)$ is known. In order to determine the source $q(x,t)$ from any measured acoustical field outside the source region, a physical model of the source is required. This is typical of any inverse problem in which the solution is not unique. The acoustic pressure at the listener position is generated by three sources, also shown in figure2.1-

- Monopoles- A source which radiates sound equally in all directions. The monopole source creates a sound wave by alternately introducing and retracting fluid into the surrounding area.
- Dipoles- A dipole source consists of two monopole sources of equal strength but with opposite phase and is separated by a small distance compared with the wavelength of the sound. While one source expands the other source contracts. The result is that the fluid (air) near the two sources move back and forth to produce the sound. A dipole source does not radiate sound in all directions equally. In the directivity pattern shown in figure 2.1b, there are two regions where sound is radiated very well, and two regions where sound cancels.
- Quadrupoles- Two opposite dipoles make up a quadrupole source. If two opposite phase dipoles lie along the same line they make a *Linear* Quadrupole source. In a *Lateral* quadrupole arrangement, the two dipoles do not lie along the same line (four monopoles with alternating phase at the corners of a square).

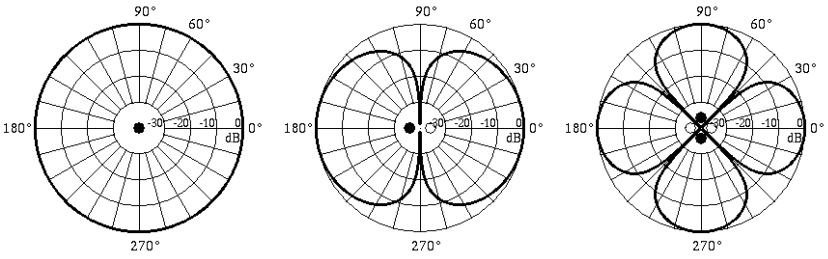

(a) Monopole source (b) Dipole source (c) Quadrupole source

Figure 2.1: Sources of acoustic emissions(ref:www.acs.psu.edu)

The true nature of these sources can not be accurately described by the linear theory as majority of the sound production is due to non-linear fluid motions and fluid-structure interactions.

2.2 Acoustic analogies

Acoustic analogies are applied to reduce sound sources originating in a flow to simple emitter types. They are therefore often also referred to as aeroacoustic analogies. In general,

aeroacoustic analogies are derived from the compressible Navier-Stokes equations (NSE). The compressible NSE are rearranged into various forms of the inhomogeneous acoustic wave equation. Within these equations, source terms describe the acoustic sources. They consist of pressure and speed fluctuation as well as the stress tensor and force terms.

Approximations are introduced to make the source terms independent of the acoustic variables. In this way, linearized equations are derived which describe the propagation of the acoustic waves in a homogeneous, resting medium. The latter is excited by the acoustic source terms, which are determined from the turbulent fluctuations. Since aeroacoustics is described by the equations of classical acoustics, the methods are called aeroacoustic analogies. The main analogies employed are as follows-

- Lighthill's analogy: considers a free flow, as for example with an engine jet. The non-stationary fluctuations of the stream are represented by a distribution of quadrupole sources in the same volume.
- Curle's analogy: is a reformulation of the Lighthill Analogy, which takes hard surfaces into consideration.
- Ffowcs Williams-Hawkings-analogy: is valid for aeroacoustic sources in relative motion with respect to a hard surface.

Brief details of the first two analogies are presented in this section.

Lighthill's eighth power law for free jets

In acoustics, small amplitude oscillations of a compressible fluid about a state of rest is considered. The basic equations follow from linearising the full equations of mass and momentum conservation and the equation of state. In general, it is adequate to assume the fluid to be Newtonian and to neglect all molecular relaxation and diffusion effects, so that stress on any fluid element consists of simply a normal pressure. Starting with the equations of conservation of mass and momentum, an approximation to Lighthill's theory of aerodynamically generated sound is given by-

$$\frac{\partial^2 \rho}{\partial t^2} - {c_0}^2 \nabla^2 \rho = \frac{\partial^2}{\partial x_i \partial x_j}(T_{ij}) \;\; where \;\; T_{ij} = \rho v_i v_j + p_{ij} - {c_0}^2 \rho \delta_{ij} \tag{2.8}$$

where ρ is the density and c_0 is the adiabatic speed of sound. Here p_{ij} is the stress tensor representing the stress acting in the i direction on a surface element having its normal in the j direction. We have $p_{ij} = p\delta_{ij} - \tau_{ij}$ where τ_{ij} is the viscous stress and p represents the sum of the static pressure and fluctuating pressure. Making an acoustic approximation, the resulting far-field solution reads as-

$$p(x,t) = \frac{x_i x_j}{4\pi c^2 |x|^3} \int_v \left[\frac{\partial^2}{\partial t^2} T_{ij}(y,t) \right] dV \tag{2.9}$$

The t in the equation 2.9 represents time delay, inside the parentheses of the integral, it is to be considered as $t - |x - y|/c$ and x, y are the co-ordinates of the source region.

Furthermore, the approximation $T_{ij} = \rho_0 v_i v_j$, where ρ_0 is mean density, is customarily made in low Mach number and high Reynolds number flows with only negligible temperature variation. Using this, the characteristic velocity V and the characteristic length L of the jet,

$$T \sim \rho_0 V^2 \tag{2.10}$$

$$\frac{\partial}{\partial t} \sim \frac{V}{L} \tag{2.11}$$

Therefore,

$$p \sim \frac{x_i x_j}{4\pi c^2 |x|^3} (\frac{V}{L})^2 \rho_0 V^2 L^3 \tag{2.12}$$

and the pressure scales as-

$$p \sim \rho_0 \frac{V^4}{c_0^2} \frac{L}{x} \tag{2.13}$$

The total acoustic power is the intensity integrated over a spherical surface of radius x, where intensity is $I \sim p^2$ and is given as-

$$W \sim \rho_0 \frac{V^8}{c_0^5} L^2 \tag{2.14}$$

The total acoustic power thus scales as the eighth power of jet velocity. This equation is Lighthill's eighth power law for jet noise. It is strictly only true for low speed flows, because it is assumed that the source is compact. At higher speeds, the characteristic frequency of the source increases and interference effects between different regions of the jet become important.

Curle's sixth power law for flow-structure interaction

Compact bodies radiate a dipole sound field associated with the force which they exert on the flow as a reaction to the hydrodynamic force of the flow applied to them. When flow instabilities interact with a solid surface, pressure recovery by fluid acceleration is prevented by the presence of the boundary. Pressure fluctuations at the surface are in turn transmitted back to the fluid and they partially propagate as sound. An extension to Lighthill's general theory of aerodynamic sound so as to incorporate the influence of solid boundaries upon the sound field was made by N.Curle in 1955. It was shown that the influence of the solid boundary is two-fold:

1. Sound waves are reflected and diffracted at the solid boundary.

2. The quadrupoles will no longer be distributed over the entire space but only throughout the region external to the solid surface where there is a resultant distribution of dipoles

at the boundaries. Dipoles are likely, since in acoustics they correspond to externally applied forces and such forces are present between the fluid and the boundaries.

Curle generalized the solution of Lighthill equation to include a foreign body embedded in the unsteady flow, leading to a far field approximation as:

$$p(x,t) \sim \frac{\rho_0}{|x|}\int_s [\dot{u_n}]\,dS + \frac{x_i/c}{|x|^2}\int_s \left[\frac{\partial}{\partial t}(f_i + \rho u_i u_n)\right] dS + \frac{x_i x_j/c^2}{|x|^3}\int_v \left[\ddot{T_{ij}}\right] dV \tag{2.15}$$

where the time derivatives are designated with a dot. Furthermore, if the embedded surface is stationary or in rigid, parallel motion, then $\dot{u_n} = 0$, the first term in 2.15 becomes zero. The third term represents the quadrupole contribution of the flow which represents the direct contribution of the flow instabilities to the noise. Following Lighthill, the second integral which is the surface dipole contribution, was estimated by Curle that leads to sound power being radiated as a sixth power law:

$$W \sim \rho_0 \frac{V^6}{c_0^3} L^2 \tag{2.16}$$

The dipolar term represents the fluctuating normal and tangential stresses at the wall induced by hydrodynamic fluctuations near the body. This clearly shows that the acoustic power is greater in the presence of dipoles than with quadrupoles. Curle suggested that the dipole character of a source would overwhelm the quadrupole source at low speeds. Due to this domination of the dipole sources, flow-structure interaction causes much more noise levels than free shear flows.

Lighthill's eighth power law can be associated with free region of the jets while for flow impingement, clearly the presence of solid boundaries ensure dipole distribution which commands over the quadrupolar quantities of the free jet region.

Chapter 3

Jet physics

Understanding the anatomy of round impinging jets is important in various applications. Instability of the free shear layer downstream of the nozzle mouth, large scale toroidal structures, turbulence development and stagnation point flow behaviour are of fundamental interest in these physical flow phenomena. A series of experiments have been performed on a low-speed circular jet impinging on a plate with the aim of finding out the pressure distribution in the impingement region and in the subsequent radial wall jet. This chapter presents the fundamentals of jets which provides a base to the reasoning and interpretation of the experimental results obtained in the further chapters.

3.1 Circular free jets

A jet is an outflow of fluid that is projected into a surrounding medium, through a comparatively smaller opening such as an orifice or nozzle. Jets are made up of intrinsic structures that have been of broad interest for the wide range of consequences it tends to induce.

Whenever a moving fluid enters a quiescent body of the same fluid, a velocity shear is created between the entering and the surrounding fluids, causing turbulence and mixing of layers. Consequently, the shear layer and the jet spreads laterally outward and the jet velocity decreases downstream. The properties of a turbulent flow greatly depend on the geometry of the flow domain and on the type of forces acting on the fluid. In this thesis, the focus is directed towards an unforced jet emerging from an even-contoured round nozzle geometry which impinges on a flat plate placed downstream of the flow.

The main aspect of jets is the vorticity, $\Omega = \nabla * u$ where u is the velocity field, which gives a local measure of the rotation of the fluid. Vorticity is generated near the jet exit (as explained later in this section) and its convection and diffusion into a narrow portion of the surrounding medium gives the defining appearance to a jet. The onset of flow instabilities and the resulting amplification of the fluctuating vorticity causes a clear confinement of vorticity which can be visualized by various means. The jet's flow regime

is characterized by jet exit velocity V, jet diameter at nozzle or pipe exit D, and the Reynolds number $Re = VD/\nu$ where ν is the kinematic viscosity.

Mixing between a turbulent jet and its surroundings occurs in two stages; one by bringing relatively large amounts of fluids together and the second by small-scale velocity fluctuations that accelerate mixing at a molecular level. The deformations in the interface of rotational and irrotational fluid which possess the largest scales move at a certain speed into the surrounding fluid. Propagation of these structures are coherent and easily recognizable which leads to their name *coherent structures*. These structures reoccur over space and time which implies that they have a certain impact within the flow field. It is therefore of prime importance to understand the formation, interaction, merging and breakdown of these coherent structures.

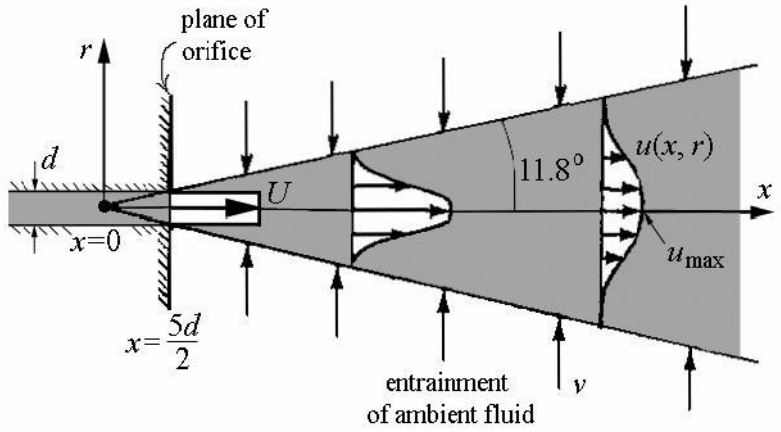

Figure 3.1: Profile of a turbulent jet

When jets enter into a quiescent fluid of the same density, the original kinetic energy of the jet is gradually dispersed in the turbulent mixing region of the jet. The jet is separated from the surroundings by a distinct surface discontinuity. The surrounding fluid is entrained into this boundary increasing the mass of the fluid and decreasing its velocity, thus keeping the momentum constant. In this way, the envelope containing turbulence caused by the jet adopts a nearly conical shape. It means that the radius R of the jet is proportional to the distance x downstream of the fluid. The opening angle is always the same, regardless of the properties of the fluid or the aperture through which it entrains. Following Prandtl's hypothesis, Tollmien (1926) calculated the half-angle of the cone of a gaseous jet to be nearly 12° or 24° full angle (Horn and Thring (1956)). Taking the tangent of the half-angle of a jet, $tan(12°) \simeq \frac{1}{5}$, gives the proportionality relation of the jet radius with the downstream distance x.

$$R = \frac{1}{5}x \tag{3.1}$$

From figure 3.1 it can be seen that the point of origin of the *turbulence cone* is not at the nozzle exit but from a distance of $5D/2$ into the pipe where D is the diameter of the nozzle. This point of origin is called the *virtual source*.

Previous experimental investigations (eg. Ko and Chan (1978)) have revealed that a jet is self-similar, i.e. the jets stretch as they move downstream but they maintain their cross

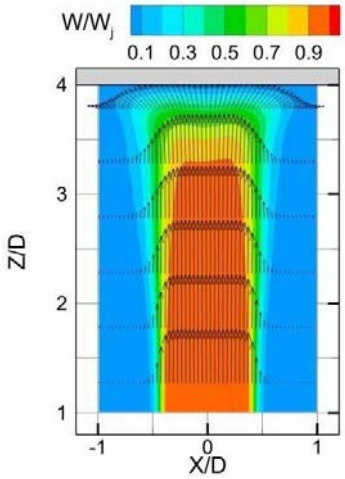

Figure 3.2: Velocity profile in a jet(Violato and Scarano (2011))

sectional appearance identical in time. The velocity profile across the jet exhibits a nearly Gaussian shape.

PIV experiments conducted by Violato et al., shows the profile of velocity distribution at different distances from the nozzle exit. It can be seen in figure 3.2 that the velocity remains constant in the potential core region and slowly transforms into a bell curve beyond it.

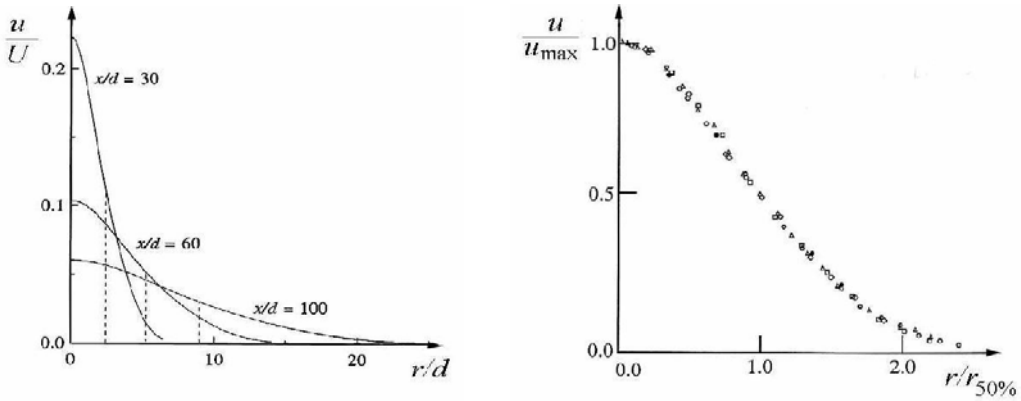

(a) Radial profiles of mean axial velocity

(b) Mean axial velocity along radial distance

Figure 3.3: Velocity profiles in a turbulent jet(Pope (2000))

Figure 3.3 shows the velocity profiles of a jet with respect to distances from the nozzle exit. It can be clearly observed from these figures that with increasing axial distance, the jet decays i.e. the centreline velocity U_0 decreases and spreads circumferentially. The mean velocity profiles change as the jet moves downstream but the basic shape of the profiles do not change. The curves shown here are adapted from the data of Hussein et al. (1994) measured at $Re = 95500$. Beyond the developing region ($x/D = 30$) the

profiles of mean velocity U normalized with the exit centreline velocity collapse into a single curve. Figure 3.3b shows mean axial velocity versus radial distance in a turbulent round jet at $Re \approx 10^5$. The velocity is scaled by the maximum value at the center of the jet, and the radial distance by $r_{50\%}$: the distance at which the velocity drops to half of its maximum value. It can be concluded from these figures that the mean velocity profile becomes self-similar.

The most basic case is that of a *free jet* penetrating into an otherwise dormant fluid. This thesis aims to investigate a case of a homogeneous *impinging jet* on a flat plate placed orthogonally to the jet axis.

Vortices

Vortices in a jet adopt the classical definition of flow field accompanying a concentrated, continuous, coherent distribution of vorticity which is uniform in the direction of vorticity vector and which grows in scale by viscous diffusion. Yule (1978), performed extensive research on mixing layers of a round jet and described the properties of vortices in a jet. He insists on the use of the term *vortex* only when the rings are firmly established, otherwise preferring the term *eddy*, described as vorticity containing region of fluid which can be identified as a moving coherent structure in a flow.

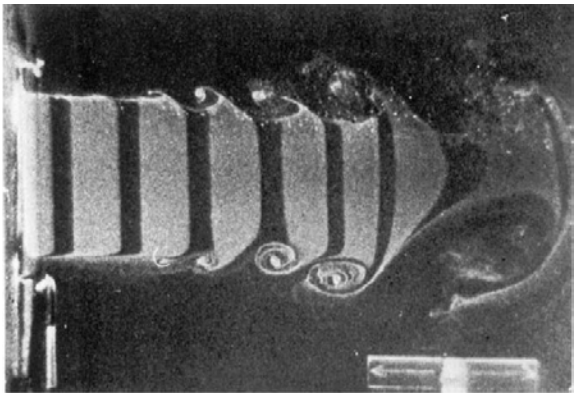

Figure 3.4: Development of a round jet: A 2-D impression of the round jet at Re=9000.(Yule (1978))

It could be clearly visualized from the work of Popiel and Trass (1991) who photographed smoke streaks that carried the coherent structures with it, that the jet starts off as an initial instability. The air exiting from the trailing edge of a convergent nozzle is confined in a boundary of a thin laminar shear layer that is intrinsically unstable. As discussed by Roshko (1981), this laminar shear layer exhibits the features of a Kelvin-Helmholtz instability. From this instability, a primary structure is developed. The laminar shear layer leaving the nozzle immediately forms waves of increasing amplitude as shown in the figure 3.4.

It can be further observed in the same figure that the wave takes a sinusoidal form for small Reynolds numbers. When Reynolds number increases from an order of 10^2 to 10^3, the instability evolves as a helix and develops as an axisymmetric wave. At Reynolds numbers of the order of 10^4, the axisymmetric structures are large scale vortex puffs(Crow

and Champagne (1971)). A small lump of vorticity contained fluid separates from the top crest of this initial instability wave and begins to convect downstream. It magnifies in size and strength to form the toroidal vortex that is proved by many researchers to be the source of acoustic noise in jets.(Crow and Champagne (1971), Brown and Roshko (1974) etc.).

As this initial toroidal vortex convects to a sufficient distance downstream, a new vortex is formed at the nozzle end which causes a significant contraction of the potential jet core, producing a slight pulsation in the pressure action upstream. The potential jet core is the central portion of the flow in which the velocity remains the same as that at the jet exit which eventually disappears as the shear layer surrounding it on all sides begin to converge towards the axis. This action causes a simultaneous appearance of a new instability wave and in turn a vortex birth around the entire circumference.

Vortices can also be clearly visualized in the figure 3.5 as presented by Violato and Scarano (2011). They detected vortices using the λ_2-criterion and convective velocities are evaluated at each time-instant. It shows a temporal sequence of the flow field at Reynolds numbers of 5000 with snapshots separated by a normalized time $\Delta t = 0.61$. They came to observe that shedding of vortices occur at a normalized distance of $1 - 1.5$ which also agrees with the findings of Liepmann and Gharib (1992) and that the core of the jet induces an outward flow in the leading edge and inward flow at the trailing one, which increases as the vortex ring grows and is convected downstream.

Vortex Pairing

When a toroidal vortex is triggered too early by any internal or external disturbances, the vortex is weaker and is usually engulfed by the earlier larger vortex. This is known as vortex pairing. Winant and Browand (1974) extensively studied the vortex pairing phenomenon during the development phase of the jet. According to them, as the unstable waves grow, the fluid rolls up into discrete two-dimensional vortical structures when it mixes with the surrounding fluid. These turbulent vortices interact by rolling around each other, forming a single vortical structure, with approximately two times the spacing of the former vortices.

Violato and Scarano (2011) give graphic details about vortex pairing phenomenon through time-resolved 3D measurements using Tomographic PIV. In the figure 3.5 it can be clearly seen that in the downstream of the jet, the shed vortices entwine with the neighbouring vortices that causes frequency halving. For better explanation, they have numbered the vortices in the temporal sequence posed. The flow induced by the earlier vortex(e.g. vortex 3) produces axial and radial accelerations directed towards the jet core. As a result, the newly shed vortex(vortex 4) begins to stretch along the axis increasing its convective velocity and decreasing its diameter. Due to this outward motion induced in the flow, the older vortex stretches and increases its diameter while lowering its convection velocity. The difference in convective velocity causes a reduction in the spacing between the two vortices and ultimately leads to pairing of the two structures. The pairing occurs repeatedly and influences the growth of the mixing layer. The average passing frequency of the primary vortex structures are expressed in the form of the Strouhal number-

$$St = \frac{f\theta}{V} \tag{3.2}$$

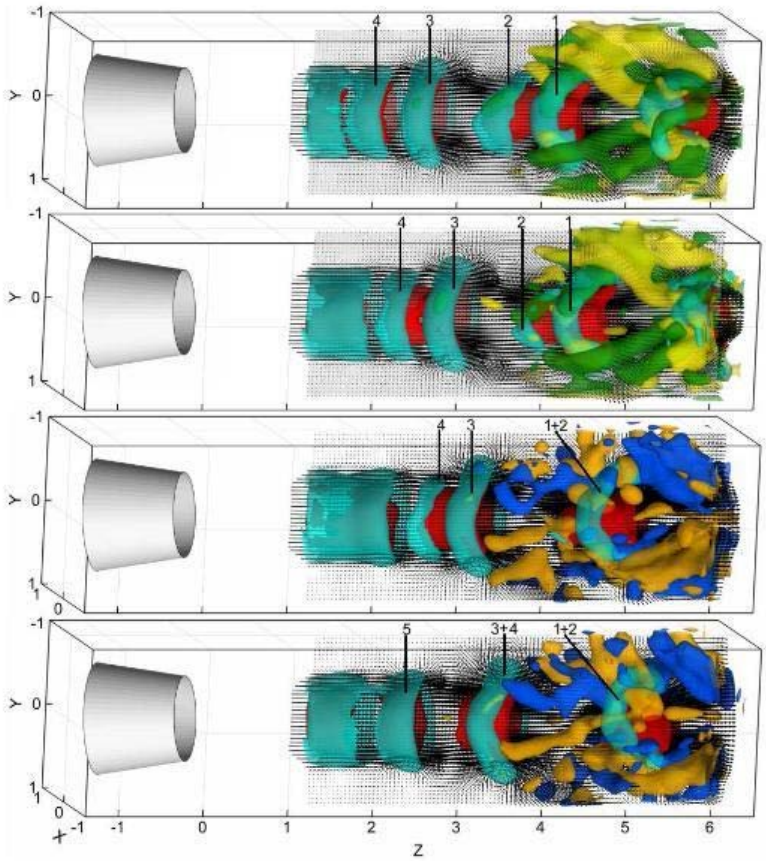

Figure 3.5: Time sequence visualization of the circular jet. Time separation between displayed images t=0.61. [Violato and Scarano (2011)]

where f is the frequency of vortex shedding, θ is the characteristic length scale of the flow and V is the velocity of the fluid. In this case, the characteristic length scale is the momentum thickness of the boundary layer at the nozzle mouth. Smoke wire experiments performed by Popiel and Trass reveal that beyond a distance of $1.5D$, the developing toroidal vortex grows and can be compared to the nozzle radius. Due to this increase, the vortices decrease their passage frequency which result in coalition of the later vortices with the earlier ones. As found by Crow and Champagne (1971), for Reynolds numbers in the range of 10^4 to $5 * 10^4$, a constant Strouhal number of 0.3 can be inferred based on the jet diameter and frequency of the passing vortices.

Vortex Spacing

According to Armstrong et al. (1976), the scale of the coherent structures is roughly proportional to the local width of the shear layer, which increases linearly with distance H from the nozzle. It was also assumed that separation distance between two neighbouring vortices λ is proportional to the distance H. They inferred a relation of the form-

$$\lambda/D = 0.55H/D \tag{3.3}$$

It could also be represented as-

$$\lambda/D = V_c/fD = (V_c/V)/St \tag{3.4}$$

where V_c is the vortex convection velocity, V is the jet exit velocity, f is the vortex passing frequency and St is the Strouhal number as defined in equation 3.2.

Transitional jets

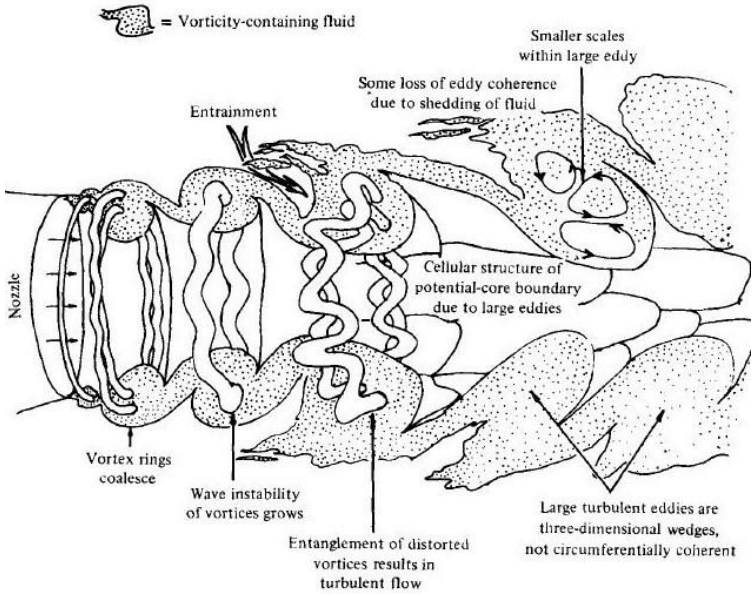

Figure 3.6: Structure of a transitional jet as presented by Yule(1978)

The first set of experiments in this thesis are conducted in the transitional region which calls for a deeper understanding of this regime. The figure 3.6 from Yule (1978) gives a clear representation of transitional jets at $x \approx 3D$. The fluctuating velocity field at this value of x has not yet attained all the properties of a fully developed turbulent flow which begins beyond $x \approx 4D$. The natural instability of the initial laminar shear layer produces a street of vortex-ring-like vorticity concentrations. As these rings move downstream, they generally coalesce with neighbouring rings, so that the scale and separation of the vortex rings increase with the distance from nozzle. Yule observed a gradual increase in the radial velocity fluctuations with distance from the nozzle downstream due to the orderly wave deformations of the cores of the vortex rings. They could observe from one upto-atleast three regions of coalescence in the transition region depending on the Reynolds number of the jet and the boundary layer thickness of the nozzle. Coalescence disappears downstream of transition. Just before turbulence begins, only the vortex rings which have core deformations larger than a critical size coalesce, which produce enhanced vorticity stretching and small scales of motion. These entangled vortices are seen as large eddies in the downstream of transition. The ring vortices and peak-frequency halving associated with vortex pairing are not observable in regions beyond transition. The initial orderly, helical interface between the jet and ambient fluid entraining into the vortex becomes perturbed and diffuse as new fluid enters and coalescence takes place.

3.2 Impinging jets

The impinging jet can be characterized into four different flow regions as shown in the figure below. These flow regions are described below.

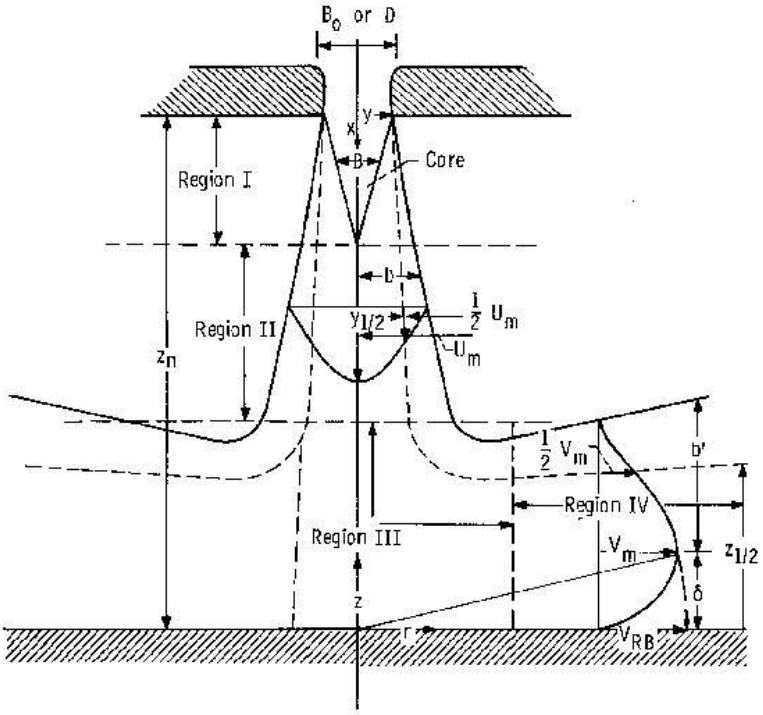

Figure 3.7: Characteristic regions of impinging flow(Gauntner et al. (1970))

Region 1 is the region in which the flow establishes itself. It extends from the nozzle exit to the apex of the potential core, where in the mean velocity is almost uniform. When the shear layer spreads, it merges from all directions because of which the potential core eventually disappears. The velocity profile is constant here.

Region 2 is the region in which the established flow propagates in the direction of the jet beyond the potential core. The potential core is surrounded by a mixing layer that remains nearly laminar. The mixing layer then spreads linearly into both jet and the fluid. The flow passes through a transition region and finally into a fully developed flow.

Region 3 is the region of impingement. Here the jet is deflected from the axial direction due to the presence of a solid wall. Here the vortices impinge on the plate which causes a fluctuation in pressure over the wall.

Region 4 is the wall jet region. This region consists of accelerating flow in the radial direction along the surface of the wall. Here the flow thickness increases which in turn begins to form the boundary layer on the solid surface. Adverse pressure gradients in this region can lead to separation of the radial flow.

Various factors like the nozzle-plate distance, nozzle geometry, Reynolds numbers cause different effects upon impingement as the vortices that roll up in the mixing region and

interact with the plate depend on these factors. This region of interaction causes enormous fluctuations of instantaneous local skin friction and heat or mass fluxes. Popiel and Trass, who measured at a nozzle-plate distance of $H/D = 1.2$, found that that the toroidal vortices reach the plate at a radial distance of $r/D = 0.7 - 0.9$. The vortex begins to stretch as the plate is approached. Its diameter increases until the velocity component perpendicular to the wall tends to zero and the radial velocity begins to increase. They also found ring-shaped eddies at the wall induced by the large scale toroidal structures which are deviated in the radial direction. These eddies eventually follow the same path as the toroidal structures by elongating and diverging in the radial direction. By the time these structures reach a radial distance of $r/D \approx 2$, there is a transition region where the eddies and the vortices merge together to form a fully developed turbulent radial wall jet. Similar unsteady separation phenomenon was captured earlier by Didden and Ho (1985) in a forced impinging jet. They observed that the vortex rings formed in the shear-layer approach the plate approximately 0.9 diameters from the jet centreline and then travel radially outward over the surface causing formation of secondary vortex rings near the wall. These secondary vortex rings eventually were ejected from the surface approximately 1.5 diameters from the jet centreline. They then wrapped around the primary vortex rings which led to the breakdown of both ring structures.

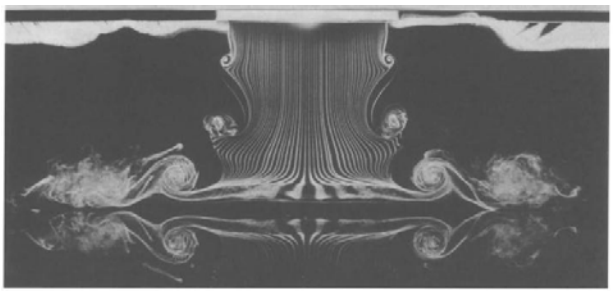

Figure 3.8: Impinging flow structures[Popiel and Trass (1991)]

The above image as captured by Popiel and Trass reveal the vortex formation and pairing along with impingement and radial divergence of the structures. They found that in regions of $H/D > 2 - 4$, the instantaneous stagnation point of the impinging jet moves about the geometrical stagnation point as observed by Yokobori et al(1979). Beyond $H/D > 4$ the flow in the impingement region becomes chaotic and is dominated by large scale turbulent fluctuations with imposed fine scale turbulence.

3.3 Flow-field characterization in jets: Research until now

The study of impinging jets has attracted a lot of key research due to its structural configuration. As such it is necessary to investigate the effects of different geometrical and fluid property parameters on the jet behaviour. Researchers have characterized the flow field produced by turbulent round impinging jets because these flow configurations play a major role in many applications such as heat transfer, noise emissions etc.. Previous investigations have shown that the heat transfer produced by round impinging jets is affected by a number of parameters including the nozzle-to-plate distance, the jet Reynolds number and the geometry of the nozzle (Viskanta (1993)).

Early studies were conducted in order to understand the evolution and progression of structures in a jet by researchers like Becker and Massaro (1968) and Yule (1978). They investigated round jets with flow visualization, smoke photography, hot-wire and similar techniques to characterize the intrinsic development of jets. The evolutionary phenomenon of instability, vortex ring formation, coalescence of ring vortices and disintegration of eddies was studied. Their work has provided a clear understanding of the structural intricacies of a free jet.

Popiel and Trass (1991) reaffirmed the theories by providing a clear picture of the structural formation of round free and impinging jets with the help of detailed images from flow visualization. Interaction between the ordered large scale toroidal vortex structures and the normally impinged flat plate is qualitatively defined. They carried out the examination in the potential core of the jet at $H/D = 2 - 4$ where the velocity profile is still constant and the turbulent flow has not commenced. Their work provides an estimate of the radial position on the wall at which vortices reach the plate. Images provided by them showed the clear range of the radius of $r/D = 1 - 2$, a transition zone in which the toroids abruptly merge with the developing eddies and the flow develops into a turbulent radial wall jet. It was noted that at low H/D distances, the toroidal structures are larger and beyond $H/D = 4$ the flow in the impingement region becomes very chaotic and is dominated by large scale turbulent fluctuations.

These investigations have also shown that the transition in scaling of heat transfer is produced by the impinging jet in the region of $r/D \leq 1.5$ and the turbulent region begins from $r/D \geq 2$. Yan et al. (1992) compared the profiles of Nusselt number produced by impinging jets exiting a long pipe with Reynolds number of 23000-70000 and nozzle-to-plate distances of 2-10 diameters. They found that the profiles of the Nusselt number in transition region between stagnation and wall jet region did not collapse nearly as well for jet with nozzle-to-plate distances of 2 and 4 diameters which has secondary heat transfer peaks, as they did for jets with nozzle-to-plate distances of 6 and 10 diameters, without secondary peaks in the heat transfer.

Cooper et al. (1993) compared measurements of the flow field in the radial wall jets at Reynolds numbers of 23000 and 70000 and nozzle-to-plate distances of 2 and 3 diameters. A comparison of radial growth with jet half-width, variation of velocities along the symmetry axis, dependence of the near-wall axial mean and turbulent velocities on nozzle-to-plate distance and radial turbulent velocity profiles for different nozzle-to-plate distances were shown. It was noted that as the height of the jet above the impingement point increased, more mixing occurred before the jet struck the plate. The turbulence levels noted were higher and the impingement zone of the jet is at a distance of 2-3 diameters from the stagnation point.

Many have characterized the development of large scale structures in the near field of the radial wall jets, produced by impinging jets with nozzle-to-plate distances less than 4 diameters. (e.g. Popiel and Trass (1991) , Didden and Ho (1985), Landreth and Adrian (1990)). These investigations showed that the passage of the large scale structures originally formed in the shear layer caused a separation of the near-wall flow at $r/D \approx 1.4 - 2$. Although Didden and Ho (1985) examined the development of a forced jet, they found that the large scale structures approached the wall at $r/D = 0.9$ and then radially spread along the wall. The unsteady pressure gradient imposed by the passage of these

structures caused secondary regions of counter-rotating vortices to form in the near wall flow beneath the ring structures. The secondary vortices were ejected faster than the primary structures and were ejected from the near wall region at $r/D \approx 1.4$ similar to a lone vortex ring impinging on to a wall. They observed that the secondary vortex ring appeared to wrap around the primary ring and an instability causes the breakdown of both rings shortly. Other researchers like Popiel and Trass (1991) used flow visualization technique on a natural jet to find that the ejection of secondary vortices appeared to occur further downstream than in a forced jet.

Many researchers have examined the development of the structures in free jets exiting contoured nozzles varying with Reynolds numbers (e.g Liepmann and Gharib (1992)). They concluded with their investigation that the development of structures depended on the thickness of the boundary layers in the nozzle with varying Reynolds numbers. They noted that the location of initial instability moved towards the nozzle as the Reynolds number of the jet increased but did not compare the development of the three dimensional structures downstream. The thickness of the near wall region decreases with increase in Reynolds number. This has an effect on the shear layer of the jet and in turn the three dimensionality of the structures in radial wall jets.

Hall and Ewing (2005) opined that investigation of three dimensionality is better done with two-point and two-time correlation than by flow visualization of the flow field because the flow is dispersed radially outward and has a characteristic height significantly smaller than the jet outlet diameter. Also Ho and Nosseir (1981) measured the two-point and two-time correlation of semi-compressible impinging jets, and showed that the impingement of the periodic structures formed in the jet shear layer were also responsible for acoustic resonances.

Another researcher to have performed detailed two-point and two-time correlation measurements was Kataoka et al. (1982). He measured at nozzle-to-plate distances of 6 diameters and found that the flow structures impinging onto the plate were highly three-dimensional and the potential core ended at roughly $6D$.

Hall and Ewing (2006) also investigated two-point and two-time correlation of fluctuating wall pressure at two Reynolds numbers 23000 and 50000. Comparison of the three dimensionality and development of the large scale structures in the near field of radial wall jet as the Reynolds number differed indicated that the large scale structures were more two-dimensional, more periodic and more prominent in higher Reynolds number flow. They characterized the three-dimensionality of the large scale structures exiting from a long pipe with nozzle-to-plate distance of 2-4 diameters in a turbulent regime of Re=23000. It was found that the instantaneous structures were not axisymmetric and the structures became more three-dimensional as the nozzle-to-plate distances increased.

It can be seen from extensive literature that different techniques have been employed for characterizing jets. Flow visualization techniques, hot-wire anemometry, pressure sensor measurements, Laser Doppler Velocimetry, Particle Image Velocimetry amongst others have been employed for conducting experiments. Each of these techniques have yielded to the gamut of knowledge available on jets.

Of the other techniques currently evaluating the pressure fields from PIV measurements, investigation of unsteady aerodynamic loads and the resultant sound production is of high

interest. This has been acknowledged in the review article of Jordan and Gervais (2008) where the role of time-resolved PIV is emphasised.

Most recently Violato et al. (2011) consolidated the experiments with a 3D planar configuration (Elsinga et al. (2006)) from which emerged that the three-dimensional velocity field must be considered to correctly evaluate the instantaneous pressure field using a Lagrangian approach. In this aspect, the tomographic variant provides a more complete approach in obtaining information about the sound generation. As such thin tomographic PIV experiments are carried out by Violato et al., in the water jet facility of the Delft University of Technology at low Reynolds number to evaluate the pressure field on the impinged plate. The pressure field obtained is used as input in Curle's analogy for aeroacoustic prediction.

In addition to the surface pressure measurements to enhance the understanding of topology and dynamics of jet structures for various flow conditions that generate sound, direct far-field investigations have been conducted to determine the noise quantities for different configurations of flow and impingement parameters. Nosseir and Ho (1982) investigated the noise generation mechanisms in subsonic impinging jets. Cross-correlations of near-field measurements close to the lip of the nozzle and the microphone were used to determine the acoustic propagation paths. The frequency spectra showed two peaks corresponding to the impingement of large coherent structures and the initial instability of the free shear layer. These two mechanisms were concluded to be the sources of noise generation in impinging jets, both of which followed separate acoustical paths.

The aerodynamic sound generated by a jet impinging normally and obliquely was studied by Shen and Meecham (1993). Microphones were used to conduct a directivity test at different nozzle-to-plate distances, nozzle sizes and jet speeds. They observed a clover leaf, quadrupole directivity pattern suggesting such sources have approximately fixed orientation. A consistent minima was found at $45\,^{\circ}$, measured from the plate while the maxima was observed at $0\,^{\circ}$ and $90\,^{\circ}$. This was believed to be the first experimentally observed quadrupole directivity pattern in connection with Lighthill's quadrupole source theory. Cross-correlations with far-field microphones when the pressure transducer was located at about $1D$ from the jet axis, indicated that the major source of the jet impingement noise is located at this position. Also cross-correlation between microphones and hot-wire measurements that were conducted at $2mm$ above the plate encouraged the authors to believe that the quadrupole noise source existed at a location above but very close to the plate. They theorised that there exists an organized coherent structure near the noise source location on the plate, here the vortical motion of the flow is organized with a directed orientation, generating a quadrupole sound. Beyond the area of organized structures, the vortical motion of the turbulent flow was expected to be randomly oriented so no quadrupole-like far field is apparent due to this class of vortices.

A quantitative report on the sound power levels encountered in an impinging jet is given by Petrie (1974). Experiments were conducted to observe the effects of different nozzle diameters, nozzle-to-plate distances and exit velocities. It was found that at low velocities and large nozzle diameters the sound power levels continuously increased as the nozzle-to-plate distance decreased. It was seen that the impinging jet produced $7dB$ more than a free jet. For smaller diameters and high velocities, an increase of $27dB$ was observed as compared to a free jet. It was concluded that this large increase can be avoided by inclining the boundary to the jet axis.

With this background of jets, experiments are conducted as described in the next chapter and more detailed description of impinging jets will be presented along with the results in chapter 6

Chapter 4

Experimental set-up and measurements

The experiments are conducted in the semi-anechoic chamber described in section 4.2.1 in the Acoustics lab of Delft University of Technology. The purpose of these experiments is to investigate the near field pressure variations caused by a round jet impinging on a plate at various Reynolds numbers and nozzle-to-plate distances. The pressure profiles thus obtained over an area is used to understand the source mechanisms in jets that play an important role in the sound generation. Priorly obtained results from Tomographic Particle Image Velocimetry is used to explain the vortex dynamics. An account of the PIV set up can be found in Appendix A. This is followed by acoustic measurements in the far-field of the impinging jet. The main methods employed to find the pressure fluctuations are: microphone and pressure transducer. Hot-Film Anemometry measurements are conducted to verify the velocity profile of the air jet in order to establish that the two experiments are conducted at similar exit conditions. The experiments are conducted at 4 velocities between Mach 0.02-0.22.

4.1 Techniques

4.1.1 Hot Film Anemometry

An anemometer is basically a fluid velocity measuring device that is incorporated with a sensor. An anemometer that works on the principle of change in its temperature properties for measuring velocities falls into the category of Thermal anemometry in which Hot-wire and Hot-Film Anemometry are most common.

The hot-wire or film is a thin sensor(in the order of micrometers) which makes use of the principle of heat transfer from a heated surface which is dependent upon the flow conditions passing over it. The sensor is made up of an electrically conducive metal. When current passes through the sensor, electrical energy is converted to thermal energy

leading to a rise in the temperature above ambience. It is known that the resistance of a metal is dependant on its temperature. Therefore, when the temperature increases, the resistance of the wire also increases. When fluid from a source flows over the wire, it changes the temperature distribution across it due to convective heat transfer. The rate at which this heat is convected is directly related to the velocity of the fluid flowing over the sensor. This produces a new equilibrium in temperature and the resistance of the metal. In order to compensate the changes in resistance, the voltage is varied so as to maintain the temperature constant.

Of the different working principles, the system used for the current set of experiments is a Constant Temperature Anemometer(CTA). It is essentially made up of a Wheatstone bridge, of which the fourth resistance is the thermal sensor(refer figure 4.1). The other two legs of the bridge have identical resistance. An amplifier tries to match the resistances of the lower legs of the bridge (keeps the error voltage zero). It adjusts the bridge voltage such that the current through the probe heats it to the temperature which gives the selected resistance. When the sensor probe is in the path of the flow, the fluid tries to cool the hot-sensor. In order to maintain the temperature (and thereby resistance) constant, the bridge voltage is increased. Thus faster the flow, higher the voltage.

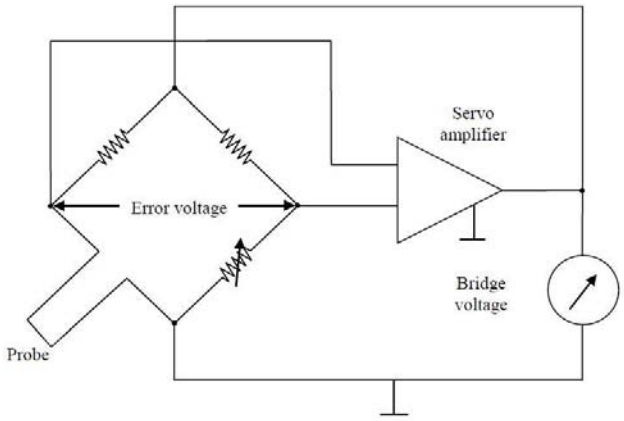

Figure 4.1: CTA bridge circuit

In this thesis, a hot-film probe is used. The hot-film is essentially a conducting film on a ceramic substrate. The hot-film is preferred to a hot-wire for the following reasons-

- The thermal conductivity of the substrate material is low. Hence very little heat losses due to conduction to the probe supports.
- More rigid and can be used in harsh conditions. The substrate protects the sensor against corrosion, damage and wear. Easier to clean.
- More flexibility in sensor configuration. Different shapes like wedge, conical, parabolic and flat surface are available.

However, hot-films also are expensive and do not respond to changes as quickly as hot-wires due to the fact that the films are slightly larger in diameter than the wires. This

means that at high frequencies the film sensor does not work as well as the wire. But since only lower frequencies are investigated with this technique, a hot-film is used as per availability.

HFA is used to obtain the velocity profiles at the exit of the jet for Reynolds number of 4300. Similar measurements were conducted with Thin Tomographic PIV and the velocity profiles are verified to demonstrate the comparability of the measurement data from the two techniques.

4.1.2 Pressure sensors

A pressure sensor measures pressure of typically gases or liquids. A pressure sensor usually acts as a transducer generating a signal as a function of the pressure imposed. Sensors are small, simple to mount and relatively easy to calibrate and measure. It has an advantage of being able to detect small fluctuations in both spatial and time constraints. This section gives a short account of the working principle of the sensors.

Microphones

A microphone is a sensor that converts sound or pressure fluctuations to electrical signals. These signals are later processed digitally to yield the required information. A microphone measures only fluctuating component of the pressure and not the mean. The microphone used for measurements here is the Sonion 8010T which has an omni-directional response. It has a frequency range of 100 Hz- 10 kHz and sensitivity of -33.5dB or 0.02 V/Pa at 1 kHz.

Sonion 8010T is a condenser microphone which senses pressure based on the change in the internal capacitance. The microphone is essentially a capacitor with one of the plates acting as a diaphragm. When struck by sound waves, this thin membrane vibrates causing a variation in the distance between the two plates. The variation in distance between the membrane and the back plate causes a change in the capacitance which alters the voltage through the resistance. An external voltage supply is required to get the capacitor working. In the case of the current microphone used, a supply voltage of $1\,V$ is given as per specifications. Figure 4.2 shows the working principle of a condenser microphone.

Assuming the charge of the capacitor Q remains nearly constant, the voltage V over the condenser is proportional to the distance between the plates given by the capacity law-

$$V = Q/C \tag{4.1}$$

where C, the capacity of the microphone is proportional to the area of the plates (A) and inverse of the distance between the plates (d), given by $\epsilon A/d$ with ϵ being the dielectric constant.

This voltage is converted to pressure by calibrating the microphone and obtaining a constant for the linear relation. The opposite side of the diaphragm also reacts to pressure disturbances with a delay while being insensitive to fast vibrations. Therefore, the pressure difference between opposite sides of the diaphragm p' is equivalent to the fluctuating component of the static pressure.

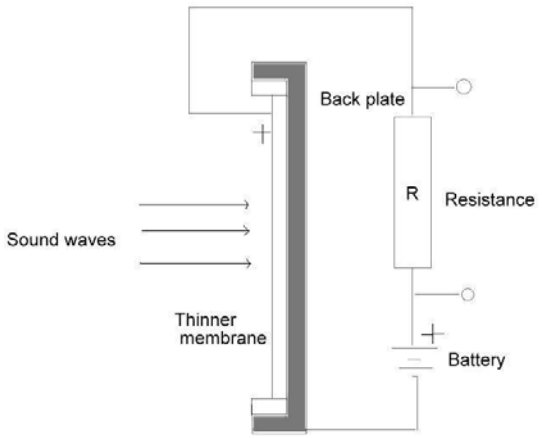

Figure 4.2: Working principle of a condenser microphone

For the far-field measurements, a condenser microphone: LinearX M51 is used which works on the same principle. A detailed description is presented in section 4.5.

Pressure transducers

A pressure transducer is a type of a sensor which generates a signal as a function of pressure imposed. It converts the air pressure fluctuations enforced upon it to electrical signals similar to a microphone. The electrical signals are then digitized to get valuable information relating to the physical phenomenon. Various pressure sensing technologies are currently available in the market which work on the principle of either strain gauges, i.e they use a force collector to measure strain or deflection caused due to applied force over an area or on the principle based on the properties of the fluid measured like density, temperature etc..

Pressure transducers can be classified in terms of pressure ranges they measure, temperature ranges of operation, and the type of pressure they measure. Transducers that measure pressure relative to vacuum are called *Absolute pressure sensors* while the ones that measure relative to the atmospheric pressure are known as *Gauge pressure sensors*. Several transducers can measure pressures below the atmospheric pressures like the *Vacuum pressure sensors* and difference in two pressures, such as the *Differential pressure sensors*. The current thesis uses a Gauge pressure sensor working on the principle of a piezoresistive strain gauge for measuring the surface pressure fluctuations.

The strain gauge transducer is essentially made of a Wheatstone bridge circuit with a combination of four active gauges (full bridge), two gauges (half bridge), or, less commonly, a single gauge (quarter bridge). In the half and quarter circuits, the bridge is completed with precision resistors. The present experiments employs a full-bridge sensor which ensures maximum sensitivity and wideband frequency response. The complete Wheatstone bridge is excited with a stabilised DC supply. As stress is applied to the bonded strain

gauge, a resistive changes takes place and unbalances the Wheatstone bridge. This results in a signal output, related to the stress value. Figure 4.3 shows the strain gauge principle where E represents the input voltage to the bridge and O/P is the output value rendered to the acquisition system.

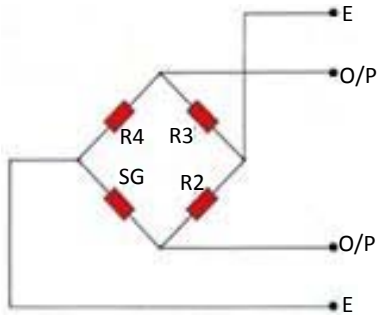

Figure 4.3: Working principle of a transducer

Strain-initiated resistance change is extremely small. Thus, for strain measurement a Wheatstone bridge is formed to convert the resistance change to a voltage change. Suppose in figure 4.3 R2, R3, R4 are resistances (Ω), Sg is the strain gauge and the bridge voltage (V) is E . Then, the output voltage e_0(V) is obtained with the following equation:

$$e_0 = \frac{SgR3 - R2R4}{(Sg + R2)(R3 + R4)}.E \tag{4.2}$$

If Sg changes by a resistance ΔR due to strain, then output voltage is given by-

$$e_0 = \frac{(Sg + \Delta R)R3 - R2R4}{(Sg + \Delta R + R2)(R3 + R4)}.E \tag{4.3}$$

If Sg=R2=R3=R4=R, then e_0 can be written as-

$$e_0 = \frac{R^2 + R\Delta R - R^2}{(2R + \Delta R)(2R)}.E \tag{4.4}$$

Here, the bridge resistance is considered to be much larger than the change in resistance. Therefore $R >> \Delta R$ gives,

$$e_0 = \frac{1}{4}.\frac{\Delta R}{R}.E = \frac{1}{4}.Ks.\varepsilon.E \tag{4.5}$$

where Ks is the gauge factor: the coefficient expressing the strain gauge sensitivity and ε is the tensile strain given by $\varepsilon = \Delta L/L$, the ratio of elongation to the original length.

Thus obtained is an output voltage that is proportional to a change in resistance, i.e. a change in strain. The output voltage being very small requires additional amplification for further analysis.

For a Reynolds number of 5000, a microphone from Sonion is used while for greater Reynolds numbers, an Endevco pressure transducer is chosen for measurements. The

reason for this choice is that for lower Reynolds numbers, the uncertainties are much higher than the measured fluctuations in the pressure transducer. The pressure transducer has a range of $0 - 6.897\ kPa$ with a cumulative uncertainty of 30 Pa. While for Reynolds numbers like 5000, the fluctuations measure close to 7 Pa at the peaks. To avoid unreliable measurements, a different sensor that corresponds to the required range is used. It is seen fit that a low pressure range microphone could be used for these measurements.

4.2 Jet facility

4.2.1 Semi-anechoic chamber

To reduce the disturbances in fluctuations during measurements and to obtain an acoustically insulated environment for the far field measurements, the set up is placed inside a previously built semi-anechoic chamber (refer de Boer (2011)). The chamber measures 2.32x1.86x1.86 m^3 in size and is lined by a porous acoustic foam of thickness 0.071 m which absorbs sound thereby reducing reflections. The opening for the nozzle is 0.5 m above the ground and 0.5 m away from the y-plane of the chamber. The chamber is equipped with a door on the opposite face with dimensions of 1.5x0.5 m^2. The set up is placed inside, on the floor of the chamber with an appropriate support system as described in section 4.2.3. Also, Appendix B, shows a representation of the chamber with dimensions.

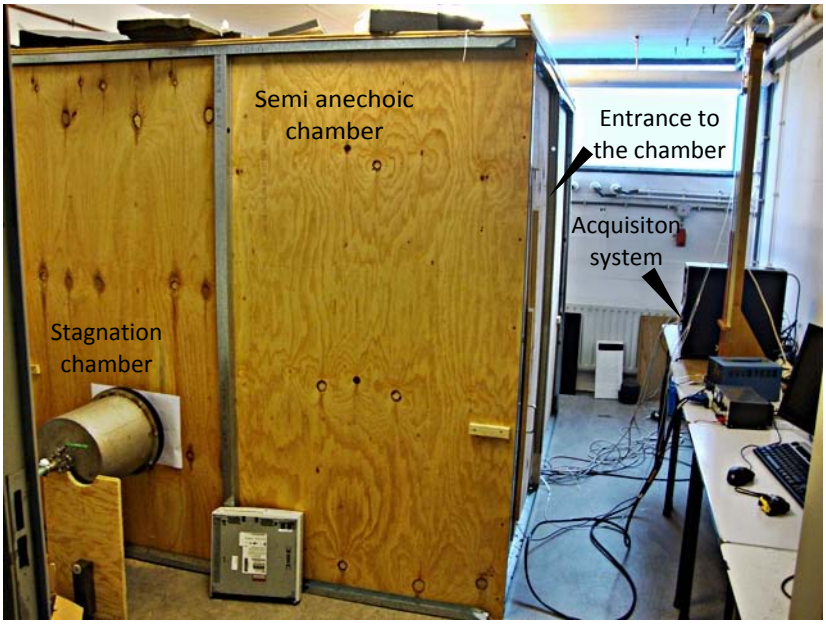

Figure 4.4: Experimental facility

4.2.2 Air supply system

The air is supplied to the system from a pressure vessel of size 300 m^3 compressed at a pressure of 40 bar. The dry air issued has a relative humidity ratio of $4.1 * 10^{-6}$ and is

channelled through a pipe that expands the air to 10 *bar*. Further, to be able to regulate the pressure in the jet at low subsonic range, a high precision pressure regulator and a needle valve are used which effectively reduce the supply pressure to 2 *bar*.

Figure 4.5: Nozzle

From here on, two configurations for a jet system are used. Initial experiments were conducted with the first configuration which consisted of a 1.5 m long PVC tube having an internal diameter of 0.119 m. The expanded air enters the pipe via a bronze diffuser which permits a relatively noiseless transition of flow by artificially enhancing the mixture of high speed compressed air from the pressure vessel and low speed air inside the tube. The tube is lined with acoustic foam layer of 0.02 m thickness to reduce the noise generated by the flow. The center of the tube holds a permeable piece of sound absorbing foam. Near the exit, a honeycomb structure is placed to prevent swirling of fluid along with 3 subsequent meshes to facilitate a fully laminar exit through the convergent nozzle of diameter 0.010 m.

Figure 4.6 shows the components of this configuration of the jet. The flow through this jet configuration, when measured at a low Reynolds number and compared with existing results, showed spurious frequencies leading to the conclusion that the flow was not sufficiently laminar which necessitated the use of a better configuration as explained below.

(a) Bronze air diffuser (b) Honeycomb mesh (c) Foam structure

Figure 4.6: Parts of the first configuration of the jet

The second configuration which proved to be more effective consisted of 0.3 m long cylindrical container with a radius of 0.3 m and height 0.8 m that is connected to the air

(a) Cylindrical stagnation chamber

(b) Nozzle inside the chamber

(c) Internal foam structure in the cylinder

Figure 4.7: Parts of the second configuration of the jet

supply via the diffuser. This container acts as a second stagnation chamber at the end of which a honeycomb structure of 0.07 m thickness is placed to ensure an enhanced laminar flow. The cylinder is connected to a smaller tube with a contraction ratio of 56.25. The air at the end of this tube passes through a second honeycomb mesh of thickness 0.05 m which is placed to ensure continued laminar flow at the outlet. The nozzle is connected to this end which provides a second contraction. The combination of two contractions and thicker honeycombs lead to a structured flow that facilitates better jet characterization.

4.2.3 Jet impingement configuration

Following the approach used by Ho and Nosseir (1981), Hall and Ewing (2005), Hall and Ewing (2006) the development of the large scale structures in the jet is examined by quantifying the fluctuating surface pressure upon impingement. The set up for measuring these fluctuations is built inside the semi-anechoic chamber to limit the disturbances in the fluctuations caused due to external agents. The nozzle of the jet opens into the chamber at a distance of 0.2 m, sufficiently far away from the walls of the chamber to avoid structural interference with the flow. A pitot probe is mounted on a rigid traverse system perpendicular to the flow direction to be able to measure the axial velocity of the flow at the nozzle exit. A flat aluminium plate measuring 0.6x0.5x0.005 m^3 is used to provide a large surface for the impinging jet.

It is mounted on a traverse mechanism (figure 4.8) with 3 degrees of freedom that is used to adjust the position of the plate relative to the jet axis. The center of the plate is embedded with the sensor to detect the surface pressure fluctuations caused by the jet.

The first step for setting up the experiment is to align the sensor with the axis of the jet. This is done by measuring the distance of the nozzle axis from the ground and accordingly build the set up with the traverse system such that the sensor position is marked at the same dimensions from the walls of the chamber as the nozzle axis; as explained in detail in section 4.3.2.

To ensure proper alignment, a simple and quick oil flow visualization technique is employed for verification. The aluminium plate is covered with a black adhesive paper and placed at a height from the nozzle of $H = 4diameters$ from the nozzle's center. Lubricant oil is sprayed on the paper and the jet is turned on. Saw-dust is blown from right angles to

Figure 4.8: 3-axis traverse system

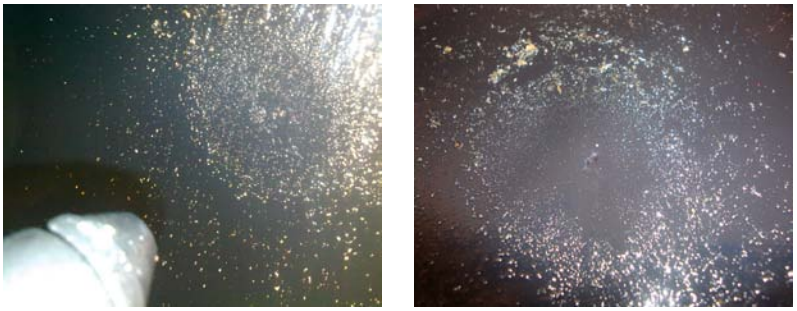

(a) Oil flow visualization (b) Visible axis of the jet

Figure 4.9: Oil flow visualization

the flow on the plate for better visualization of the oil flow on the plate. The flow creates a pattern by spreading the oil in radial direction clearly indicating the center of the jet. This center point is marked while the jet is stopped. The co-ordinate position of the point is measured, the adhesive paper is removed and the sensor is flush mounted on the plate at the measured location. A picture of the oil flow visualization is shown in figure 4.9.

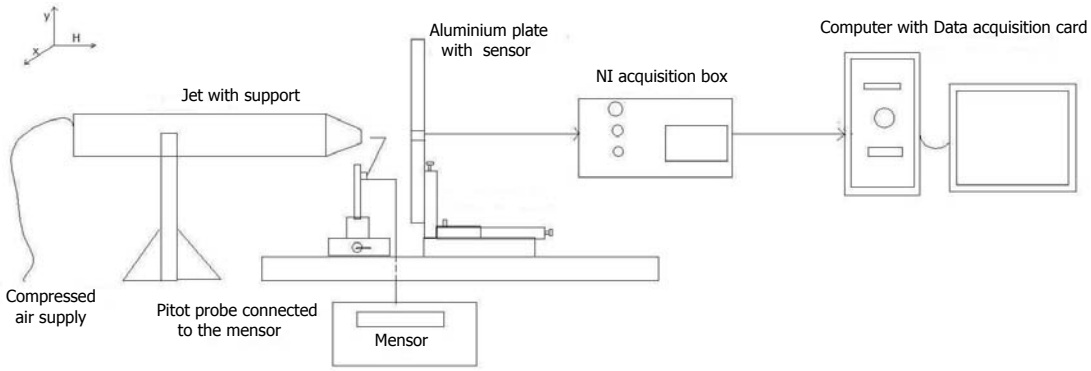

Figure 4.10: Representation of the jet impingement set-up

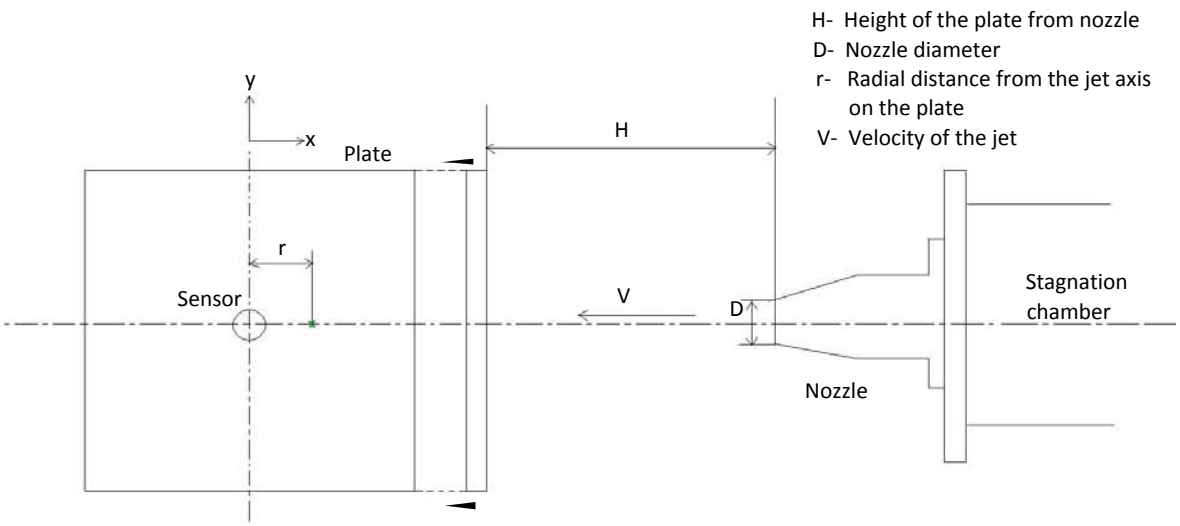

Figure 4.11: Experimental parameters

The sensor output is connected to the acquisition system placed outside the chamber which is in turn connected to the computer with the LabVIEW program to acquire these signals. The block diagram 4.10 shows the circuit of the jet impingement set up and figure 4.11 designates the important experimental parameters used in this thesis.

4.2.4 Acquisition System

The acquisition system here consists of an 8-channel National Instruments signal conditioner: NI-1301, that connects the sensors to the acquisition card: NI-PCI-6250 in the computer. The experiment is moderated using a suitable acquisition program on LabVIEW. For the pressure transducer, an input signal range of $\pm 0.1\ V$ is set while for the microphone a range of $0 - 1\ V$ is specified. A low-pass frequency is specified based on the flow regime not exceeding half the acquisition rate. The excitation voltage for the sensors is set according to the specifications given by the companies: $10\ V$ for the pressure transducer and $1\ V$ for the microphone. The signals are acquired at a sampling rate of $10000\ Hz$, for a period that is determined by checking for convergence of the RMS pressure fluctuations on the plate. For Reynolds numbers below 50000, the signal is acquired for $60\ s$ each while for $Re = 50000$, $30\ s$ is seen as sufficient. The sampled signals are converted to pressure using the linear sensitivity coefficients of the sensors.

4.3 HFA set-up and measurements

Hot-Film Anemometry is used to establish the comparability of the experiments conducted with pressure sensors in an air jet and Tomographic PIV in a water jet. Similarity of the exit conditions is essential to be able to employ the two methods to describe the topology of the jet and also for future work as mentioned in section 1.3. Hence velocity fluctuations at the jet exit is measured using a hot-film and the mean velocity profile is

plotted across the radial span of the nozzle. Velocity profile obtained from Thin Tomo PIV is used to compare with the hot-film measurements to affirm the similarity between the two systems.

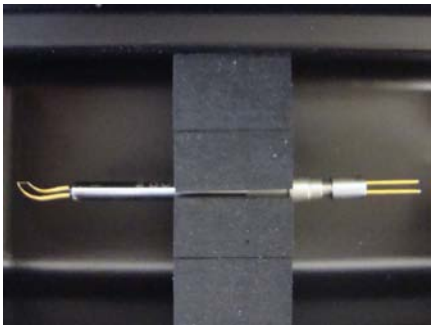

Figure 4.12: TSI Hot film sensor

A Thermal Anemometry System(TSI)'s hot film sensor where the film is held vertically by the probe ends is used for measurements with appropriate mounting. The vertical placement of the wire serves the purpose of mapping the shear layer velocity profile.

The hot film is fixed to a probe whose wire is connected to the TSI's Constant Temperature Anemometer(CTA) instrumentation box. The IFA-300 CTA is in turn connected to the NI-acquisition card: NI-PCI-6250 whose output bridge voltage and temperature are transferred to the computer. The CTA is also connected to the computer through Port-A. A thermostat is placed in the measurement room(semi-anechoic chamber), that is plugged to the CTA system. A supply voltage of $220\,V$ is provided to the CTA. A block diagram (figure 4.13) shows the set-up of the hot-film measurements.

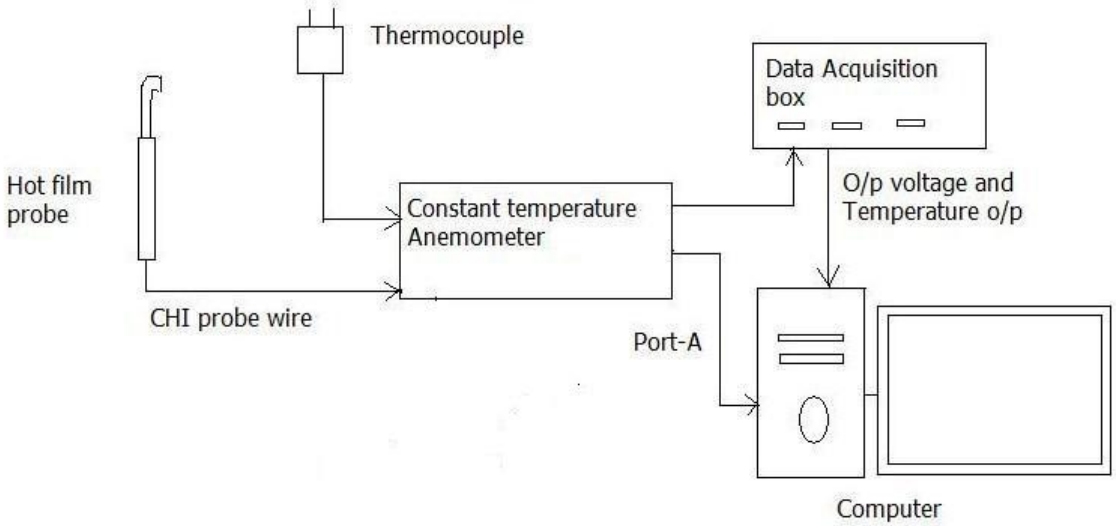

Figure 4.13: Representation of the hot-film circuit

Table 4.1: Hot-film specifications

Probe resistance	9.49Ω
Wire resistance	0.18Ω
Operating resistance	$\pm 7.2\Omega$
Diameter of the film	$50.8\mu m$
Length of the probe	$1.02mm$
Distance between supports	$1.65mm$
Max. sensor operating temperature	425 °C
Material of film	Platinum coated

4.3.1 Calibration

The system has to be calibrated before carrying out measurements to obtain the voltage-velocity relation. The output of the hot-wire anemometer is analogue and it represents the velocity in a specific point of the flow. The response of the hot-film is non-linear and is given by-

$$E^2 = A + BU^n \tag{4.6}$$

where A,B,n are constants depending on system properties and are determined by a calibration procedure, E is the measured voltage and U is the measured velocity. Considering that the King's law expresses the relation for n = 0.45 (for air, between 0 and 20 °C), the relation between U and E requires at least a fourth order polynomial to be represented accurately. Therefore the fitting function reads as:

$$U = C_0 + C_1E + C_2E^2 + C_3E^3 + C_4E^4 \tag{4.7}$$

The HFA settings are controlled by *ThermalPro* software, where gain, offset, resistances of the film, probe and filters are set. The relative accuracy of the system varies between 95% at $0.1m/s$ to 99.7% at 5 m/s. [Nati (2011)]. The resistance of the probe and cables is determined by 'short-cutting' around the probe. The specifications of the hot-film are given in the table 4.1. The operating temperature of the system is set to 250 °C.

The voltage range is $\pm 5\,V$ and needs to be fully covered to increase maximum HFA accuracy. The system has a 12-bit A/D converter card with $10/12^2 = 2.44mV$ voltage steps(Nati (2011)).

The air supply system and nozzle used for the pressure sensor measurements as explained in section 4.2.3 are employed for the hot-film measurements. Since examining the exit properties of the free jet is the priority, the plate is dismounted from the traverse system. However, the traverse is used to mount the hot-film probe and to align it. The probe is fixed on to a 3-axis stand that is mounted on the traverse system. It is first aligned to measure free shear layer near the jet exit. The film is aligned to the nozzle edge, perpendicular to the horizontal axis of the nozzle.

The exit velocity profile is evaluated at a nozzle-to-plate distance of $H/D \approx 0.1$: nearly the nozzle exit and in a laminar flow regime of $Re = 4300$. The connections of the circuit

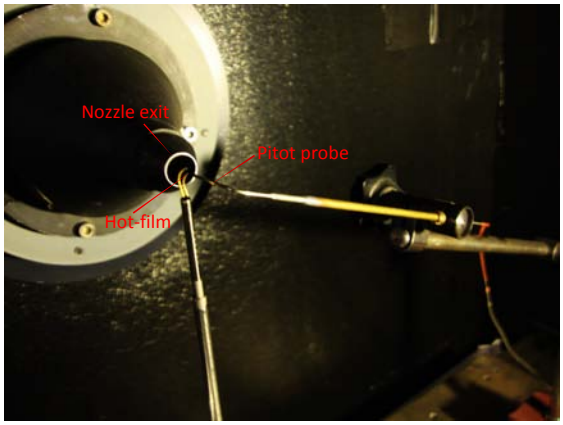

Figure 4.14: Hot-film calibration

are checked and the probe is shorted for calibration. The initial gain and offset of the film is set to zero. Using the software *Thermal Pro*, the resistance of the probe wire is determined. With these input parameters, the cable resistance is calculated by the tool. These values in *Thermal Pro* are transferred to a LabVIEW program automatically which is then is used for obtaining the calibration constants. The shorted probe is now reconnected to the film. To obtain the gain and offset, signal acquisitions at the maximum and minimum limiting pressures are obtained and the program is allowed to calculate the gain and offset. These values replace the original offset and gain values on *Thermal Pro*. For adjusting different pressures, a pitot probe set up as applied for the pressure sensor measurements (4.4.3) is used alongside the hot-film without causing mutual interference as shown in figure 4.14. In this case, the sensor was calibrated between 2 and $450 Pa$.

Now, 10 data-points at increasing velocities are acquired within the range of set pressure values. The program reflexively plots the calibration curve after the desired number of calibration points and interpolates the coefficients which are directly channelled to LabVIEW for measuring velocities.

4.3.2 Procedure adopted for measurements

After the calibration, the pitot probe is moved away from the nozzle exit and the film is positioned at the edge of the nozzle along its horizontal axis. Beginning from the edge of the nozzle and moving towards the center(figure 4.15), the signal of the jet is acquired for $20s$ each. The traverse system is used to move the hot-film in specific increments. Care is taken to see that the film is handled sensitively as it is prone to damage quickly. Voltage signals are acquired according to the intervals presented in table 4.2.

Table 4.2: Measurement intervals

$0.36 > r/D < 0.5$	$\Delta r/D = 0.05$
$0.29 > r/D < 0.35$	$\Delta r/D = 0.1$
$0 > r/D < 0.2$	$\Delta r/D = 0.28$

The acquisitions made at a sampling frequency of $10000 Hz$ are introduced into MATLAB to check for the mean and RMS convergence of the fluctuating velocity. The velocities

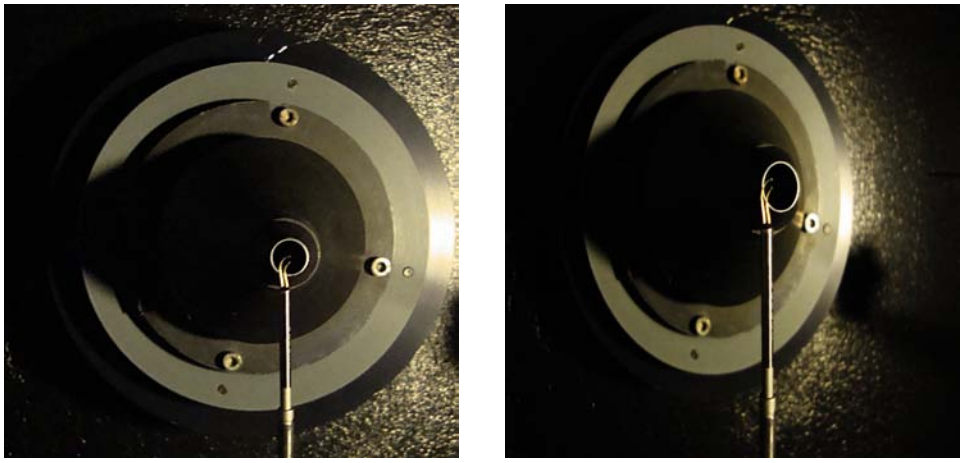

(a) Hot-film at the center of the jet

(b) Hot-film traversing towards the edges

Figure 4.15: Hot-film measurement

are then used to create the mean and RMS profile of the flow near the nozzle exit. The same procedure is adopted for a nozzle-to-plate distance of $H/D = 1$ but with a constant interval of $r/D = 0.1$ between two measurements.

The mean axial velocity profile and comparison are presented in chapter 6.

4.4 Surface pressure measurements

Locations close to the sound source between the source and the far-field can be categorized as near-field. Here, the variation of sound pressure with distance is a complex function of the radiation characteristics of the source. The near-field is typically characterized by large sound pressure level variations with small changes in measurement position from the source. To measure these fluctuations, pressure sensors like transducers and microphones prove to be capable instruments. This section describes the apparatus, set-up and the procedure for measurements done in the near-field of jet impingement using a microphone and pressure transducer.

4.4.1 Microphone calibration

Sensors have to be calibrated before conducting measurements to ensure that the effects of temperature, density and other mechanical or electrical factors are taken into consideration. The calibration is done using a pistonphone. A pistonphone is a device which acts as a sound source that uses closed coupling volume to generate a precise sound pressure for calibration purposes. It has a piston that is mechanically driven to move at a particular frequency, resulting in oscillation of air to which the pressure sensor is exposed. The sensor detects the fluctuations in air pressure in the form of voltage variations which is used to calculate the sensitivity of the microphone. Sensitivity is defined here as the

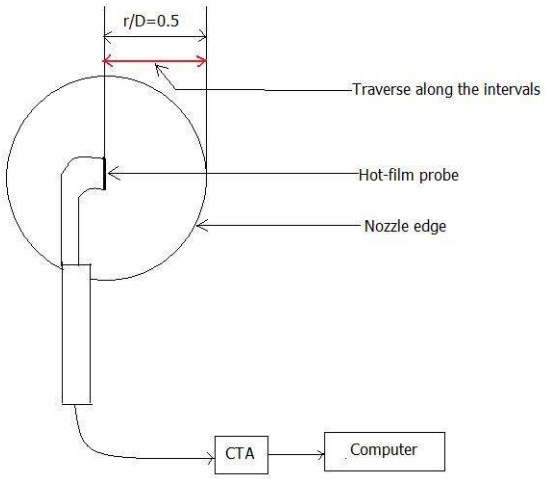

Figure 4.16: Representation of measurement traverse

change in voltage of the sensor for a pressure variation of $1Pa$. The calibration constant thus obtained is further used to calculate the pressure fluctuations of the jet.

The Sonion microphones are calibrated using a pistonphone that produces a frequency of $250Hz$ at a Sound Pressure Level of $114.0dB$ ($105.4dBA$). The principle used for calibration is based on comparison of the pistonphone signal recorded by the microphone with that from a known sensor. Since the sensitivity of the pressure transducer is already known, it serves as a good choice for comparison.

Figure 4.17: Endevco 8507-C pressure transducer and Sonion 8010T microphone

The pistonphone, a G.R.A.S Pistonphone type 42AA, is first aligned axially with the pressure transducer which is connected to the acquisition system and its voltage variations, V_{pt}, are recorded. The transducer has a linear response as discussed in the following section. The corresponding standard deviation of the pressure fluctuations P_{pt} are calculated using the transducer sensitivity. The pistonphone is then aligned with the microphone to obtain the standard deviation of the voltage variations, V_{mic}. Theoretically, this voltage fluctuation corresponds to P_{pt} since the source is exactly the same. Or in other words,

the change in air pressure due to a particular source induces a similar voltage fluctuation in different sensors.

Figure 4.18: Hand-held pistonphone

Therefore, for every 1 Pa change in the air pressure, the voltage fluctuation of the microphone can be calculated as-

$$\frac{V_{mic}}{P_{pt}} = Sensitivity \tag{4.8}$$

The pistonphone recorded a standard deviation (σ) of 9.5174 Pa on the pressure transducer and a voltage deviation of 0.1986 V which translates to-

$$\frac{0.1986 \;\; V}{9.5174 \;\; Pa} = 0.02154 \;\; V/Pa \tag{4.9}$$

The sensitivity of the microphone thus obtained is verified from the specification of -33.5 dB at 1 kHz by Sonion. A difference of 1.8% was found in the sensitivities which can be attributed to the prevalent ambient conditions in the laboratory and calibration procedure.

4.4.2 Pressure transducer calibration

An Endevco 8507-C1 pressure transducer was used for the measurements which has a piezoresistive strain gauge. It uses the piezoresistive effect of bonded or formed strain gauges to detect strain due to applied pressure. The strain gauge is connected to form a Wheatstone bridge circuit to maximize the output of the sensor. A specified excitation voltage of $10\,V$ is supplied across the bridge. The maximum and minimum input voltages to the DAQ system is set as $\pm 100 mV$. The range of the current transducer used is $6897 Pa$.

Calibration

The pressure transducer is calibrated using a closed system with a U-tube water manometer against Mensor DPG 2001 which has a range of $3447 Pa$ and an uncertainty of 0.010 % FSO. The transducer is connected to the acquisition system and the manometer as

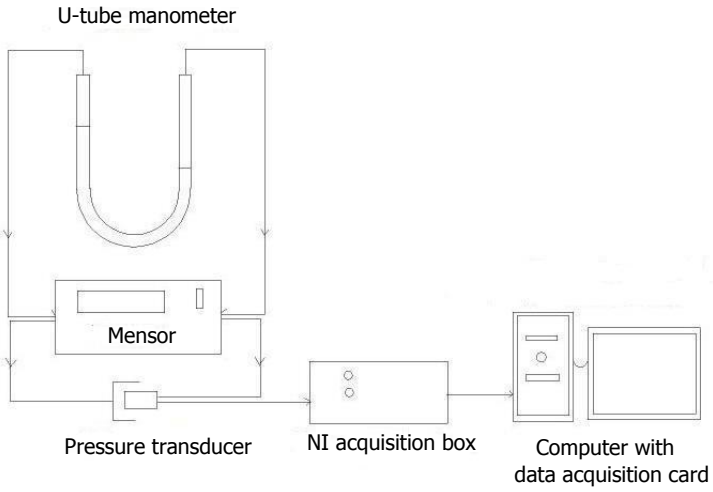

Figure 4.19: Block diagram of the pressure transducer calibration

shown in the figure 4.19. The manometer is in turn connected to the mensor. A pressure difference is created in the manometer by using the water column height as the reference which translates as a pull force on the back plate of the transducer. The corresponding mensor reading is noted down. A stopper is applied to the manometer to maintain the pressure while the transducer signal is recorded through the acquisition system. A block diagram of the system is given in figure 4.19.

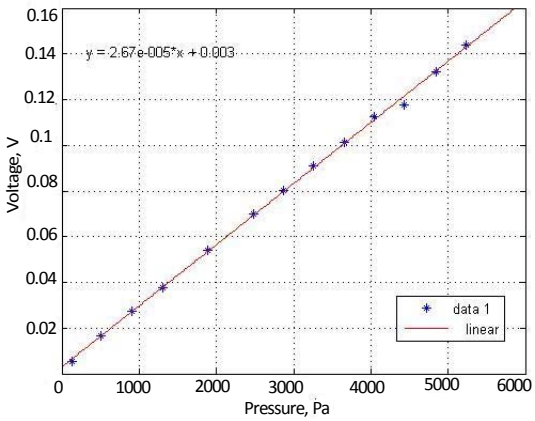

Figure 4.20: Calibration curve and sensitivity of the pressure transducer

The procedure is repeated for a range of pressure differences in the manometer. Assuming Δh is the reference height of the water column in m, ρ is the density of water (1000 kg/m^3) and g is the gravitational constant (9.8 m/s^2), the pressure difference in the manometer (ΔP) is calculated as-

$$\Delta P = \rho g \Delta h \tag{4.10}$$

Plotting the pressure difference for each trial against the voltage acquired for each trial, a

linear curve is obtained as shown in the figure from which the sensitivity of the transducer is calculated as the slope of the curve. The sensitivity is obtained as 26.7 mV/kPa as shown in figure 4.20.

4.4.3 Procedure adopted for measurements

The plate with the sensor, mounted on the 3-axis traverse system is placed at a distance of 4 diameters from the nozzle exit. The traverse system and the nozzle are fixed to the chamber floor and wall respectively. Before beginning the measurements, the sensor alignment with the jet axis is checked.

Alignment : As explained in section 4.2.3, the plate is initially aligned by measuring the dimensions of the nozzle axis and the walls of the semi-anechoic chamber. The sensor is fixed such that it is in line with the jet axis. However, to check if there are any discrepancies in the alignment caused while mounting the sensor or the plate, or due to uneven traverse planes, the alliance between the center of the nozzle and the sensor is cross-checked manually along perpendicular axial planes. The plate with the sensor is traversed forward to a distance of $H/D \approx 0.1$ from the nozzle exit. With the help of appropriate lighting, the sensor position is fine tuned to lie along the center of the nozzle by viewing it from horizontal and vertical planes as shown in figure 4.21.

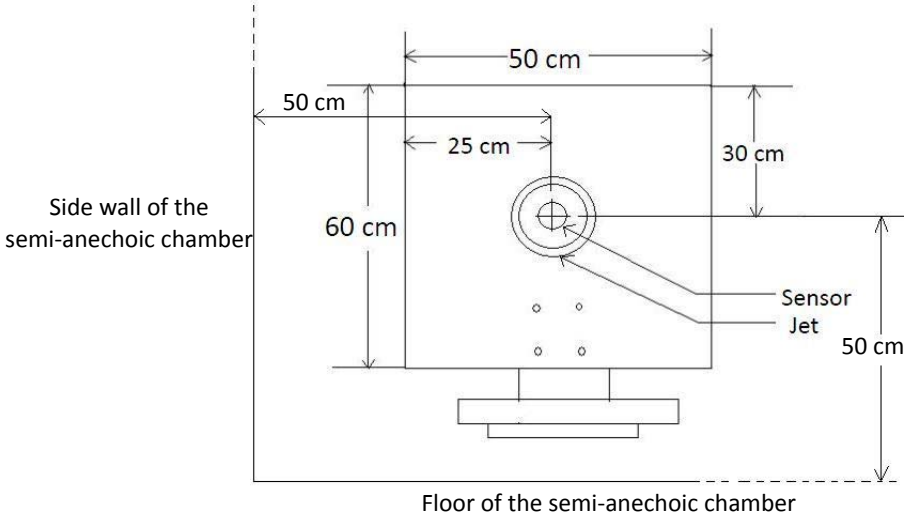

Figure 4.21: Front view of the impinging plate to show the alignment views

For further verification, the plate is traversed back and forth once again to check for any misalignment. Once the alignment is confirmed, the plate is moved back to a distance of 4 diameters where the initial measurements are done to check for axial symmetry of the jet and to obtain the pressure fluctuation profiles at various Reynolds numbers. According to Yule (1978), transition of the jet from laminar to turbulent flow is initiated at around $H/D = 3 - 4$ for low Reynolds numbers of the order of 10^3 and earlier as the Reynolds number is increased to an order of $5 * 10^4$. This is confirmed more recently by Violato and Scarano (2011) where it was observed that the axial symmetry of a paired vortex

begins to decay at nearly 4 diameters from the nozzle. The regimes investigated here are within the above mentioned Reynolds number range and the flow exit conditions are the same as that used for the most recent PIV measurements by Violato et al. so as to draw interpretations using both the techniques. Also to aid future work regarding comparison of pressure reconstructed from Tomo-PIV and sensor measurements, the nozzle-to-plate distance used in the first part of this thesis is same as that of PIV measurements. Hence, a nozzle-to-plate distance of $4D$ is chosen such that the structures are still intact when impinging and pressure variations captured by the sensors do not consist of turbulent fluctuations.

Determining the exit velocity : The exit velocity of jet is the most important factor for further measurements and analysis. It can be determined from the dynamic pressure of the jet at the nozzle exit. A custom-made pitot probe, which measures the stagnation pressure due to adiabatic compression, is mounted on a stand which has three degrees of freedom. The stand is mounted on a sliding mechanism orthogonal to the nozzle exit as shown in figure 4.22. The pitot probe reads the total pressure of the system.

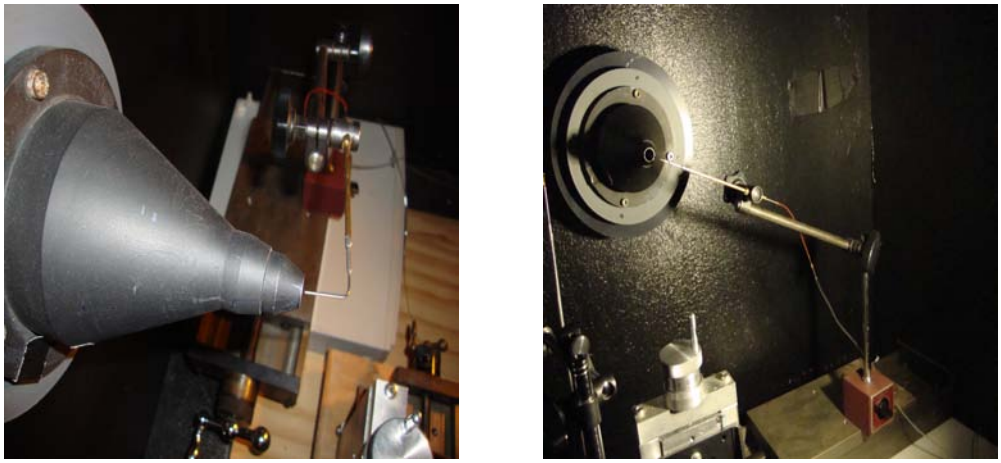

(a) Pitot probe at the exit (b) Probe mounted on the stand

Figure 4.22: Pitot probe set up

The probe is connected to the Mensor outside the chamber. The gauge pressure reader is then corrected for any shown offset. This means that the atmospheric pressure is set as zero reference. The air supply from the main tank is switched on and a pressure regulator is used to control the air entering into the pipe or the secondary stagnation chamber. The reading on the Mensor is noted for different exit pressures along with the stagnation pressure readings. Velocity for each pressure reading is calculated from Bernoulli's principle-

$$P_{tot} = P_{atm} + q \tag{4.11}$$

where P_{tot} is the total pressure, P_{atm} is the atmospheric pressure inside the chamber and $q(= \frac{1}{2}\ \rho\ V^2)$ is the dynamic pressure. So, the above equation becomes-

Table 4.3: Flow regimes investigated

Desired Re	q,Pa	V,m/s	Achievable Re	Flow regime
5000	34	7.5503	5033	Nearly Laminar
10000	135	15.0450	10030	Transitional
20000	537	30.0064	20004	Turbulent
50000	3355	75.0020	50001	Highly turbulent

$$\Delta P = P_{tot} - P_{atm} = q = \frac{1}{2}\rho V^2 \tag{4.12}$$

where density ρ, is calculated using the gas law, defining $R = 287.058 J/kg\ K$ as the universal gas constant and T as the air temperature which is considered to be same as the ambient temperature. P_{amb} is the ambient pressure which is read from a barometer as $1.01011 * 10^5 Pa$.

$$\rho = P_{amb}/RT \tag{4.13}$$

Therefore, the velocity is given by,

$$V = \sqrt{2q/\rho} \tag{4.14}$$

Knowing the nozzle geometry and jet properties, the Reynolds number for this flow can be obtained as-

$$Re = VD/\nu \tag{4.15}$$

where Re is the Reynolds number, V is the velocity obtained from Bernoulli's equation, D is the characteristic length of the flow which, in this case is the diameter of the nozzle and ν is the kinematic viscosity which is temperature dependent. A constant of $20\,^{\circ}C$ was measured for all the experiments conducted.

The table 4.3 shows the range of Reynolds numbers that were investigated along with their dynamic pressures and velocities at nozzle exit. The range of Reynolds numbers chosen is based on the idea of investigating flows in laminar, transitional, turbulent, highly turbulent flow.

The slight differences in the desired and achievable Reynolds numbers is due to the fact that the pressure reader can read only discrete values and hence fine tuning it to achieve the required pressures for required Reynolds number is difficult. However, since the differences are within 5% of the required values, the flow is considered to belong to the same regimes.

Calibration is done as explained in section 4.2.3 for the sensor chosen and the gain is noted down. The pitot probe is placed at the nozzle exit along the axis and the jet is discharged. The pressure at the exit of the jet is controlled by an additional needle valve at the upstream to obtain a nearly accurate Reynolds number. Once the desired velocity

is achieved, the pitot probe is moved away without disturbing the set-up and the jet is allowed to stabilise.

The first set of experiments done at a nozzle-to-plate distance of 4 diameters with the above described set up aims at finding the pressure fluctuation profiles of the jet along the horizontal(x) and vertical(y) axis of the jet starting with the sensor at the origin i.e. the centreline of the jet. The objective is to establish the axis symmetry of the jet at different flow regimes and to obtain the regions of maximum pressure fluctuations in the radial direction that gives an idea about the distribution of the flow structure upon impingement which plays an important role in the study of noise emissions, local heat or mass transfer rates etc..

Starting from the stagnation point, a scan of both positive and negative x and y axes is done for each of the Reynolds number by traversing the plate embedded with the sensor at specific intervals. Since the difference in pressure fluctuations varies consistently, measurements are made at smaller intervals of $r/D = 0.2$ from $r/D = 0 - 2$ to obtain a precise image of pressure variations on the wall. Beyond $r/D = 2$, as explained in the previous chapter, the flow turns turbulent and the pressure fluctuations constantly decrease. Although this is verified, the focus is emphasised in the regions of stagnation upto fully developed turbulent flow.

Once the jet is released and the connections of the sensor, the data acquisition system and the computer are ascertained, a time signal is collected using an acquisition program on LabVIEW at a sampling frequency of $10000Hz$. The plate is traversed manually after each acquisition in all the four directions with the above mentioned intervals. When a signal is acquired, it is converted into Pressure(Pa) using the calibration constant and is checked for the mean and Root Mean Square(RMS) convergence of the pressure to make sure that the fluctuations perceived by the sensor are indeed stabilised and are not influenced by surrounding factors of pressure variations. For measurements at lower Reynolds numbers, it is known through studies that the large scale structures are convected in the jet at lower velocities. By adopting a smaller time length for acquisition, the fluctuations on the wall may not be stabilized and energy data in the spectrum will be lost. To be able to discern the correct distribution of energy, more number of samples needs to be incurred. Hence at lower Reynolds numbers the signal is acquired for about 60 s which shows an acceptable convergence within $\pm 5\%$. As the flow regime advances, the length of the time signal is shortened as enough samples are obtained within a shorter time frame. The fluctuating pressure signal is then used to obtain a power spectrum from which the intrinsic frequencies of the system can be determined. The standard deviation of the pressure calculated in each case is used for further analysis that is presented in the next chapter.

4.5 Far-field set-up and measurements

The free-field consists of two parts, the near-field and the far-field. In the far-field, the sound pressure is inversely proportional to the distance and has interference effects. Acoustic measurements are conducted such that the microphones are in the far-field of the impingement area. Generally, the far-field condition begins at a distance greater than

Specifications	
Element Type	Electret Condenser
Preamp / Line Driver	SMT Active Preamp
Uncorrected Freq Response	±5dB 10Hz-40kHz
Corrected Freq Response	±1dB 10Hz-40kHz
Acoustic Sensitivity	-36dBm/Pa (12mV/94dBspl)
Output Impedance	150 Ohms
Maximum SPL	150 dBspl
1/3 Octave Noise @1kHz	18 dBspl
ANSI-A Weighted Noise	34 dBspl
Temperature Range	0C° to +40C°
Temp Coef @1kHz	-0.01dB/C°
DC Supply Voltage	9 VDC ±10%
DC Supply Current	30mA Typ
Electrical Connector	Switchcraft TB3M / cable to A3M / LVP Interface
Construction and Finish	Aluminum, Black Anodized
Microphone Dimensions	Diameter: 0.52", Length: 4.25"
Weight of Mic and Cable	1 oz (28 grams)
XLR Adapter Cable Length	6 Feet (2 meters)

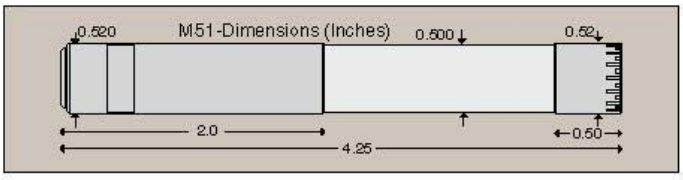

Figure 4.23: LinearX M51 microphone specifications

the wavelength of the lowest frequency emitted from the source, or at more than several times the greatest dimensions of the source.

Following the near-field pressure measurements, far-field noise measurements are done to investigate sound propagation due to fluid-structure interaction. The measurement essentially consists of the same set-up as that used for near-field measurements with the difference being the use of an acoustic microphone for measurements. The sensor used here is a LinearX M51 microphone. The specifications of the microphone is presented in figure 4.23.

The M51 is a high performance low voltage electret condenser microphone. It is a low cost, low distortion microphone with low power supply requirements, a high threshold for sound pressure levels and wide frequency range. It incorporates a special element/preamp design which enables performance and capabilities far superior to that of typical electret type microphones, and allows for operation from a single $9\,V$ DC supply. The data recorded by the microphone is transferred to the PCI-6250 through the BNC-2110 A/D converter at full-scale setting. The circuit connection is shown in figure 4.24.

For an acoustic wavelength of λ_a and distance d between the source and observer, the observer is said to be located in the far-field if $\frac{\lambda_a}{2\pi d} << 1$, where pressure and velocity fluctuations are in phase. This condition follows Arndt et al. (1997) who gives a relationship between wavenumber and measurement distance for the boundary between the near and far field of a round jet as $kd >> 1$ where $k = 2\pi/\lambda_a$. From the near-field measurement results as presented in 6.2.4, it is known that for a Strouhal number of 0.38, the corresponding frequency is 2850 Hz with respect to the exit velocity and nozzle diameter.

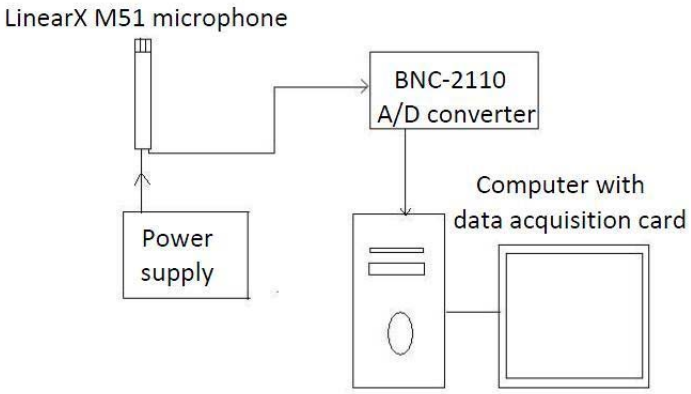

Figure 4.24: Microphone circuit block-diagram

Then, the acoustic wavelength is calculated as the reciprocal of the frequency with respect to the speed of sound. Hence $c_0/f = 0.1193$ where $c_0 = 340m/s$. Testing the far-field condition for distance of $0.3m$, $\frac{\lambda_a}{2\pi d} = 0.063 << 1$. At distances lesser than $0.3\ m$ the ratio tends towards 1. Since the condition requires the ratio to be much smaller than 1, the far-field is considered to start at $0.3m$. Measurements are conducted at two distances of $d = 0.3m,\ 0.5m$ for the sake of comparison. The microphone is placed at two angles of $\theta = 60\,^\circ,\ 90\,^\circ$ to the jet axis as shown in the figure 4.25.

The aim of a complete directivity test for angles below $60\,^\circ$ could not be conducted due to spatial constraints in the semi-anechoic chamber. These measurements can be conducted by increasing the distance between the nozzle exit and the back wall of the measurement chamber (refer fig.4.25).

The pistonphone described in section 4.1.2 is used to calibrate the microphone. Following the procedure applied for calibrating the Sonion microphone, the coupler of the pistonphone is placed as input to the microphone and the voltage signal is acquired. The corresponding pressure fluctuation of the pistonphone is known as $10Pa$. Adopting equation 4.8, the calibration constant for the microphone used is obtained as-

$$\frac{0.1227\,V}{10Pa} = 12.3mV/Pa \tag{4.16}$$

This value is in close agreement to the company specified sensitivity of $12mV/Pa$. A sampling frequency of $20{,}000Hz$ is used to acquire the signals from the microphone. Analysis and results of the far-field measurements are presented in chapter 6.

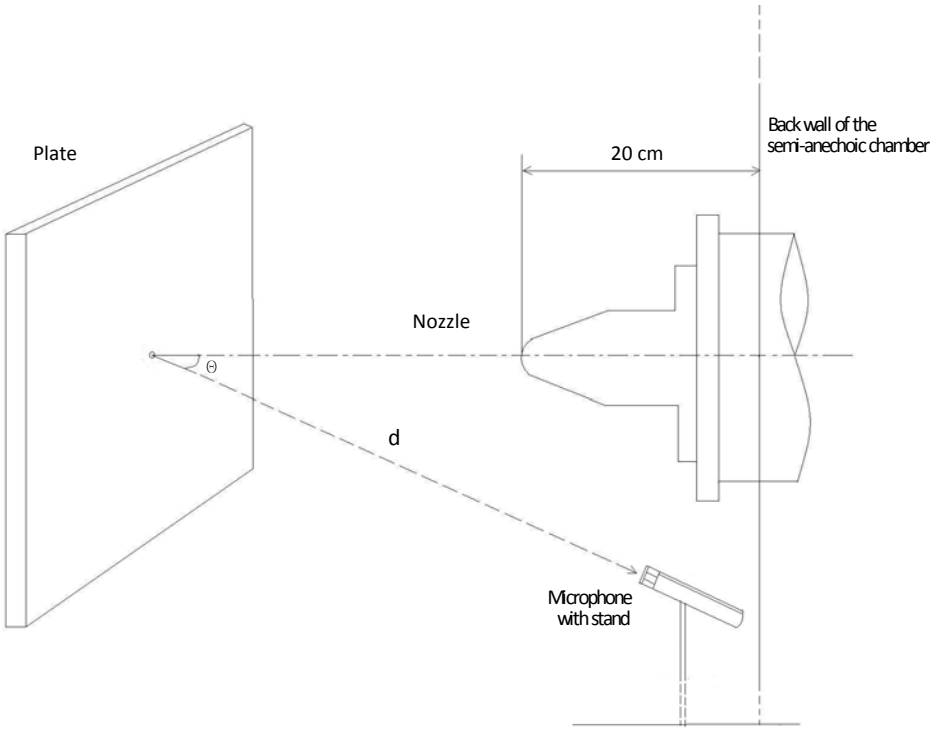

Figure 4.25: Representation of the far-field parameters

Chapter 5

Data Analysis

While the previous chapter explained the experimental set up and acquisition of jet signals, the current chapter focusses on the post-processing of data acquired in order to obtain the pressure fluctuations due to impingement and spectral composition of various flow regimes.

5.1 Time domain analysis

The set-up is secured as explained in the previous chapter and the experiment is controlled using LabVIEW. When the jet impinges on the flat plate, the sensor flush-mounted on it generates an analog voltage signal as a function of the pressure imposed. This analog voltage is received by the NI-1301 signal conditioner which has an internal built-in amplifier that amplifies the signal and converts it into a digital form. The NI conditioner is connected to the Data Acquisition Card: NI-PCI-6250 that is in turn connected to the storage hardware. The DAQ system receives the converted digital signal and stores it in the computer which is used for further analyses.

The discrete voltage value per sample is plotted in time as shown below using MATLAB. The time signal is checked to ensure that enough number of samples are acquired. The signal is obtained as a sine wave when the sensor is along the axis of the jet. Although it maintains its basic waveform, the signal is slightly distorted as the sensor moves away from the stagnation region.

Using the sensitivity of the sensor obtained from calibration, the pressure signal PPa is computed as-

$$P = V/C \tag{5.1}$$

where V is the discrete voltage signal incurred from the A/D converter and C is the calibration constant obtained as defined by equation 4.8. In case of microphone measurements, only the fluctuating component is considered for the conversion owing to the fact that microphones can measure only fluctuating signals.

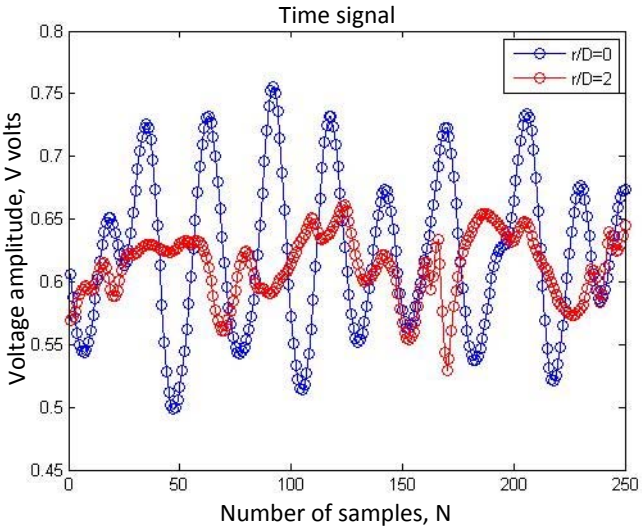

Figure 5.1: Time signal comparison at Re=5000

To check for any underlying disturbances in the signal and the consistency of the fluctuations, the convergence of the mean ($\bar{p}$) and the fluctuating components (p') of the pressure signal are checked for every measurement trial. The mean is calculated as the average of the cumulative sum of all the samples of the pressure signal and the RMS is estimated as the root of the cumulative mean of the squares of the fluctuating component of the pressure signal as described in chapter 2.

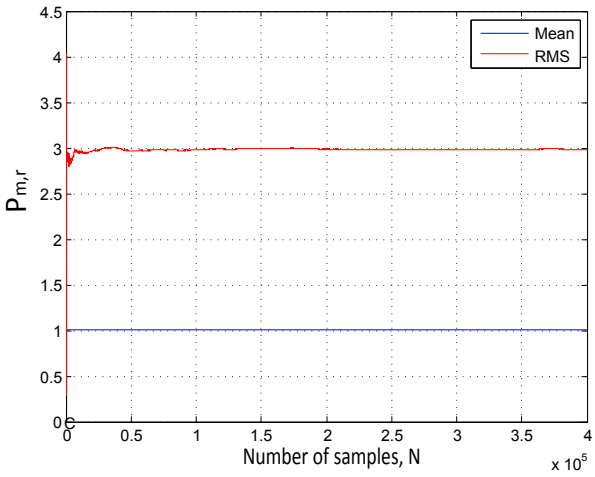

Figure 5.2: Example for statistical convergence of the pressure signal at Re=50000, r/D=0

The standard deviation of the fluctuating pressure is then obtained as square root of the variance given as-

$$\sigma = [\frac{1}{n}\sum_{i=1}^{n}(x_i - \bar{x})^2]^{0.5} \tag{5.2}$$

where n is the number of pressure samples, x_i is the i^{th} sample ranging from 1 to n, $\bar{x}$ is the mean of all the samples and σ is the standard deviation of the pressure signal. In

this case, since the area of interest is to see the fluctuations in the pressure due to jet impingement, the standard deviation is calculated using the fluctuating component of the pressure signal.

In order to establish the relative fluctuation in the sound pressure to a reference value, a logarithmic estimate is obtained. The fluctuating Sound Pressure Level (SPL) is calculated according to the formula-

$$P_{spl} = 20log_{10}\left(\frac{P_{std}}{P_{ref}}\right) \tag{5.3}$$

where P_{std} is the standard deviation of the fluctuating pressure, P_{ref} is the reference pressure of $2 * 10^{-5}$ Pa.

The mean pressure profile of the jet is plotted to check for irregularities. The mean pressure reaches a maximum at the stagnation point and reduces radially as it can be seen in figure 5.3.

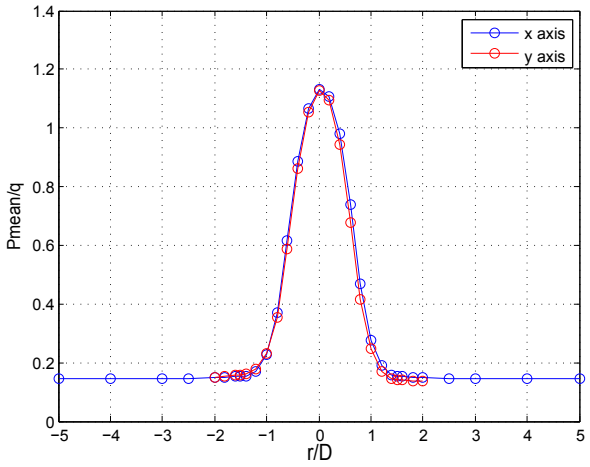

Figure 5.3: Mean pressure plot at Re=20000

Further, the standard deviation is used to plot the profile of pressure variations along the radial direction of the jet. An example of such profile can be found in the results section (figure 6.16 etc.). The information from this plot is used to interpret the characteristics of the jet at stagnation region, vortex impingement and its subsequent behaviour in the turbulent wall flow which improves the knowledge of the sources of sound generation.

5.2 Frequency domain analysis

The signal in the time domain does not give information about the energy contained in it or details of physical phenomena in the system. Hence the signal has to be converted to the frequency domain.

This is achieved by using the Welch method which is also effective in reducing the noise in the spectrum. The Welch method estimates the power spectral density of the input

signal vector using the modified periodogram method of spectral estimation. The input vector is divided into a number of segments or blocks of equal length called 'window' with half the number of samples overlapping with the previous window's samples. The length of the Fast-Fourier Transform(FFT) is specified as twice the smallest power of two that is greater or equal to the absolute value of the window length. To compute the Power Spectral Density(PSD) for the corresponding frequencies, a sampling frequency of $10000 Hz$ is used which is normalized with the exit velocity and the diameter of the nozzle to obtain the Strouhal number as described by equation 3.2. Different window lengths are employed to obtain distinct peaks that best describe the energy content in the signal acquired. A window length of 500 is chosen to be appropriate in this case.

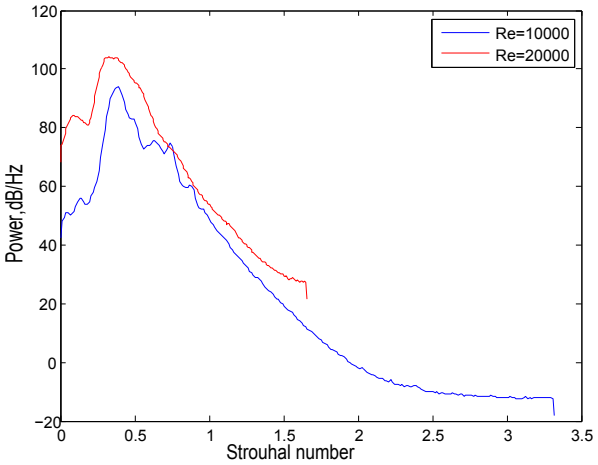

Figure 5.4: Power spectral density comparison

The figure 5.4 shows a comparison of the frequencies at two Reynolds numbers. It is seen to that all uneven oscillations are removed from the spectrum and clear peaks are obtained for interpretation. The details of each Reynolds numbers are shown in the next chapter.

For far-field measurements, an additional A-weighted filter is used to remove unwanted lower frequencies. A-weighting is the most commonly used of a family of curves relating to the measurement of sound pressure level. The weighting is employed by arithmetically adding a table of values, listed by octave or third-octave bands, to the measured sound pressure levels in dB. The resulting octave band measurements are usually added (logarithmically) to provide a single A-weighted value describing the sound; the units are written as dB(A). Though A-weighting was originally intended for low-level sounds, it is commonly used in most applications today.

In equation form, the filter is described by a weighting function that acts on the amplitude spectrum, or an offset that must be added to the unweighted sound level in dB units. It is given as-

$$R_A(f) = \frac{12200^2.f^4}{(f^2+20.6^2)sqrt((f^2+107.7^2)(f^2+737.9^2))(f^2+12200^2)} \tag{5.4}$$

$$A(f) = 2.0 + 20\log_{10}(R_A(f)) \tag{5.5}$$

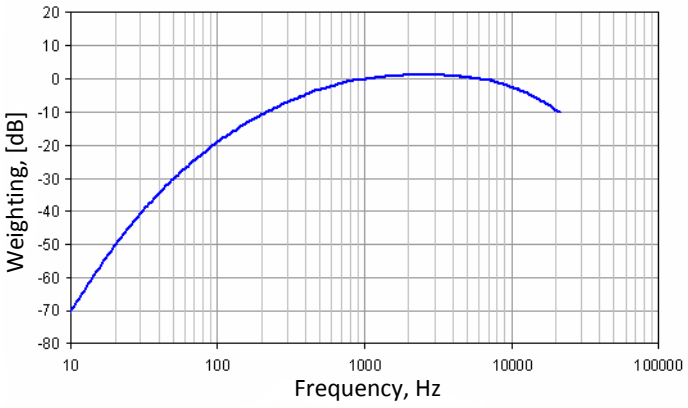

Figure 5.5: A-weighted filter

This function (figure 5.5) is applied to the output intensity of the windowed spectrum which eliminates the high intensity lower frequencies from the amplitude spectrum. The gain defined in equation 5.5 is applied to the sound pressure level and subsequently integrated over the frequency range-

$$OASPL = 20\log_{10}\left(\int_0^\infty \frac{P(f)R_A(f)}{P_{ref}}df\right) + 2.0 \tag{5.6}$$

The sound pressure levels presented in section 6.4 are all in terms of *dBA* units.

Chapter 6

Results and discussion

The previous chapters have explained about the experimental set-up, the aim of the experiments and analysis of data which has lead the reader to the discussion of the obtained results. This chapter attempts to relate the topology of the impinging jet to the pressure fluctuations caused due to impingement. Further experiments aim to describe the effect of nozzle-to-plate distances and also far-field acoustic pressure fluctuations.

6.1 Exit conditions of the jet

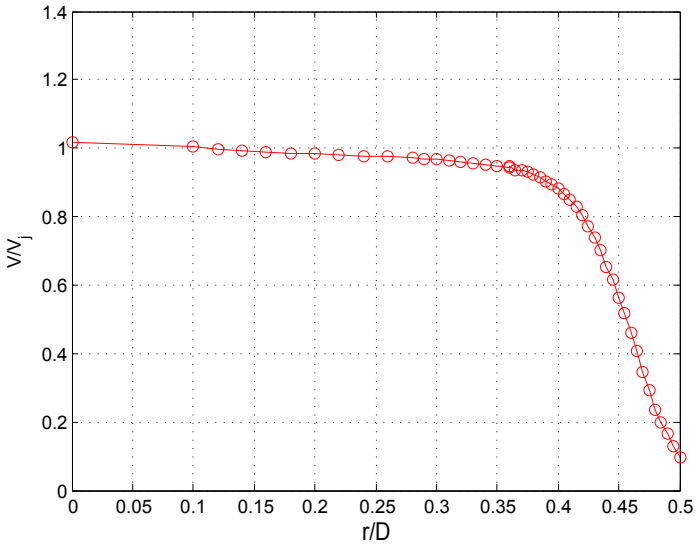

Figure 6.1: Mean Velocity profile from HFA

Hot-film Anemometry (HFA) is conducted to check if the exit conditions of the air jet is similar to that of Tomo-PIV water jet facility(refer section 4.1.1). A scan of the exit conditions at $H/D \approx 0.1$ is conducted to obtain the velocities and the frequencies at these

locations. The mean velocity profile is plotted along the radius of the jet and compared with PIV data from the water jet facility.

Figure 6.1 shows a typical velocity profile curve of a jet as obtained from measurements. This is in tandem with established concepts of round jet profile as seen in chapter 3.

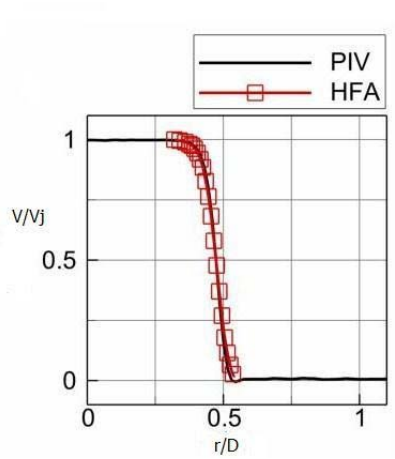

Figure 6.2: Mean axial velocity profile match of HFA and Tomo PIV

The velocity data obtained from Thin-Tomo PIV is used to compare with the HFA data. Figure 6.2 shows the velocity fluctuations from HFA overlapping that of Tomo-PIV. The velocities at the exit conditions are normalized with the jet centerline velocity V_j and are plotted along the radius of the nozzle. Since the nozzle is an axisymmetric circular boundary, the velocity profile over the diameter can be expected to be a mirror-image along the vertical axis of the nozzle.

The mean axial velocity profiles obtained by the two techniques show excellent agreement. Thus it can be said that the jet exit conditions of both techniques are the same and the experiments conducted in the air jet system for the same non-dimensional parameters as that of the PIV water jet facility would yield comparable results.

6.2 Topology of the impinging jet at different flow regimes

The first set of experiments are done to check the axisymmetry of the jet at different Reynolds number and to obtain the fluctuating pressure profiles of the round jet in the radial direction between the stagnation point and the wall jet. The standard deviations of the fluctuating pressures are plotted across the x and y axes of the jet impinging on the plate. Comparisons are made between the two to check for axisymmetry of the jet structures. Spectral analysis is done for select points that is explained in the previous chapter. These measurements are done at a nozzle-to-plate distance of $H/D = 4$ for reasons explained in 4.4.3. The flow regimes investigated in this section are laminar, transitional, turbulent and highly turbulent flows. Reynolds numbers corresponding to these regimes are selected with appropriate background information from literature as explained in each subsection and in tandem with the PIV measurement database.

6.2.1 Laminar impingement : Re=5000

The first chosen Reynolds number for investigation is 5000 which, although of the order of 10^3, still provides a laminar exit to the jet. According to Becker and Massaro (1968), upto a Reynolds number of 5500, they found a regularity in the vortex pattern beyond which the initial vortices exhibit a degree of fluctuating asymmetry. The resultant crowding of vortices due to fusion of single vortices which further increases in size appeared to have reached a limit in a flow at Re=5500. In Reynolds numbers higher than 5500, no increase in size was evident but they found a considerable degree of chaos and a tendency towards turbulent eddying. This means that the jet begins to undergo transition only further downstream for a Reynolds number of 5000. This flow regime can be counted upon to retain all the characteristics of streamwise vortices which makes it a good case for studying the impingement of the vortex rings on the plate at lower velocities.

Time-resolved Tomographic PIV measurements were conducted at the TU Delft by Violato et al., in 2011 (Appendix A) which showcased the three-dimensional structures of Re=5000 flow regime with great clarity. A sequence of images are presented in figure 6.3 to draw a relation between the pressure fluctuations detected by the sensor measurements and the coherent structures of the impinging jet. The jet in these snapshots is a section shown along the axial span of the jet with a two-dimensional view of the core of the jet, vortices, plate and the structures after impingement along the field of view on each axis (refer Appendix A). The color coding reads from dark red to blue with the former representing higher velocities and the latter representing negative velocities implying vorticity.

Figure 6.3 shows a time-resolved 2D sequence that depicts the shedding of the vortex rings, pairing and impingement. The core can be seen essentially in dark orange while the dark blue blobs travelling alongside the jet indicate the vortices moving downstream from the nozzle. The vortices induce an inward force resulting in an increase in velocity of the fluid in the regions surrounded by them which can be seen as the dark red regions of the core. Clear distinguishable regions in the flow field implies that a continuous stream of vortices are shed at regular intervals which reach the plate intact. However, in snapshot 6, it can be observed that as the jet approaches the flat plate, it begins to diverge and mix with the

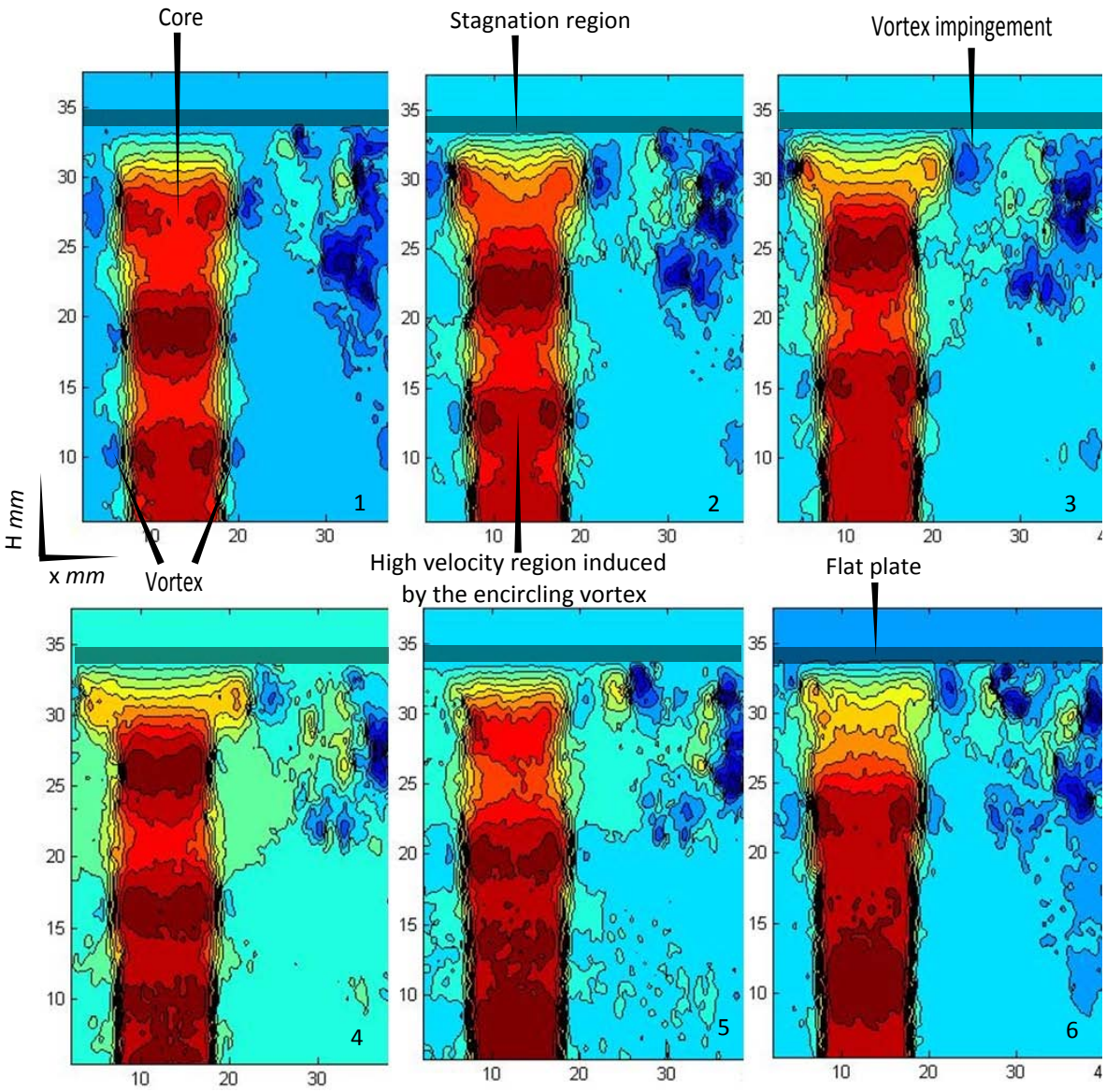

Figure 6.3: Sequence of snapshots from TR-Tomo PIV for $Re = 5000$: 2D contours are illustrated on the longitudinal mid-plane. Color code: Red to blue represents higher to lower(negative) velocities.

quiescent fluid in the surroundings. The flow becomes slightly irregular which indicates the onset of transition. This region is marked by the growth of azimuthal instabilities, along with the formation of streamwise and radial vortices which are organized in counter-rotating pairs (Daniele Violato (2011)). When the jet impinges on the plate the velocity reduces as the pressure builds up giving rise to layers of decreasing axial velocity at the stagnation region. The sequence also indicates that the vortices increases in size as they travel downstream and upon reaching the plate loses its axial velocity component and instead gains a radial component which can be seen from the vector field in figure 6.4. The vortex moves downstream of impingement region and at about $r/D \approx 2$ it completely loses its coherence, transferring its kinetic energy to smaller scales of turbulence and from

there on leading to molecular diffusion of momentum.

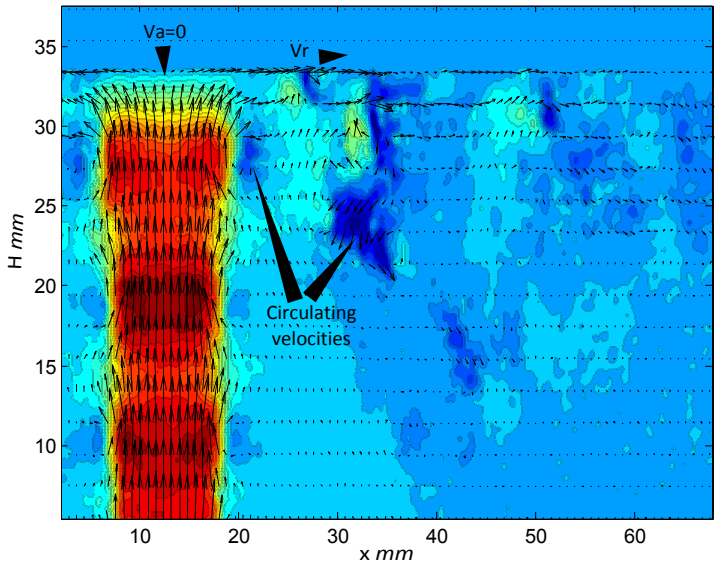

Figure 6.4: Vector field indicating the flow evolution in a laminar jet impingement

In the sample vector field shown via figure 6.4, Va represents the axial velocity and Vr represents the radial velocity components of the jet. At the boundary of the flat plate the vectors can be seen to change their vertical orientation to gain a horizontal component of the velocity. The build up of pressure at the stagnation region of the plate tends to induce an opposite force which drives the incoming vectors to change their orientation in the radial direction, thus resulting in the Vr component gaining magnitude. Additionally, circulating vectors can be spotted in the dark blue regions which represents the vortices along with a pulsating pattern formed by these structures and entrainment of fluid.

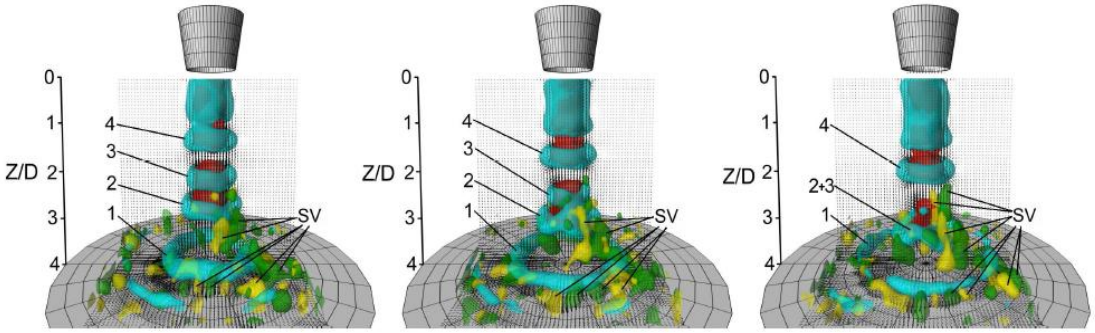

Figure 6.5: Impinging flow structures [Daniele Violato (2011)]

Previous experiments conducted by Violato et al. at Re=5000 are also presented here to assist explanation on the pairing phenomenon. In the sequence of figure 6.5, vortices are represented from 1-4. Vortex shedding begins at about $H/D = 1.5$ and increases in size as they proceed downstream. When the vortices are nearly at three diameters from the nozzle, vortex 2 and 3 begin to merge due to velocity differences as explained in

chapter 3 causing an increase in vortex spacing. They undergo pairing before impinging on the plate and travel radially breaking down into smaller turbulent scales. The axial accelerations produced by the pulsatile motion leads to the growth of three-dimensional structures such as longitudinal vortices of radial and streamwise vorticity designated as SV in the figure.

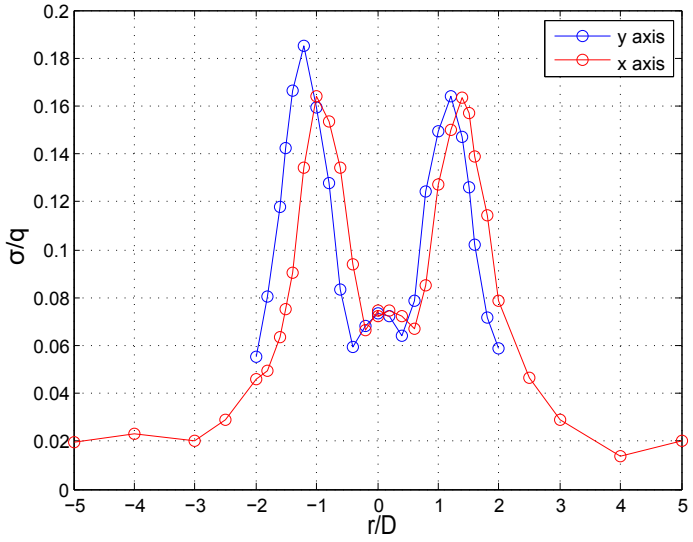

Figure 6.6: Normalized standard deviation of pressure fluctuation profile for Re=5000

In this chapter the surface pressure variations caused by impingement of these vortices on the flat plate as detected by the sensors is explained. A profile of the standard deviation of pressure fluctuations along the radial direction is plotted as shown in 6.6.

The profile scanned along the positive and negative x and y axes shows a good degree of overall axisymmetry. The standard deviation of the pressure fluctuation (σ) is normalized with the dynamic pressure (q) of the flow corresponding to its velocity found from the pitot probe measurements as explained in the section 4.4.3. The flow impinges normally on the plate with the sensor (in this case the microphone) and deflects radially. The radial fluctuations are captured by acquiring data at each point. The profile shows that the fluctuations are lower in the impingement region than the radial wall jet. The highest pressure fluctuation seen at $r/D \approx 1.2$ is nearly 60% more than that observed at the stagnation point and can be attributed to the impingement of vortices. The local differences at axisymmetric points can be assigned to the pairing induced azimuthal distortions in the vortices impinging on the plate. The most distinct difference is spotted at the point of impingement with the negative y-axis showing a nearly 11% increase compared to the maximum deviation of 0.164 on the other axisymmetric points. This is also discussed by Violato and Scarano (2011), who show that after a vortex pairing event, the vortex rings gradually lose their axial symmetry and the azimuthal perturbations becomes more prominent with noticeable peaks of the out-of-plane waves. Thus the change in the amplitude of fluctuations at axisymmetric nodes can be assigned to the deformation of the impinging structures. Two maxima can be observed in the overall profile with one at the stagnation point and the other at the region of vortex impingement while a single minima in the profile occurring close to the stagnation point at $r/D = 0.4$.

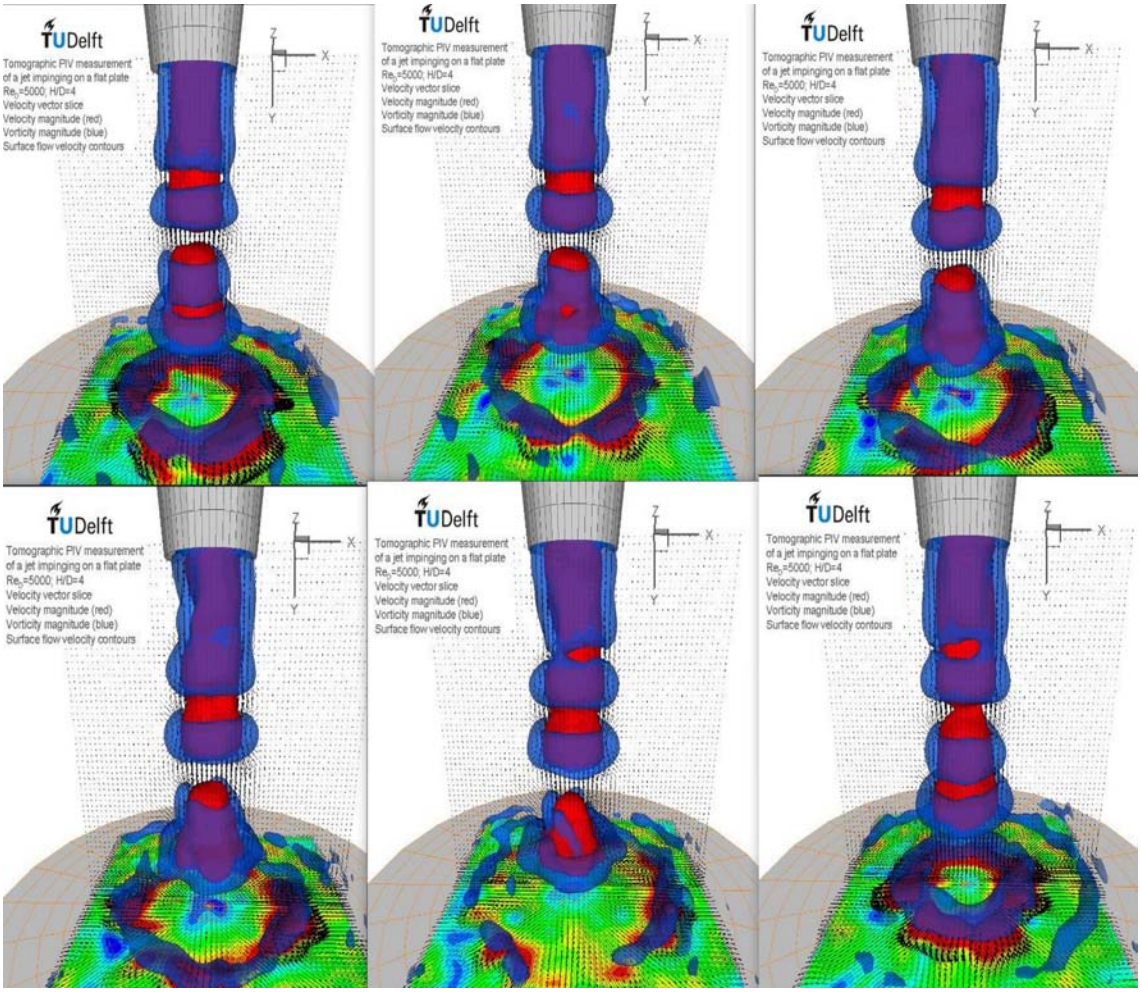

Figure 6.7: Sequence of vortex impingement at Re=5000 and H/D=4. (Courtesy:Violato and Scarano)

The pressure fluctuations increase further downstream of radial distance until it reaches the peak which defines the impingement of primary coherent structures (Didden and Ho (1985), Ho and Nosseir (1981) etc.). The pressure fluctuations decreases further indicating the decay of vortex rings. Also measurements conducted up to $5D$ on the x-axis indicates that the pressure fluctuations tend towards zero as they proceed further in the radial wall jet. This also indicates that there are no significant changes in the pressure distribution caused by the turbulent eddies downstream. No details of formation and development of smaller scale structures in the turbulent boundary layer can be inferred from this experiment due to single-point measurements and limited two-dimensional spatial resolution of data points.

The maxima in the radial region can be attributed to the circulating velocities of the toroidal structure impinging on the plate which causes a peak in the pressure fluctuation. However, the smaller maxima at the stagnation point exhibiting 60% lesser pressure fluctuations, where only the core is known to impinge on the plate can be explained based on the sequence in figure 6.7 and figure 6.8 obtained from Tomo PIV measurements. The

sequence clearly shows the generation of the toroidal structures from the shear layer, shedding and pairing of vortices that impinge on the plate. Red represents the velocity magnitude and the blue represents the vorticity magnitude. Near the nozzle edge a pulsating flow can be observed closely that depicts the continuous initiation of the vortex. The intermittent blue field in the stagnation region on the plate when the vortex approaches the plate could possibly mean that there is rotation of fluid in that region.

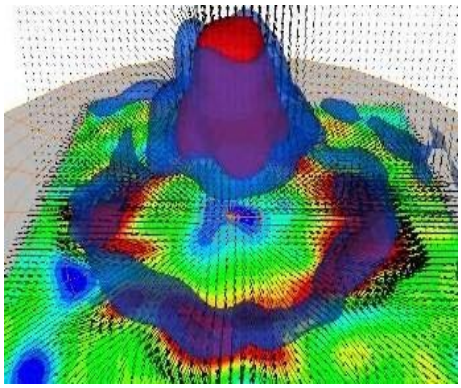

(a) Vorticity vectors in the stagnation area

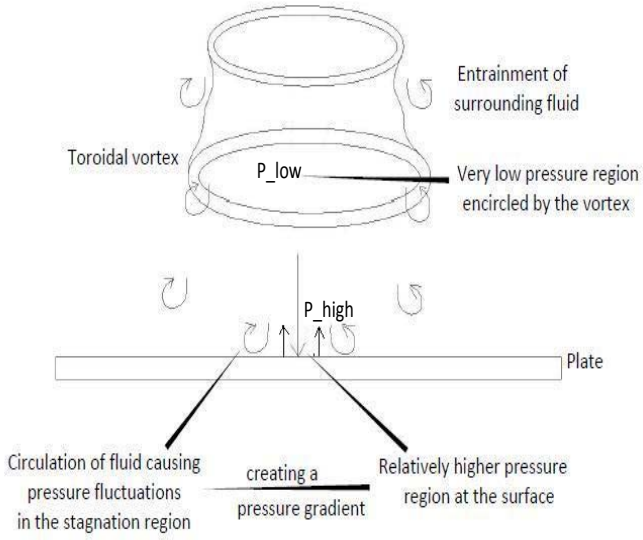

(b) Description of the circulation phenomenon

Figure 6.8: Circulation in the stagnation region

In this sequence, the field of circulating velocities on the plate is limited to few tenths of the nozzle diameter. From the flow vectors it can be noticed that as a vortex moves downstream from the nozzle, it draws the surrounding fluid into the jet stream and increases in size. The core of the vortex is made up of higher velocities and very low pressures than the surroundings. It can be speculated that as the core surrounded by the (paired)vortex approaches the solid boundary, it causes a pressure gradient between the core fluid and the fluid near the plate. The combination of low pressure in the core and the

circulating velocity of the vortex results in a suction pressure inwards of the jet. As the enlarged toroid impinges, the pressure gradient tends to zero again until the next vortex is sufficiently close enough to cause an inbound motion of the fluid near the boundary. At the instant of impingement, the core produces a maximum mean pressure value at stagnation. Figure 6.8a shows the close up of the stagnation region where the vorticity field can be observed and figure 6.8b gives a pictorial representation of the physical process. Observing the sequence, it can be remarked that this pressure difference is caused only when the core fenced in by the vortex is sufficiently close enough to the plate to cause a gradient that the inward force of the rotating vortex elements can act upon. This fluctuation in pressure at stagnation could possibly explain the cause of a maxima as seen in the figure 6.6 at r/D=0. These fluctuations appear to reduce away from the stagnation point reaching a minima near one nozzle radius distance on the plate and then continuously increase downstream owing to the approach and impingement of the vortices.

Frequency Spectra

Signals acquired for various radial distances gives comprehensive data on the development and impingement of structures on the flat plate. Following the spectral analysis procedure described in chapter 5, two distinct peaks can be observed in the spectra corresponding to the frequency of vortex shedding and vortex pairing in the lower end of the spectrum while smaller peaks are detected at higher frequencies.

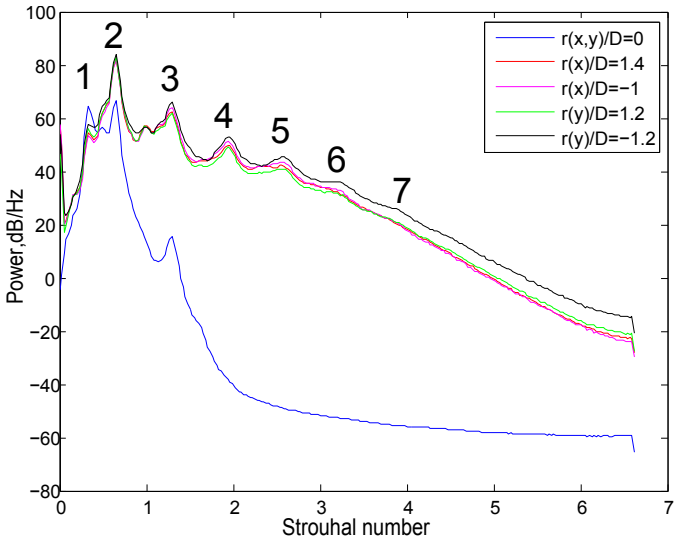

Figure 6.9: Spectral comparison for Re=5000

In the spectrum for stagnation point(r/D=0), two clear peaks are visible in the lower frequency range while in the region of impingement(r/D=1-1.4), one distinct peak and its harmonics are visible. The peak numbered 1 at a Strouhal number of 0.34 corresponds to the frequency of vortex pairing in tandem with the findings of Daniele Violato (2011) through time-resolved PIV. This frequency exhibits more energy at the stagnation region than compared to the radial wall jet region where the power is nearly 17% less than that of r/D=0. This implies that pairing is not prominently influential in the radial jet field. However, the secondary peak is much stronger in the outer regions of the jet as

compared to the stagnation point. The peak marked 2 corresponds to St=0.65, close to the value of St=0.72 as determined by Daniele Violato (2011). The conflict of nearly 10% found could be attributed to the differences in the experimental set-up and medium used for investigation. The energy of the pairing and shedding vortices appear to be almost the same at stagnation point with the shedding frequency being just 3% stronger than pairing. At St=0.65, the PSD at downstream of the stagnation point where the pressure fluctuations are maximum is nearly 21% higher than that of stagnation point, clearly indicating that it is indeed due to vortex impingement. Other harmonics can be observed in the higher frequency range which are integral multiples of the frequency of vortex shedding. A total of 5 harmonics are visible through this spectrum in the radial field where as only one harmonic is evident in the stagnation region.

Table 6.1: Characteristics of Re=5000

Parameter	Value in units
Normalized σ_{max}	0.164,0.1849
SPL_{max}	110 dB
$St_{shedding}$	0.65
$St_{pairing}$	0.34
Dimensional shedding frequency	490.75 Hz
Dimensional pairing frequency	256.7 Hz

6.2.2 Transitional impingement : Re=10000

According to Becker and Massaro (1968), the flow regime beyond a Reynolds number of 5500 shows an increase in the degree of fluctuating asymmetry, exhibiting a tendency towards turbulent eddying and as the point of turbulent breakdown advances, only a single, rather chaotically structured vortex is visible after fusion of enlarged vortices. Yule (1978) also observed through hydrogen-bubble visualizations of transitional flow at $Re = 9000$ that vortices coalescing away from the nozzle are seen as relatively disorganized, diffuse region of bubbles that remain coherent for several nozzle diameters downstream of the end of the transition region. A Reynolds number of 10000 can thus be treated as an appropriate case for studying transitional jets impinging on a plate.

Figure 6.10 shows a time-resolved sequence of snapshots obtained from TR-PIV. In the sequence, clearly visible are the vortical structures surrounding the core inducing higher velocities in this region. As compared to the snapshots at $Re = 5000$, it can be noticed that the vortices are smaller in size. Snapshot 1 and 2 clearly indicate that the flow begins to spread and mix with the surrounding air much more upstream as compared to $Re = 5000$. Nearing the flat plate, the jet almost turns chaotic denoting the onset of turbulence. A pulsating core produced due to the convection of regular toroidal vortices as described by Popiel and Trass(1991), can be clearly visualised in snapshot 5. This generates some kind of "vortex action upstream" that synchronizes the appearance of a new instability wave and consequently vortex birth around the entire circumference. Vortex pairing can also be observed in the 5^{th} snapshot with the later vortex catching up with the former and merging into one, as observable from the core of the 6^{th} snapshot.

The vector field shown in figure 6.11 for this flow regime clearly displays the diverging

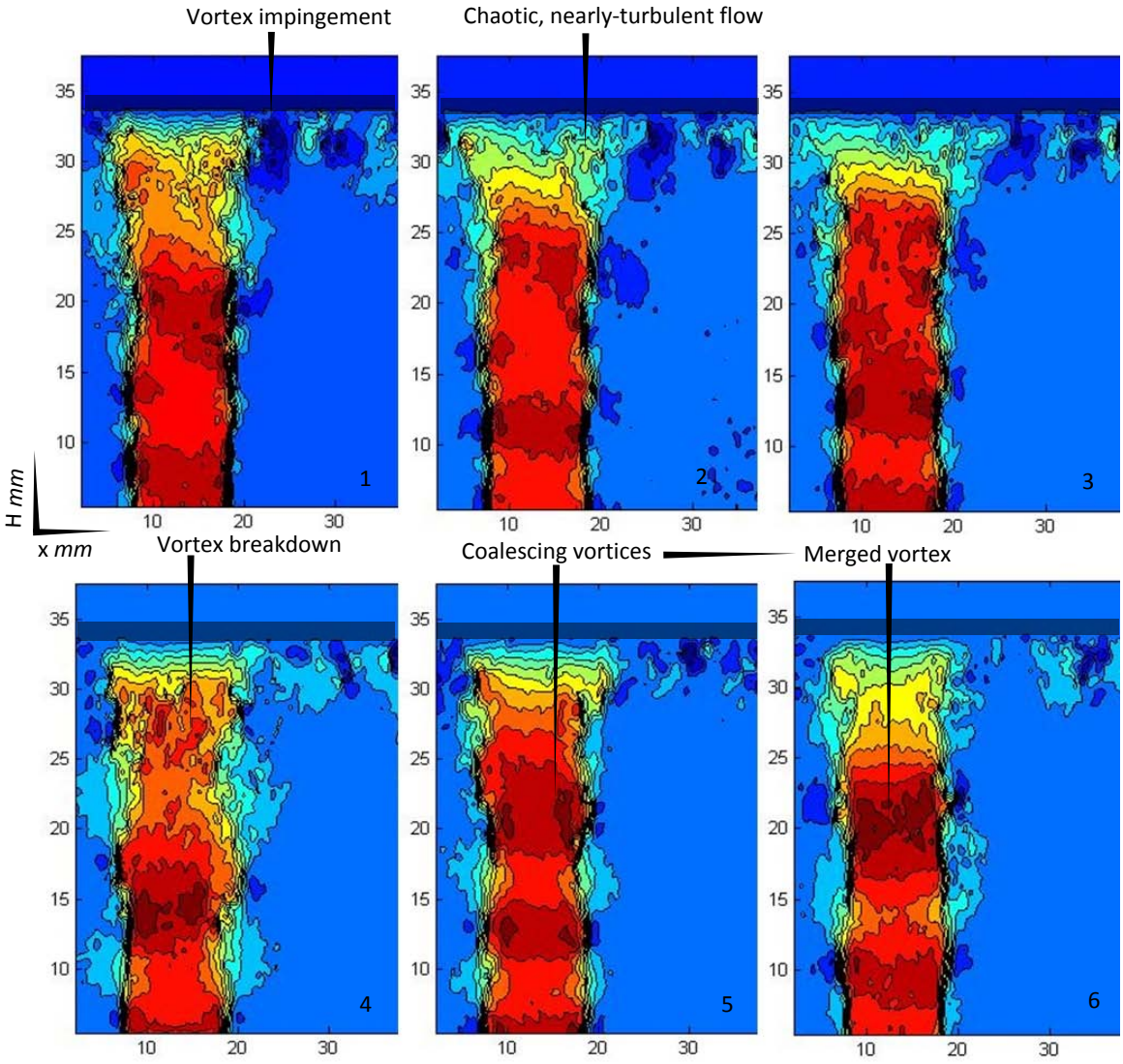

Figure 6.10: Sequence of snapshots from TR-Tomo PIV for $Re = 10000$: 2D contours are illustrated on the longitudinal mid-plane. Color code: Red to blue represents higher to lower(negative) velocities

velocity vectors downstream of the nozzle, much before reaching the solid boundary. The structure does not have a clear shape like that of the laminar case near the impingement region which signifies transition. The jet is much more spread out and the velocities are lower. Also, inward bound vectors in the radial interface of the free jet region demonstrates entrainment of surrounding fluid in between the structures that leads to the spreading of the jet.

As with the previous case, a profile plot of the wall pressure fluctuations is obtained for $Re = 10000$ as shown in figure 6.12. It follows the same trend as in $Re = 5000$ and the standard deviation of the pressure fluctuations are nearly the same too. The standard deviation along the wall of the jet shows two maxima-one at the stagnation point and one in the region of impingement and a minima at $r/D = 0.6$. The maximum standard

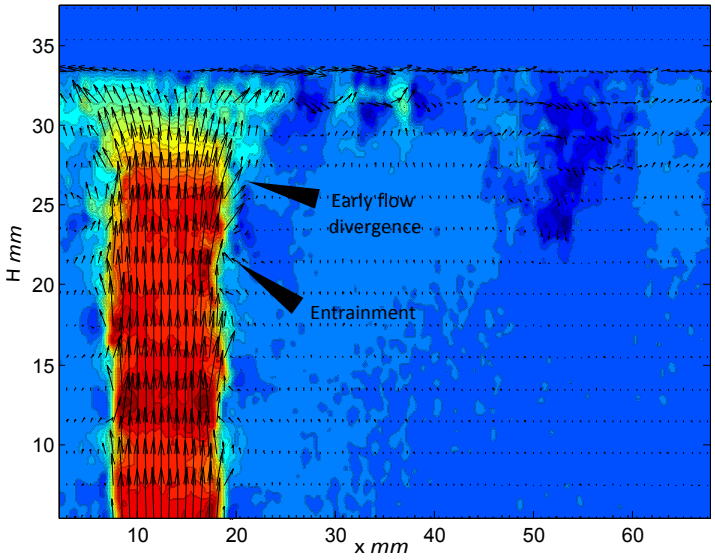

Figure 6.11: Vector field indicating the flow evolution in a transitional jet impingement

deviation occurs in the region of $r/D = 1.2 - 1.4$. There is a 38% increase in this region as compared to that of the stagnation point. Similar to the previous case, two maxima can be observed in the profile. The maxima at $r/D = 1.2 - 1.4$ is due to the high pressure fluctuations caused by toroidal impingement and the one at the stagnation point can be supposed to occur due to the pressure gradient caused by the high velocity core of the jet as explained with PIV profiles for the laminar impingement case. Even though the maximum pressure variation is comparable to that found at $Re = 5000$, the stagnation region shows nearly 35% higher fluctuations compared to that of laminar impingement case. The pressure fluctuations decrease away from the impingement region and tend towards zero as tested on the x-axis. The positive x and y axes shows a higher fluctuation than that of the negative axes pointing towards azimuthal distortions of the structures. As with Re=5000, no details of smaller scales of turbulence can be deciphered from this plot.

Frequency Spectra

Figure 6.13 shows the Fourier decomposition of the surface pressure fluctuations, providing information on the events in this regime. The frequencies are comparatively more broader than that of $Re = 5000$. The spectra shown here are for the stagnation and the vortex impingement region. At the stagnation point, a large peak can be seen at $St = 0.38$ which corresponds to the frequency of vortex pairing. The vortex shedding frequency is located at $St = 0.73$ exhibiting less energy compared to the pairing frequency. The pairing frequency shows the highest power levels compared to all radial points. Intermittent peaks can be found at $St = 0.13$, $St = 0.63$ and $St = 0.87$ which could possibly signify passage of smaller and less powerful structures at sporadic intervals.

Yule (1978) identifies in his paper that the transition region is characterized by a growth of three-dimensional flow due to a wave instability of the cores of the vortex rings. The merging of these distorted vortices produces large eddies which can remain coherent upto

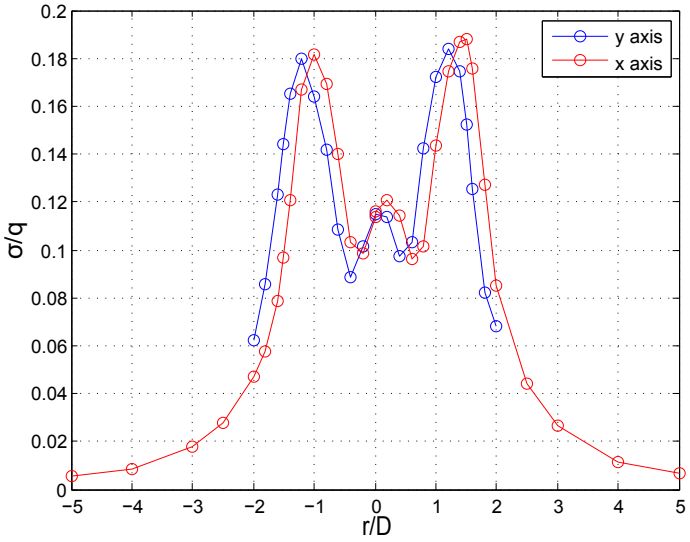

Figure 6.12: Normalized standard deviation of pressure fluctuation profile for Re=10000

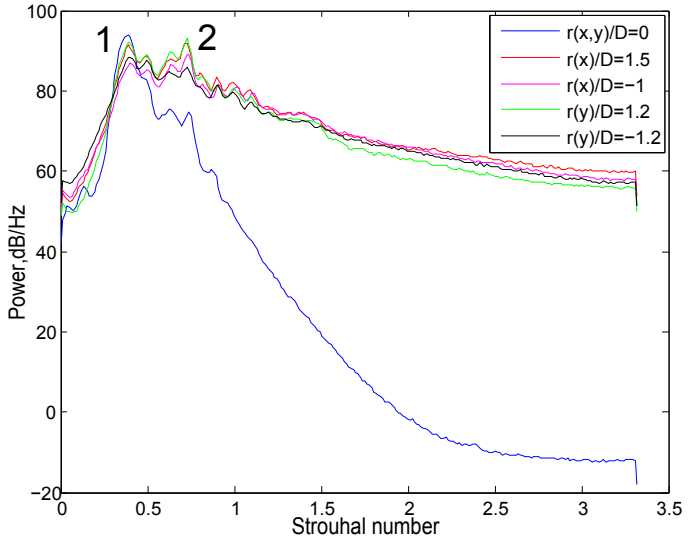

Figure 6.13: Spectral comparison for Re=10000

the end of the potential core. Similar structures could possibly account for the intermediate frequencies seen in the spectrum. In the radial positions where the vortex is known to infringe on the plate, the frequency of pairing and shedding nearly have the same power along with two smaller but well-defined peaks at $St = 0.49$ and $St = 0.63$ which could possibly represent irregular structures formed at the end of the jet length due to transition of the flow into turbulent stream. Independent peaks of lower energy are visible beyond the shedding frequency that does not correspond to the harmonics of the natural frequencies that occur in the lower frequency range. These individual frequencies can be attributed to the less powerful structures formed during transition that eventually transform into smaller scales of turbulent flow.

Table 6.2: Characteristics of Re=10000

Parameter	Value in units
Normalized σ_{max}	0.1878
SPL_{max}	122 dB
$St_{shedding}$	0.73
$St_{pairing}$	0.38
Dimensional shedding frequency	1098.3 Hz
Dimensional pairing frequency	571.71 Hz

6.2.3 Turbulent impingement : Re=20000

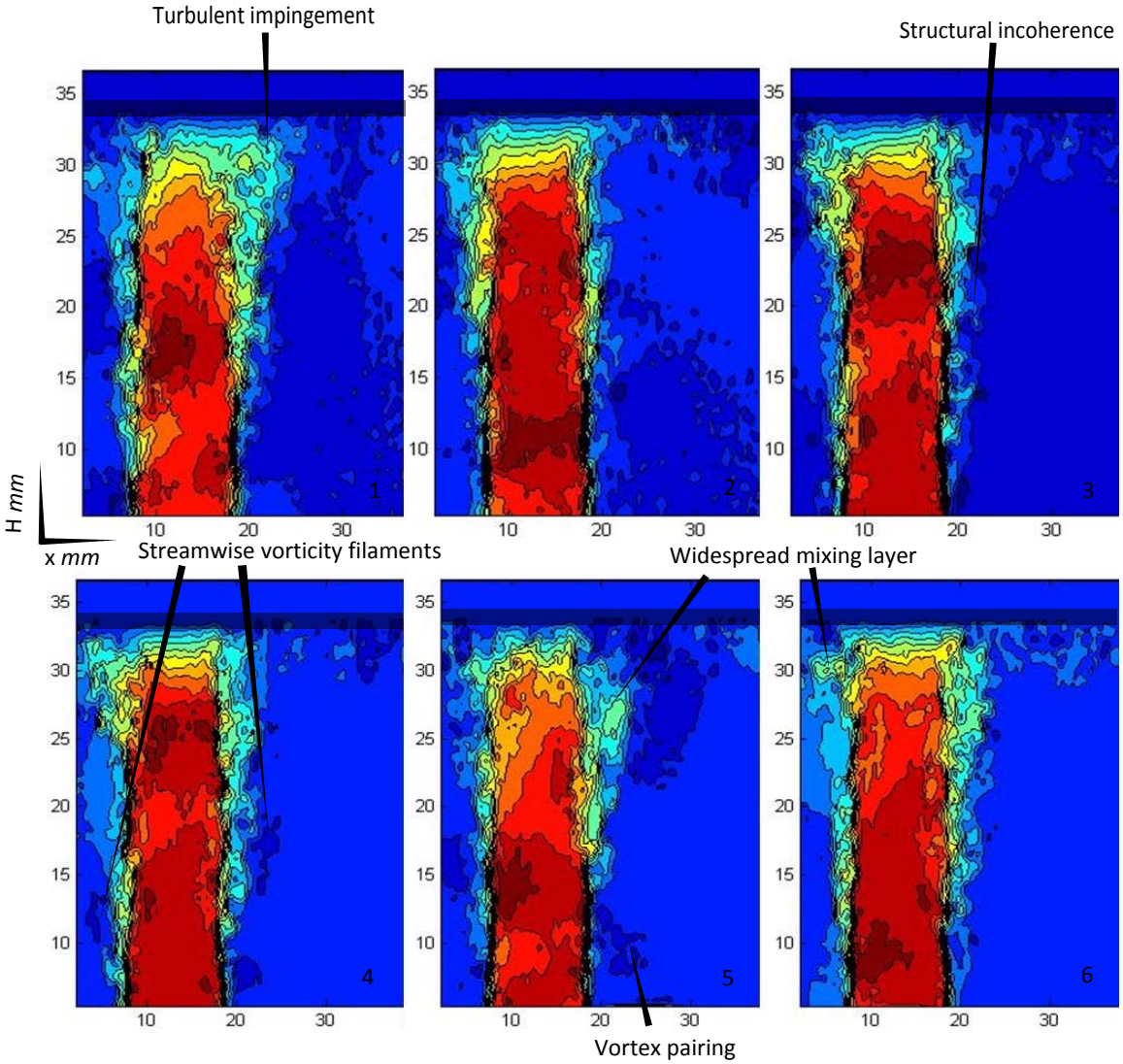

Figure 6.14: Sequence of snapshots from TR-Tomo PIV for $Re = 20000$: 2D contours are illustrated on the longitudinal mid-plane. Color code: Red to blue represents higher to lower(negative) velocities

According to Becker and Massaro (1968) in the range of $10000 < Re < 20000$, the cylindrical symmetry of the initial disturbance disappears and the evidence of vortex fusion dissolves completely into turbulent chaos. It has been characterized that the flow in this regime is a well developed turbulent mixing layer. Thus $Re = 20000$ is a good case for the study of turbulent jets impinging on a flat plate.

Figure 6.14 shows a sequence of snapshots obtained at $Re = 20000$ through PIV. In this sequence, it can be observed that the structures are smaller and more irregular as compared to lower Reynolds numbers. A clear circular cross-section of the vortices is no longer visible in this flow. However, convection of distorted fragments of vortex elements can be observed. The jet fluid begins to mix with the surrounding quiescent fluid earlier upstream and the flow exhibits chaos as it convects downstream. In snapshot 5, two subsequent vortices can be found to coalesce producing large regions of high velocity flow in the core. Irregularly shaped vorticity elements can be found downstream of the nozzle as shown in snapshot 3 and 4 that appear like streamwise vorticity filaments. This could influence the fluctuations at axisymmetric pressure points. The velocity vector field in figure 6.15 also supports the description of early turbulence onset and growth of mixing layers at a much more upstream location than at lower Reynolds numbers.

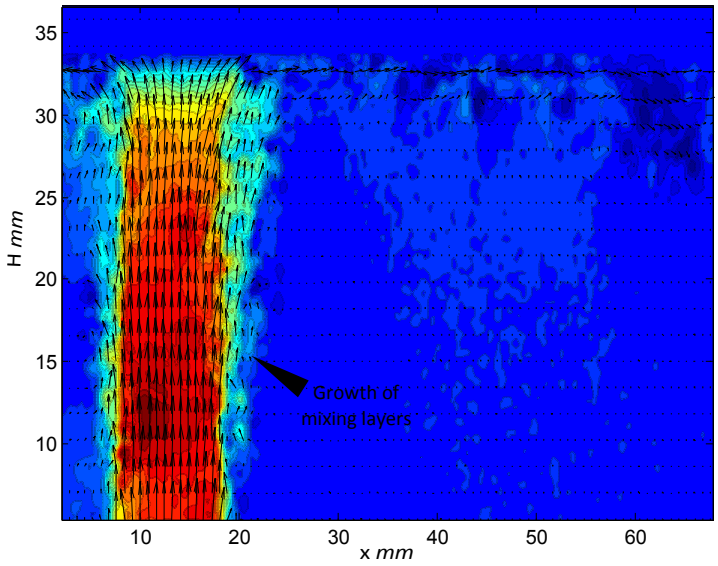

Figure 6.15: Vector field indicating the flow evolution in a turbulent jet impingement

The pressure profile developed across the radial sweep along the axes is presented in the figure 6.16. The negative axes shows nearly 9% higher pressure fluctuations than the positive axes which signifies the deformation in the structures impinging on the surface. The vortex elements impinge upon the plate at $r/D \approx 1.2 - 1.4$. The profile shows two maxima similar to the lower Reynolds numbers, one at the stagnation point and the other at the point of impingement. The pressure fluctuations decreases after impingement and tends towards zero as the radial distance increases. Compared to the lower Reynolds numbers, the maximum standard deviation of the pressure fluctuations is lower by 33.5% which suggests that the structures impinging are less coherent and more irregular in nature.

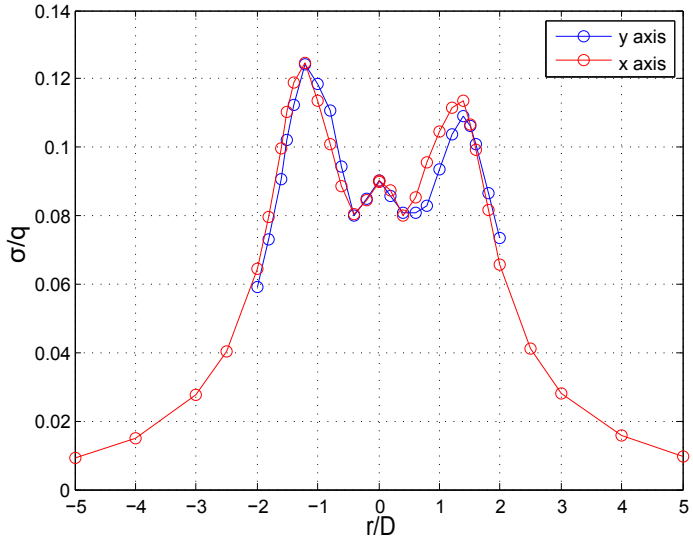

Figure 6.16: Normalized standard deviation of pressure fluctuation profile for Re=20000

Frequency Spectra

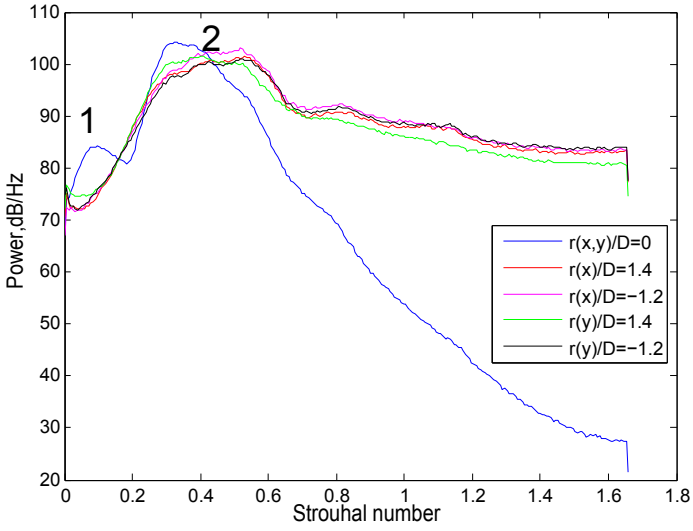

Figure 6.17: Spectral comparison for Re=20000

Figure 6.17 shows the distribution of frequencies in a turbulent jet. The most prominent feature of these frequencies is the broader peaks compared to those obtained at lower Reynolds numbers. Unlike earlier flow regimes, the frequencies of vortex shedding and pairing cannot be easily distinguished in the radial jet region. The stagnation region shows a high power slightly-broad spectrum at $St = 0.33$ along with a lower energy peak at smaller frequency corresponding to $St = 0.097$. This could represent the pairing frequency of the toroidal structures and the decrease in non-dimensional frequency compared to the previous flow regimes suggests that the number of pairings decreases as the Reynolds number is increased. In the radial region, the peaks in the region of impingement are broader than that of the stagnation point. This suggests a more aperiodic passage of

vortices at higher Reynolds numbers. In these radial points, the frequencies are also nearly 27% lower with a Strouhal number of 0.52 as compared to smaller Reynolds numbers flows.

Table 6.3: Characteristics of Re=20000

Parameter	Value in units
Normalized σ_{max}	0.1248
SPL_{max}	130 dB
$St_{shedding}$	0.52 at $r/D \approx 1.4$
$St_{pairing}$	0.09 at $r/D = 0$
Dimensional shedding frequency	1566.1 Hz
Dimensional pairing frequency	271.06 Hz

6.2.4 Highly turbulent impingement : Re=50000

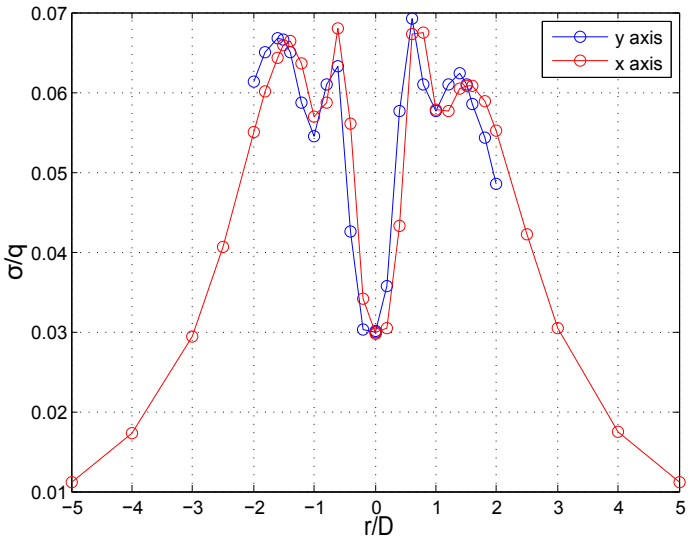

Figure 6.18: Normalized standard deviation of pressure fluctuation profile for Re=50000

For investigating a highly turbulent flow, a Reynolds number higher than 20000 had to be chosen. Following Hall and Ewing(2006) and considering the maximum attainable pressures in the jet facility, a Reynolds number of 50000 was chosen. Also $Re = 50000$ is a good choice for far-field acoustic measurements since the sound pressure levels are more apparent due to the highly turbulent nature of the flow. Currently no PIV data are available for this Reynolds numbers that can provide a better insight into the structures in a jet. However, the variation of standard deviation of the pressure fluctuation along the x and y axes is presented in figure 6.18.

The pressure profile shows a steep increase in the fluctuations between the stagnation and the vortex impingement region unlike the gradual increase for other flow regimes. The primary vortex impingement is at $r/D = 0.6$ which suggests that the size of the impinging vortex is nearly half of that at lower Reynolds numbers. A considerable dip in the maximum fluctuations can be observed as compared to other Reynolds numbers indicating that the vortex impinging is less coherent and weaker.

The instantly notable change in this flow regime compared to the previous cases is the presence of a second peak at $r/D = 1.4 - 1.5$. Didden and Ho (1985) have conjectured the presence of the dip in pressure fluctuation in the radial jet as unsteady separation of vortices. They supposed that the radially spreading vortex ring structures imposed an unsteady pressure gradient as they passed along the wall causing secondary regions of counter-rotating vortices to form in the near wall flow beneath the ring structures. The secondary structures were convected faster than the primary structures and were ejected from the near wall region at $r/D = 1.4$. However, this phenomenon was observed at $Re = 19000$ and at $Re = 6564$ by Landreth and Adrian (1990) through PIV measurements. Further investigation through flow visualisation is necessary to confirm the occurrence of separation in the current case of $Re = 50000$. Although, the secondary peak can be attributed to the fact that once the primary vortex impinges at $r/D = 0.6$, it moves with a higher velocity along the surface causing a decrease in the pressure on the wall which leads to the build up of the boundary layer. This stimulates the primary vortex to separate and form a comparatively less stronger secondary vortex that interacts with the flat plate at $r/D = 1.4 - 1.5$. The dip in pressure fluctuations is small and the secondary structure developed interacts with the plate quickly after separation. The maximum standard deviation is 44.5% lower compared to that of $Re = 20000$. The logarithmic estimate of the power produced by these fluctuations in the near-field is $141 dB$ which evokes an interest in investigating the acoustic implications of this Reynolds numbers.

Frequency Spectra

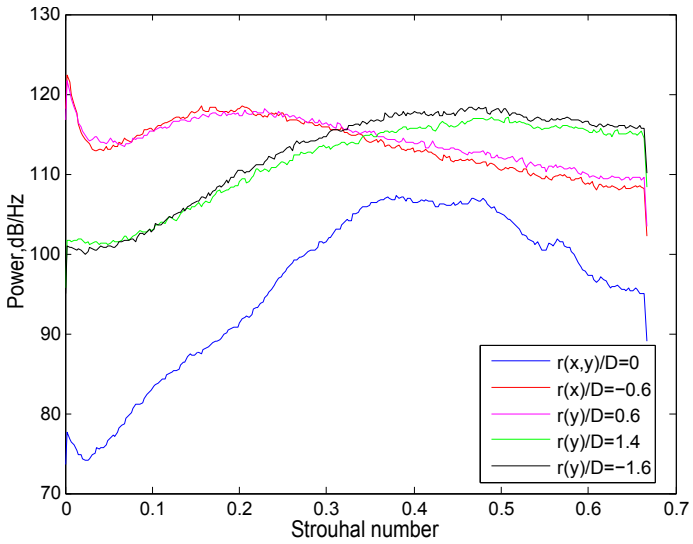

Figure 6.19: Spectral comparison for Re=50000

The spectral distribution for $Re = 50000$ is shown in the figure 6.19. It exhibits a broadband spectrum in both the stagnation as well as the outer wall region indicating that the passage of vortices is highly aperiodic. The peaks shift from around $St = 0.38$ towards larger frequencies and displays higher power at around $St = 0.47$ in the outer radius of the jet. Even though aperiodic in the region of impingement of the primary vortex, the peak can be found at lower non-dimensional frequencies in the range of $St = 0.18$ which suggests

that the vortices pass with a lower convective velocity compared to that of the secondary structures interacting with the plate in the radial regions of the jet. To elaborate, in the non-dimensional frequency parameter in consideration (Strouhal number (St)), the characteristic length and the velocity remains constant for a particular Reynolds number while only the frequency changes. Frequency being dependent on time and velocity of the system, when increases-as in the case of the frequencies obtained in the radial wall jet region-indicates that the time taken for these structures to pass is lower. Hence it can be said that the convective velocity of the primary vortices is lower than that of the secondary vortices. The power of the peak at stagnation is nearly 10% lesser than that at the radial positions indicating that the core of the jet is weaker.

Table 6.4: Characteristics of Re=50000

Parameter	Value in units
Normalized σ_{max}	0.06918
SPL_{max}	141 dB
$St_{pri.impingement}$	0.18
$St_{sec.impingement}$	0.38 to 0.48
$St_{stagnation}$	0.38 to 0.48
Dimensional frequency at stagnation and sec. impingment	2850 to 3600 Hz
Dimensional frequency at primary impingement	1125 Hz

6.3 Investigation of the secondary peak at higher Reynolds numbers

At higher Reynolds numbers such as that described in section 6.2.4, along with a peak in the region of impingement closer to the stagnation point, an additional peak of slightly lower fluctuation is observed downstream of the plate at $r/D \approx 1.5$. This section describes a set of measurements that is aimed at investigating the onset of this secondary peak in terms of nozzle-to-plate distance and Reynolds numbers.

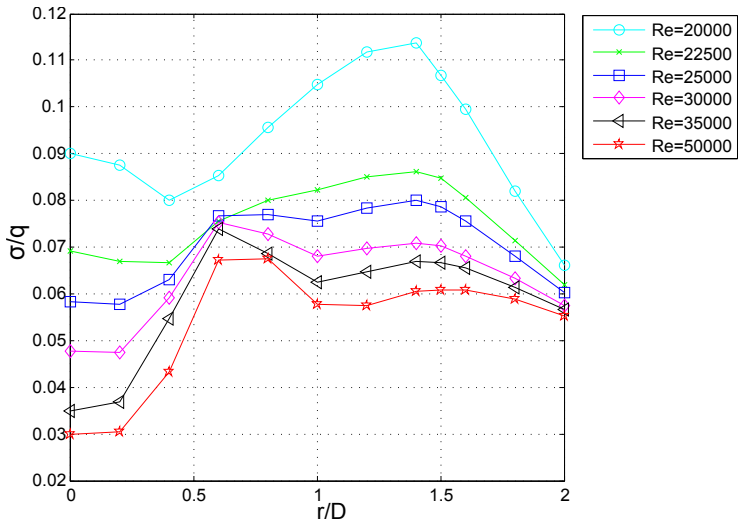

Figure 6.20: Comparison of normalized standard deviation of pressure fluctuation profiles for different Reynolds numbers at H/D=4

A series of measurements are made using the same procedure as before to obtain the fluctuations induced due to impingement of the jet at different nozzle-to-plate distances. Since axisymmetry is well established from the previous sections, signals are acquired only along the positive x-axis of the jet for the discussion presented in this section.

Firstly, it is sought to examine at approximately which Reynolds number the secondary peak begins to develop since this behaviour is not seen at $Re = 20000$ but at $Re = 50000$ in the first set of measurements. At $H/D = 4$, pressure profiles for various Reynolds numbers ranging in between 20000 and 50000 are produced starting from highest. Later on, the progress of this peak along different distances from the nozzle are checked at these Reynolds numbers. The results are presented below with analysis and comparison.

Referring 6.20, while a hint of change in the pressure profile can be found in $Re = 22500$ at $r/D = 1$, a clear dip in the pressure fluctuations can be found at a Reynolds number of 25000 in the same radial position. The standard deviation begins to increase beyond this position reaching a peak at $r/D = 1.4$. This peak becomes increasingly pronounced for all greater Reynolds numbers there on. Another change that can be observed from these measurements is at the stagnation region. The evident maxima of the wall pressure fluctuation at the stagnation point observed at lower Reynolds numbers tends to decrease such that the change in the fluctuations between $r/D = \pm 0.2$ is nearly zero. This suggests that as the Reynolds number increases, the jet becomes increasingly turbulent and the

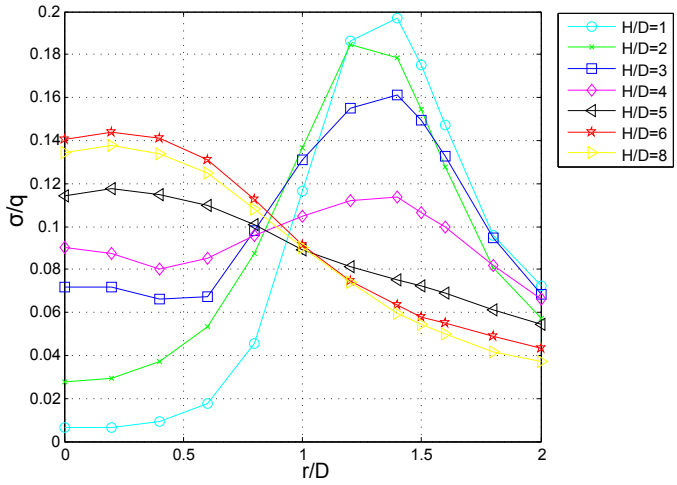

(a) Re=20000

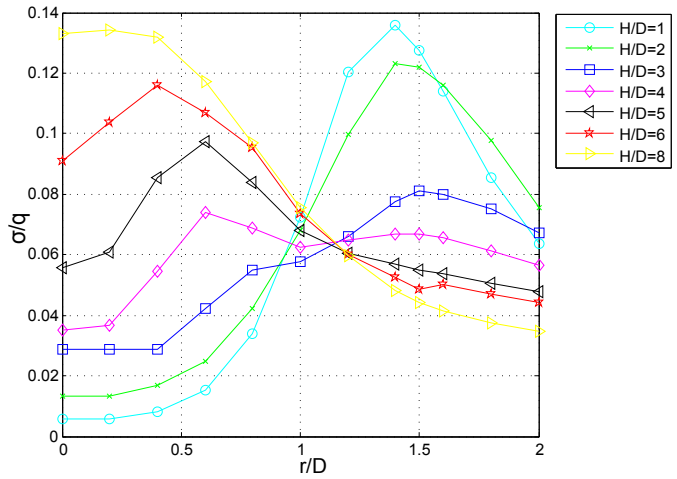

(b) Re=35000

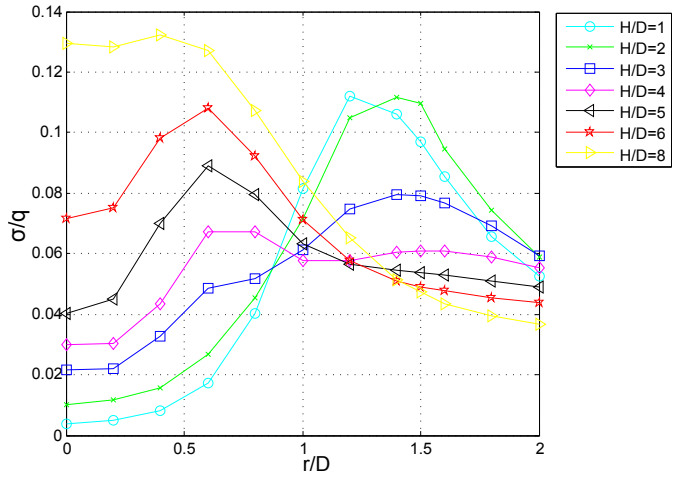

(c) Re=50000

Figure 6.21: Comparison of normalized standard deviation of pressure fluctuation profiles for different nozzle-to-plate distances at various Reynolds numbers

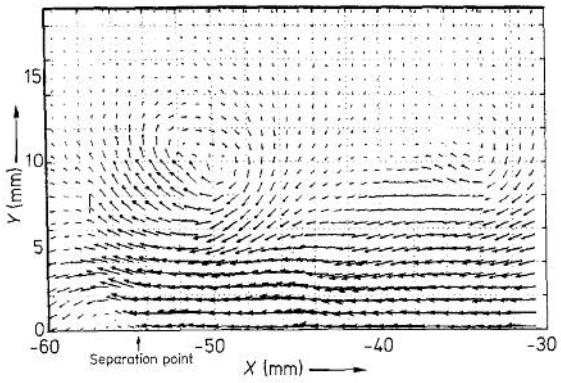

Figure 6.22: Vector field showing interaction of primary-secondary vortex pair interaction(Landreth and Adrian (1990))

effect of vortices on the pressure difference between the core and the air at the plate as described in 6.2.1 decreases giving rise to nearly constant pressure fluctuations in the stagnation region.

Figure 6.21 shows an extensive comparison of three increasingly turbulent flows at different nozzle-to-plate distances. While the maxima at the stagnation point completely disappears for flows above $Re = 20000$, it is also observed that the maximum pressure fluctuation corresponding to the vortex impingement shifts towards the stagnation region as the velocity of the jet is increased. This trend is also observed for an increase in the nozzle-to-plate distance for all flows. This suggests a decrease in the size of the structures impinging on the wall. The maximum fluctuations are observed at smaller Reynolds numbers for small nozzle-to-plate distances. The secondary peaks are noticeable at $Re = 35000$ and 50000.

It has been conjectured by Hall and Ewing (2005) who followed Didden and Ho (1985) that the dip in pressure fluctuations after the passage of primary structures and the subsequent peak in the radial region of the jet is caused due to unsteady separation of the secondary vortices formed in this flow. They noted that the secondary vortices moved faster than the primary structures and were ejected from the near wall region at $r/D \approx 1.4$. This, however, was observed at $Re = 19000$ by Didden and Ho (1985) in a *forced jet* and at a distance of 2 diameters from the exit of a long pipe by Hall and Ewing (2005). Similar phenomenon was observed by Landreth and Adrian (1990) through PIV measurements at $Re \approx 6500$. As seen in figure 6.22, a secondary vortex is formed at the point of separation located below and downstream of the primary vortex, which appears to have lifted away from the boundary layer. The secondary vortices rotate clockwise as opposed to the counter-rotating primary vortices due to viscous retardation at the wall. It should be noted here that for Reynolds number as low as 6500, in this current thesis, no such separation phenomenon has been observed. This necessitates an additional experimental confirmation through imaging techniques to establish the unsteady separation process in this region for this regime.

A comparison of the pressure fluctuations at different nozzle-to-plate distances at increasingly turbulent regimes are presented in figure 6.23. It can be observed that the wall pressure fluctuations for the three flows follow similar behaviour by decreasing as the

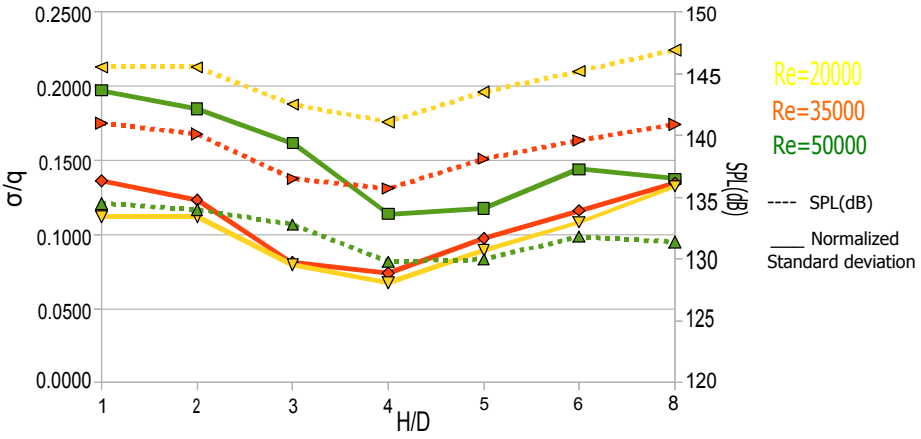

Figure 6.23: Comparison of peak values of pressure fluctuations for different nozzle-to-plate distances at various Reynolds numbers

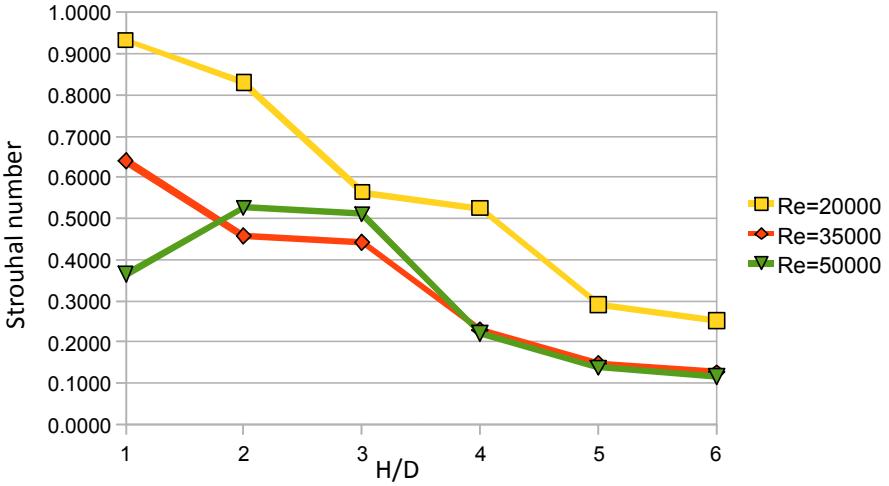

Figure 6.24: Comparison of non-dimensional vortex shedding frequencies in the impingement region for different nozzle-to-plate distances at various Reynolds numbers

nozzle-to-plate distances increases upto a height of $4D$ and increases when the distance from the nozzle is further increased. The lowest fluctuations can be found at $H/D = 4$ suggesting a region of lower sound pressure levels at the wall. This indicates that the vortex strength is larger ahead of the transition region and the vortex dissipates at larger nozzle-to-plate distances giving rise to turbulent flow that induces more prominent pressure fluctuations.

Figure 6.24 compares the Strouhal numbers corresponding to the vortex shedding frequency for the same configuration as above indicating a decreasing trend for increasing nozzle-to-plate distances. Since the velocity and characteristic lengths constituting to the Strouhal number are maintained constant, it can be noted that the frequencies detected decrease for larger distances between nozzle and plate indicating that the passage of vortices become more aperiodic as the turbulence levels increase.

6.4 Acoustic measurements

In addition to the near-field wall pressures, acoustic measurements are conducted to investigate the propagation of pressure fluctuations in the far-field due to impingement of coherent structures on the plate. The results are presented in this section.

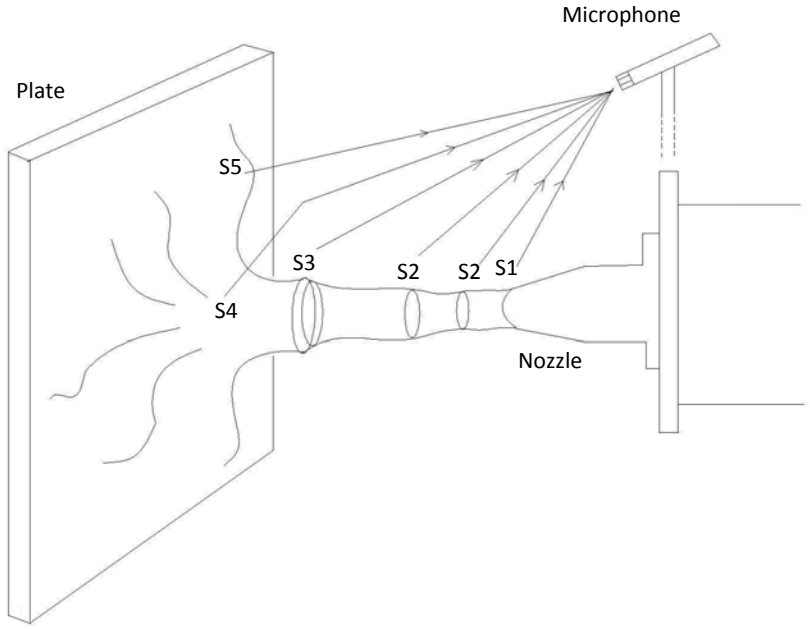

Figure 6.25: Representation of sources in an impinging jet contributing to the acoustic noise

Identifying the main generating mechanism of jet noise has been one of the important issues acted upon by many researchers. It is complicated to pursue this problem because of implicit difficulties such as diffraction and interference among acoustic waves interacting with the shear layers. The total noise power being generally much less than 1% of the jet-flow power and difficulty in using measurements of pressure fluctuations within a turbulent flow to identify the mechanisms (Nosseir and Ho (1982)) adds to the challenge. The same researchers attributed the mechanisms of sound generation to initial instability of the shear layer and impingement of large coherent structures on the plate. These two sources of noise radiate to the far-field via different acoustical paths.

In the research of Violato and Scarano (2011), Powell's aeroacoustic analogy was adopted to map the spatial distribution of the source term using 3D PIV data. The spatio-temporal evolution of such a source term was visualized revealing that the events of highest impact are associated with the processes of vortex-ring pairing and vortex ring disruption for the circular jet. In case of an impinging jet, interaction of coherent structures with the solid is the main cause of pressure fluctuations, that radiates as sound in the far-field. Therefore, it can be said that several events in the case of an impinging jet contribute to the far-field noise.

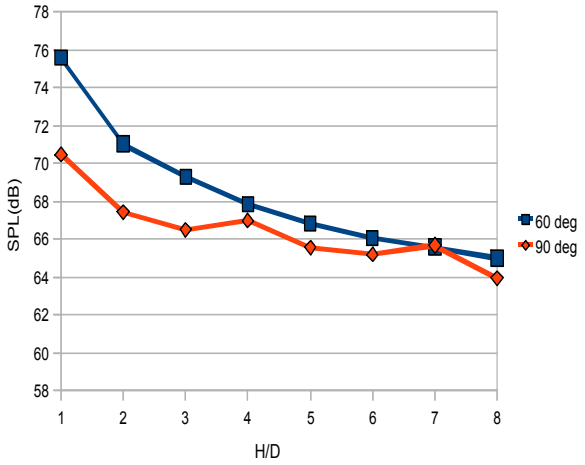

(a) d/D=30

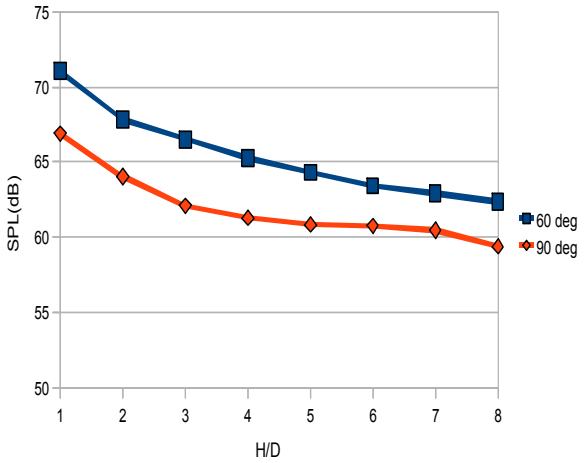

(b) d/D=50

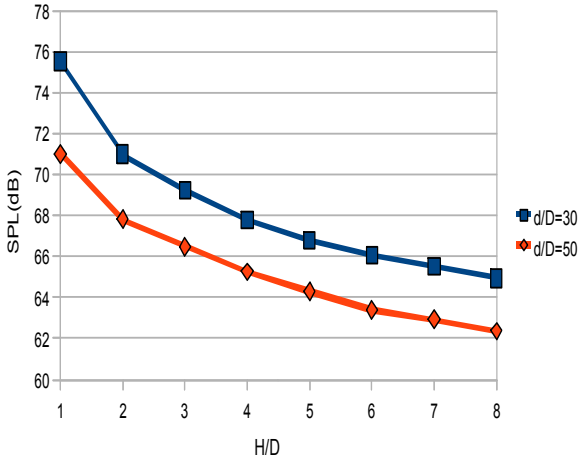

(c) Comparison of two far-field distances at 60 °C mic angle

Figure 6.26: Far-field measurements

Curle's analysis showed that the noise is generated both on solid surface and in the free jet. He theorises that noise from the free flow is of quadrupole type, which does not radiate as efficiently as the dipole type sound generated on the surface. However Powell's (1960) model implied equal contributions from both types which was disagreed upon by Nosseir and Ho (1982). They showed that the near-field pressure fluctuations produced by the pairing of vortices did not contribute largely to the total noise production in the far-field. The structures propagate to the surface with a speed of 0.62 times the flow velocity and then the fluctuating pressure radiates to the far field with the speed of sound. Hence most of the noise is generated on the plate which is in accordance with Curle's work. However, the other smaller contributors are described through a diagrammatic representation as in figure 6.25. The labels marked S1, S2, S3, S4, S5 show the different source mechanisms that produce sound in the far-field. S1 indicated at the nozzle edge marks the initial instability of the shear layer that is one of the important sources of sound generation (Nosseir and Ho (1982)). S2 belongs to the shedding and convection of vortices in the jet stream that produces weak quadrupolar sources. The pairing of vortices is represented by S3 which also generates far-field fluctuations albeit weaker in magnitude. S4 is in the impingement area which has been identified as the major contributor to impinging jet noise. According to Curle (1955), the dipoles generated at the surface are much more efficient generators of sound than the quadrupoles for low Mach numbers, given that the intensity of sound varies as sixth power of the velocity. S5 is concerned with the turbulent wall boundary flow (also refer 1.2c) which consists of secondary vortices and smaller eddies that produce pressure fluctuations, thereby adding to the total noise.

Since the waves lose their original identities through interference, far-field measurements alone do not suffice for estimation of the relative contribution from each source. This requires near-field pressure fluctuation data also. Cross-correlation of simultaneously acquired surface and acoustic pressures would enhance the understanding of source mechanisms in the impinging jet. In the present experiments, due to two different A/D conversion systems for acoustic microphone and pressure transducer and the availability of a single data acquisition card, simultaneous measurements could not be realized. This limits the scope of the acoustic measurements to the investigation of sound pressure levels produced upon impingement and an overview of the range of frequencies constituting to the impinging jet noise.

Measurements are conducted at a Reynolds number of 50000 for two far-field distances (d) of $0.3m$ and $0.5m$ from the impinging plate and at two angles of $60\,^\circ$ and $90\,^\circ$ owing to spatial constraints in the semi-anechoic chamber. A comparison of sound pressure levels at different nozzle-to-plate distances and two mic angles are shown in the figure 6.26. As it can be seen, the SPL detected at mic angle $\theta = 60\,^\circ$ is greater than that at $90\,^\circ$ in both the cases. Also the sound pressure levels decrease as the nozzle-to-plate distance increases which is in accordance with Marsh (1961).

The constituent frequencies in the system are obtained by Fourier transformation as described in chapter 5 with the application of an A-weighted filter. Since an impinging jet has both quadrupolar and dipolar sources originating from the shear layer and upon impact on the plate, it is not possible to determine singular frequencies with one microphone alone. An array of microphones, in this case would prove to be more advantageous. However, the single microphone does pick up a range of frequencies that is presented in figure 6.27. The main concentration of energy for all nozzle-to-plate distances can be

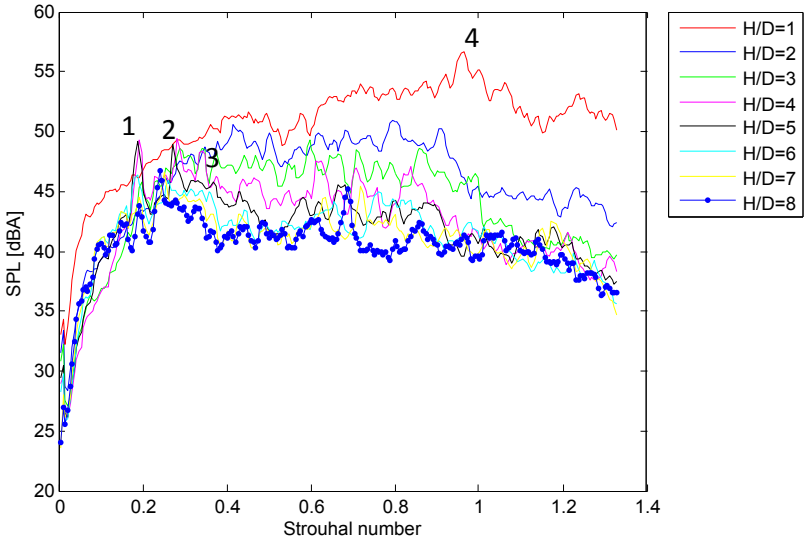

Figure 6.27: Comparison of far-field frequency spectra for different nozzle-to-plate distances for $\theta = 60\,°\mathrm{C}$ and $d/D = 30$

observed in between $St = 0.15 - 0.4$. Distinct peaks can be noticed at distances of 3-5 nozzle diameters at around $St = 0.18, 0.27, 0.34$, labelled 1, 2, 3 respectively, which corresponds to dimensional frequencies of 1350 Hz, 2025 Hz, 2550 Hz respectively. While the transition zone of the jet ($H/D \approx 4$) shows clear peaks throughout the spectrum, the frequencies are less apparent at other distances from the nozzle exit. These distinct peaks in the transition area could possibly represent the far-field frequencies due to pairing and shedding whose values are close to the near-field frequencies. Additionally at distances like $1D$ from the nozzle, the highest energy peak can be observed at $St = 0.96$, labelled 4 in the graph, that corresponds to a frequency of $7200Hz$ which is the highest frequency detected in the far-field. This could be possibly due to resonance at the jet orifice, which requires confirmation through cross-correlation with additional near-field flow measurements close to the orifice.

Chapter 7

Conclusions and Recommendations

7.1 Conclusions

Quantitative investigation of round impinging jets at different Reynolds numbers employing pressure sensors elucidates the behaviour of coherent structures of a jet upon impingement. Different flow regimes are investigated to gain a deeper understanding of the structures. Priorly conducted optical measurements through Thin Tomographic PIV by Violato et al., provides qualitative data that is used to corroborate the results obtained through pressure measurements. The vortices that begin as a definite toroidal structure due to K-H instabilities are transported along the axis of the jet encircling the core fluid until they reach the wall where they lose their axial velocity component and in turn gain a radial one. The vortex impingement is marked by maximum pressure fluctuations seen in all the profiles of various flows. The toroidal structures draws surrounding fluid into the jet stream and increase in size which can be observed from the region of vortex impingement in the pressure profiles. It can be noted that at lower velocities, the flow is laminar and the coherent structures maintain their identity very clearly. As the Reynolds number increases, the flow undergoes transition, the structures become more chaotic and ultimately lose their identity as the flow becomes turbulent. This is noticed in the reduced peak pressure variations as the flow regimes advance. The stagnation region is marked by a lesser pressure fluctuation with a presence of a maxima which can be attributed to the pressure gradient caused by lower pressures in the core of the vortex. The structures then break down and move along the surface(plate) giving rise to smaller eddies and transforming into a fully turbulent flow downstream of the stagnation point. As the distance from the stagnation point increases, the pressure fluctuations tend to zero. It is observed that the vortices reduce in size as the Reynolds number increases, exhibited by the shift of the impingement peak towards the stagnation point.

At very high Reynolds numbers such as 50000, a secondary peak is observed in the radial region following a dip in the pressure fluctuations which suggests possible unsteady separation in the flow and formation of a secondary vortex of lesser strength which impinges at around $r/D \approx 1.5$. This dip in fluctuation is seen from $Re = 25000$ and only in the

jet region of $H/D = 3 - 4$. Therefore a potential unsteady separation on the surface of impingement can be expected in the transitional region when the flow velocity is very high which could give rise to unsteady loads and also contribute to aeroacoustic noise.

The Fourier decomposition of pressure fluctuations yields the frequency of events occurring in an impinging jet. For lower Reynolds numbers, two clear peaks are visible which correspond to the pairing and shedding of vortices. A decrease in the pairing frequency at $Re = 20000$ before it completely disappears suggests that the number of pairings decreases as the Reynolds number increases. As the flow velocity is increased, the spectrum becomes increasingly broadband in nature in both- the stagnation as well as the outer radial wall region indicating that the passage of vortices is highly aperiodic. For highly turbulent flows like the case of 50000, the peak of the primary vortex shifts to a lower frequency indicating that these vortices pass with a lower convective velocity compared to that of the secondary structures which interact with the plate in the outer radial points.

The characteristics of different flows are summarised here.

Table 7.1: Characteristics of different flows

Reynolds number	Normalized σ_{max}	SPL_{max}	$St_{shedding}$	$St_{pairing}$
5000	0.1849	$110dB$	0.65	0.34
10000	0.1878	$122dB$	0.73	0.38
20000	0.1248	$130dB$	0.52 at $r/D = 1.4$	-
			0.33 at $r/D = 0$	0.09 at $r/D = 0$
50000	0.0692	$141dB$	0.38-0.48 at $r/D = 0,\ 1.5$	-
			0.18 at $r/D = 0.6$	-

The acoustic measurements conducted for two mic angles and far-field distances, gives an overview of the sound pressure levels produced by an impinging jet. At a Reynolds number of 50000, a gradual decrease in the sound pressure levels for increasing nozzle-to-plate distances is observed. The sound pressure levels of the range close to $75dB$ also decreases by less than 10% for an increase in the distance of $0.2m$ between the source and the observer.

7.2 Recommendations

Despite a large base of knowledge available on impinging jets, the following areas pertaining to experimental techniques and impinging jets can be investigated in future-

- Time resolved PIV measurements can be done for a highly turbulent flow regime like that of $Re = 50000$, firstly to obtain a clear visualization of the flow structures, secondly to investigate the unsteady separation in the boundary layer of the radial wall jet and formation of secondary structures as discussed in 6.3. Since this regime is also marked by highly three-dimensional structures owing to its turbulence levels, it is imperative to understand the physical processes occurring during the growth of the three-dimensional flow. This also plays a key role in understanding the essential differences between turbulent large eddies and vortex rings in such flows.

- The design of the jet facility can be improved such that the distance between the nozzle exit and the back-wall of the existing semi-anechoic chamber is sufficiently far away, which will enable a complete acoustic directivity test in the far-field region.
- A microphone array or sound visualization techniques such as scan and paint or acoustic cameras could be employed to obtain the noise source distribution in an impinging jet. Apart from being a novel technique for the case of impinging jets, this will also provide accurate data on the frequencies of the individual sources contributing to the noise.
- Alternatively, following a computational approach, the far-field noise emissions can be extrapolated by using the pressure field obtained through time-resolved PIV measurements using Curle's aeroacoustic formulation.
- Multiple sensors can be employed to measure the near-field of the flow and the rigid surface along with far-field measurements. Advanced correlation techniques can be employed to identify the noise sources for this configuration.
- It can be understood from the literature that oblique impingement results in lower sound pressure levels as compared to normal impingement. It would therefore be interesting to investigate the case of obliquely impinging jets through both Tomographic PIV and pressure measurements.

Appendix A

Thin Tomographic Particle Image Velocimetry

Particle Image Velocimetry(PIV) is a recent entrant into the field of fluid flow measurement and provides instantaneous velocity fields over global domains(2D or 3D) and related properties with high accuracy. It is a non-intrusive technique and unlike other measurement techniques which provide data at a single point, PIV can produce three dimensional vector fields of the flow. The technique involves recording entrained particles in a fluid that follows the direction of the flow using an optical camera. The particles are illuminated with light and the light scattered by them is recorded onto two subsequent image frames by a digital imaging device, typically a CCD camera placed perpendicular to the measurement plane. The displacement of these particles is used to calculate the speed and direction of the flow being studied.

The instantaneous measurement of 3D velocity field is of great interest to research in fluid mechanics as it enables to reveal the complete topology of the unsteady coherent flow structures. Turbulent flows are highly three dimensional in nature and thus requires the application of measurement techniques that are able to capture instantaneously its 3D structure, the complete stress tensor and the vorticity vector. A new system for 3D measurements based on tomographic reconstruction of 3D particle distribution is employed to complement the point measurement data. Recordings of particle images from an illuminated volume taken from several viewing directions simultaneously are used to reconstruct the 3D light intensity distribution. This method is therefore referred to as tomographic particle image velocimetry. Given that the two subsequent exposures of the particle images are obtained, the measurement technique returns the instantaneous velocity field within the measurement volume by means of 3D particle pattern correlation. Details are presented in Appendix.

Time-resolved PIV experiments are done in the water facility at the Aerodynamics Laboratories of TU Delft. An octagonal tank of $600mm$ diameter and $800mm$ height is fit with the water supply system at the bottom that emerges into the tank through a nozzle of $0.01m$ diameter and contraction ratio of 56.25. The tank is made out of plexiglass to

enable optical access for visualising and image acquisition. The supply tank is the same as that described in section 4.2.3 without the presence of sound absorbing foam in the cylinder. The water is driven hydrostatically through a pump which provides a stabilized supply of water in an exit velocity range of 0.1-2 m/s. Tomographic experiments are performed for Reynolds numbers ranging between 5000, 10000 and 20000 which corresponds to the aforementioned velocity range, based on jet diameter, D. The water jet impinges upon a plate of 250 x 250mm with normal incidence which is placed at a distance of $4D$ from the nozzle exit. For seeding, neutrally buoyant particles of polyamide of $10\mu m$ are dispersed homogeneously, achieving a concentration of 9.85 particles/mm^3. A Quantronix Darwin-Duo solid-state diode pumped Nd:YLF laser is used for illuminating the flow field. The laser energy is (2x25 mJ/pulse at $1kHz$). The thickness of the laser sheet is about $5mm$ formed by the means of a cylindrical lens followed by knife edges. The images are captured by a tomographic system consisting of 3 Imager pro HS 4M cameras (2016 x 2016 pixels at 1.3kHz, 11μ pixel pitch) that are arranged horizontally with an azimuthal aperture of 90 degrees. Nikon objectives of 105 mm focal length are mounted on camera-lens tilt mechanisms are mounted to comply with the Schielmpflug condition and they are set with a numerical aperture $f\#$=16 to allow focussed imaging of the illuminated particles. For a chosen imaging configuration, the particle image density attains a maximum of 0.04 particles. Sequences of tracer particles are captured at a rate of 1 kHz resulting in 35 samples for the fastest expected events (vortex shedding). The field of view is 63 x 30 mm with a digital resolution of 30 pixels/mm.

The volumetric light intensity reconstruction is performed following the Multiplicative Algebraic Reconstruction Technique(MART) algorithm by LaVision software DaVis 8. The three-dimensional particle field motion is computed by Volume Deformation Iterative Multigrid(VODIM) technique with a final interrogation volume of 24x24x24 voxels (0.8x0.8x0.8 mm^3) with an overlap between adjacent interrogation boxes of 75%. Velocity vector fields are obtained by averaging the cross-correlation map over three subsequent object-pairs, which corresponds to a recording time of $3ms$ (Scarano et al., 2010). This method can be applied to unsteady vector fields sampled with rate higher than that strictly needed for temporally resolving flow yielding the reduction in precision error without compromising the temporal resolution.

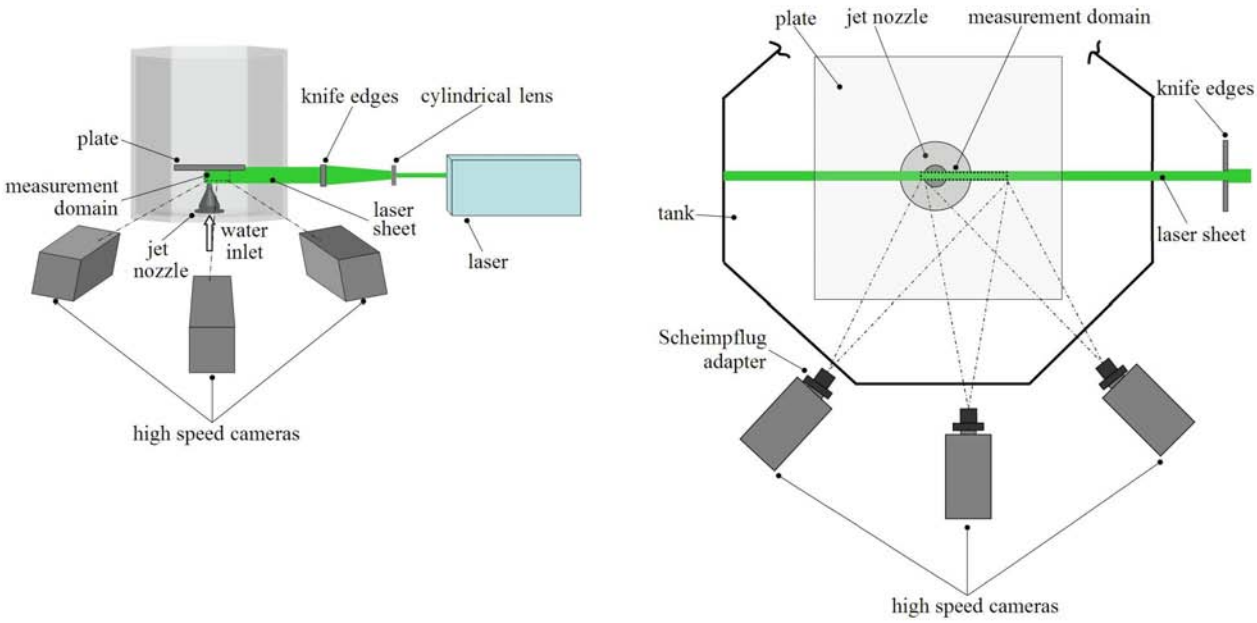

Figure A.1: Schematic view of illumination and imaging in the tomographic experiment (left); top view of the system (right).[Violato and Scarano (2011)]

Appendix B

Drawings

This section presents an overview of the nozzle design and the semi-anechoic chamber.

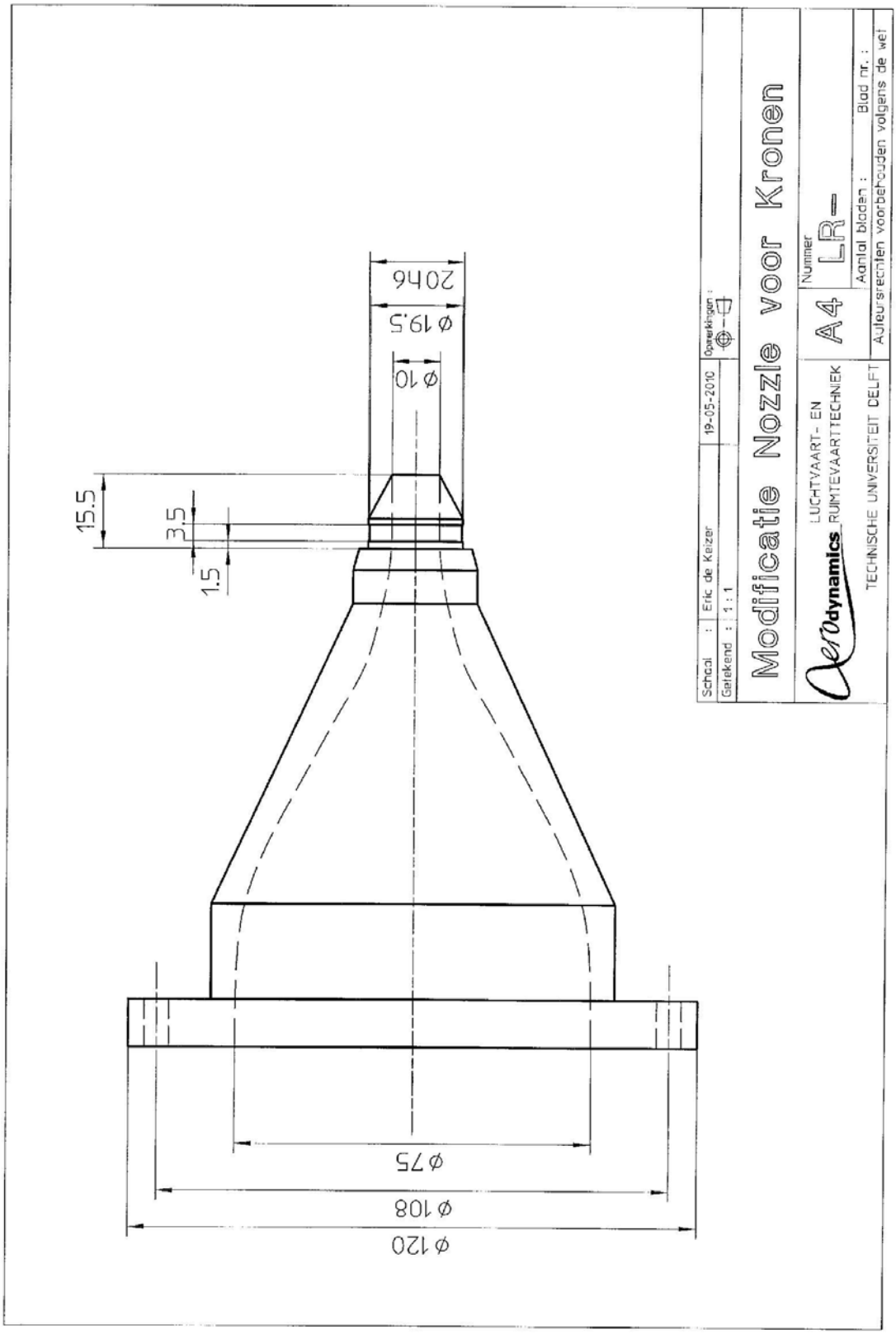

Figure B.1: Nozzle dimensions (Courtesy:Eric de Keizer)

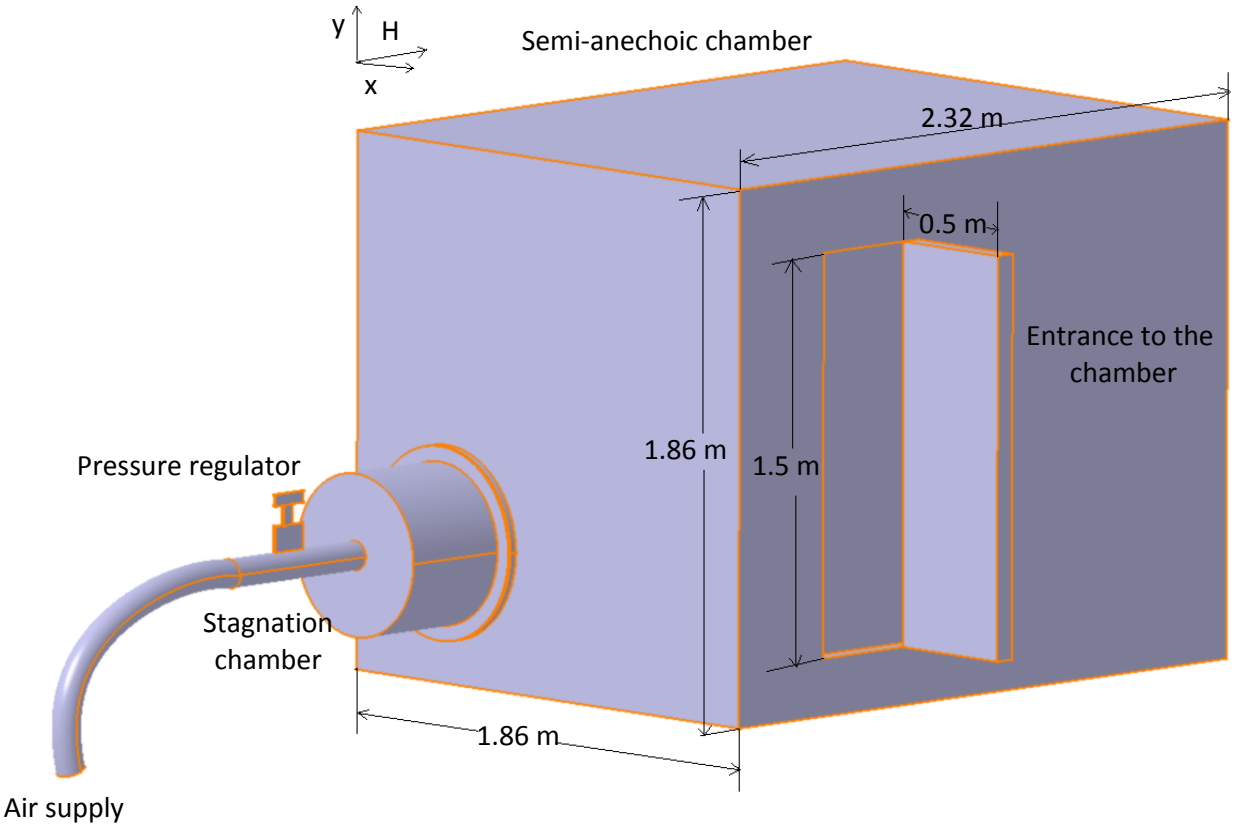

Figure B.2: Representation of the semi-anechoic chamber

References

Armstrong, R., Michalke, A., and Fuchs, H. (1976). Coherent structures in jet turbulence and noise. In *American Institute of Aeronautics and Astronautics Conference*, volume 1.

Arndt, R., Long, D., and Glauser, M. (1997). The proper orthogonal decomposition of pressure fluctuations surrounding a turbulent jet. *Journal of Fluid Mechanics*, 340(1):1–33.

Becker, H. and Massaro, T. (1968). Vortex evolution in a round jet. *Journal of fluid mechanics*, 31(03):435–448.

Brown, G. and Roshko, A. (1974). On density effects and large structure in turbulent mixing layers. *Journal of Fluid Mechanics*, 64(04):775–816.

Choy, Y., Zhen, H., Leung, C., and Li, H. (2012). Pollutant emission and noise radiation from open and impinging inverse diffusion flames. *Applied Energy*, 91(1):82–89.

Cooper, D., Jackson, D., Launder, B., and Liao, G. (1993). Impinging jet studies for turbulence model assessment–i. flow-field experiments. *International Journal of Heat and Mass Transfer*, 36(10):2675–2684.

Crow, S. and Champagne, F. (1971). Orderly structure in jet turbulence. *J. Fluid Mech*, 48(3):547–591.

Curle, N. (1955). The influence of solid boundaries upon aerodynamic sound. *Proceedings of the Royal Society of London. Series A. Mathematical and Physical Sciences*, 231(1187):505–514.

Daniele Violato, Andrea Ianiro, G. C. F. S. (2011). Three-dimensional vortex dynamics and convective heat transfer in circular and chevron impinging jets. *International Journal of Heat and Fluid Flow Manuscript Draft*.

de Boer, T. (2011). Aeroacoustic investigation of an incompressible jet with various nozzle geometries. Master's thesis, Delft University of Technology.

Didden, N. and Ho, C. (1985). Unsteady separation in a boundary layer produced by an impinging jet. *Journal of Fluid Mechanics*, 160(1):235–256.

Elsinga, G., Scarano, F., Wieneke, B., and Van Oudheusden, B. (2006). Tomographic particle image velocimetry. *Experiments in Fluids*, 41(6):933–947.

Gauntner, J., Livingood, J., and Hrycak, P. (1970). Survey of literature on flow characteristics of a single turbulent jet impinging on a flat plate. *Washington, DC.*

Hall, J. and Ewing, D. (2005). The development of the large-scale structures in round impinging jets exiting long pipes at two reynolds numbers. *Experiments in fluids*, 38(1):50–58.

Hall, J. and Ewing, D. (2006). On the dynamics of the large-scale structures in round impinging jets. *Journal of Fluid Mechanics*, 555(1):439–458.

Ho, C. and Nosseir, N. (1981). Dynamics of an impinging jet. part 1. the feedback phenomenon. *Journal of Fluid Mechanics*, 105(1):119–142.

Hori, T. and Sakakibara, J. (2004). High-speed scanning stereoscopic piv for 3d vorticity measurement in liquids. *Measurement Science and Technology*, 15:1067.

Horn, G. and Thring, M. (1956). Angle of spread of free jets.

Howe, M. (2003). *Theory of vortex sound*, volume 33. Cambridge Univ Pr.

Hussein, H., Capp, S., and George, W. (1994). Velocity measurements in a high-reynolds-number, momentum-conserving, axisymmetric, turbulent jet. *Journal of Fluid Mechanics*, 258(1):31–75.

Jordan, P. and Gervais, Y. (2008). Subsonic jet aeroacoustics: associating experiment, modelling and simulation. *Experiments in Fluids*, 44(1):1–21.

Kataoka, K., Hashimoto, S., Kamiyama, Y., and Komai, T. (1982). Mass transfer between a plane surface and an impinging turbulent jet: the influence of surface-pressure fluctuations. *Journal of Fluid Mechanics*, 119:91–105.

Ko, N. and Chan, W. (1978). Similarity in the initial region of annular jets: three configurations. *Journal of Fluid Mechanics*, 84(04):641–656.

Landreth, C. and Adrian, R. (1990). Impingement of a low reynolds number turbulent circular jet onto a flat plate at normal incidence. *Experiments in fluids*, 9(1):74–84.

Liepmann, D. and Gharib, M. (1992). The role of streamwise vorticity in the near-field entrainment of round jets. *Journal of Fluid Mechanics*, 245:643–643.

Lighthill, M. (1952). On sound generated aerodynamically. In *Proc. Roy. Soc. Lond., A*, volume 211, pages 564–587.

Marsh, A. (1961). Noise measurements around a subsonic air jet impinging on a plane, rigid surface. *The Journal of the Acoustical Society of America*, 33:1065.

Nati, G. (2011). Suppression of vortex shedding from a truncated trailing edge by plasma actuation. Master's thesis, Delft University of Technology.

Nosseir, N. and Ho, C. (1982). Dynamics of an impinging jet. part 2. the noise generation. *Journal of fluid mechanics*, 116(1):379–391.

Petrie, A. (1974). An experimental investigation of the noise produced by air jet impingement on flat plates. *Applied Acoustics*, 7(2):117–126.

Pope, S. B. (2000). *Turbulent Flows*. Cambridge Univ Press.

Popiel, C. and Trass, O. (1991). Visualization of a free and impinging round jet. *Experimental thermal and fluid science*, 4(3):253–264.

Roshko, A. (1981). The plane mixing layer flow visualization results and three dimensional effects. *The Role of Coherent Structures in Modelling Turbulence and Mixing*, pages 208–217.

Shen, J. and Meecham, W. (1993). Quadrupole directivity of jet noise when impinging on a large rigid plate. *The Journal of the Acoustical Society of America*, 94:1415.

Tollmien, W. (1926). Berechnung turbulenter ausbreitungsvorgänge. *ZAMM-Journal of Applied Mathematics and Mechanics/Zeitschrift für Angewandte Mathematik und Mechanik*, 6(6):468–478.

Violato, D., Moore, P., and Scarano, F. (2011). Lagrangian and eulerian pressure field evaluation of rod-airfoil flow from time-resolved tomographic piv. *Experiments in fluids*, 50(4):1057–1070.

Violato, D. and Scarano, F. (2011). Three-dimensional evolution of flow structures in transitional circular and chevron jets. *Physics of Fluids*, 23(12):124104–124104.

Viskanta, R. (1993). Heat transfer to impinging isothermal gas and flame jets. *Experimental Thermal and Fluid Science*, 6(2):111–134.

Winant, C. and Browand, F. (1974). Vortex pairing- the mechanism of turbulent mixing-layer growth at moderate reynolds number. *Journal of Fluid Mechanics*, 63(2):237–255.

Yan, X., Baughn, J., and Mesbah, M. (1992). The effect of reynolds number on the heat transfer distribution from a flat plate to an impinging jet. *Fundamental and applied heat transfer research for gas turbine engines*, pages 1–7.

Yule, A. (1978). Large-scale structure in the mixing layer of a round jet. *Journal of Fluid Mechanics*, 89(3):413–432.